2004

AN IMPEDANCE TUBE FOR THE IN-SITU CLASSIFICATION OF BUBBLY LIQUIDS

BOSTON UNIVERSITY

COLLEGE OF ENGINEERING

Thesis

AN IMPEDANCE TUBE FOR THE

IN-SITU CLASSIFICATION OF

BUBBLY LIQUIDS

by

JED CHESTER WILBUR

B.S., Lafayette College, 2002

B.A., Lafayette College, 2003

Submitted in partial fulfillment of the

requirements for the degree of

Master of Science

2004

Approved by

Advisor: _____

Ronald A. Roy, Ph.D
Professor, Aerospace and Mechanical Engineering

Second Reader: _____

William M. Carey, Ph.D.
Professor, Aerospace and Mechanical Engineering

Third Reader: _____

Raymond Nagem, Ph.D.
Professor, Aerospace and Mechanical Engineering

ACKNOWLEDGEMENTS

Attempting to acknowledge everyone who helped me along the long road leading to this thesis would result in an unmanageably long list of names. What follows is certainly an abbreviated list, and my apologies to those forgotten: rest assured your help was greatly appreciated.

To begin with, I must thank the members of my thesis committee, professors William Carey, Raymond Nagem, and my advisor, Ronald Roy. Not only did they read and correct this thesis, but all three contributed at different stages of the process. Professor Carey was the driving force teaching me not only the theoretical physics behind this project, but the importance of a sound theory as well. He also proved remarkably able to provide funding sources for a number of the field excursions that made this work possible. Professor Nagem was a remarkably thorough proofreader and played a mean game of basketball when the need to relieve stress arose. And professor Roy not only guided me or let me work alone when needed, but constantly forced me to work harder and investigate deeper, helping shape me not only into a better scientist and engineer, but person as well.

Perhaps the one person who helped me most at Boston University was Dr. Preston Wilson. Preston not only painstakingly laid the groundwork for much of the work discussed here, but spent countless hours working with me in the lab, discussing experiments, theory, and Texas music. After leaving BU, Preston was always more than willing to help out through phone conversations and many detailed emails. Without Preston's help and dedication to the project, this work would be much less complete than it is now.

The many field experiments would not have been possible had it not been for the gracious

AN IMPEDANCE TUBE FOR THE IN-SITU

CLASSIFICATION OF BUBBLY LIQUIDS

JED CHESTER WILBUR

ABSTRACT

It is well documented that the presence of even a few air bubbles in water can significantly alter the propagation and scattering of sound. Air bubbles are both naturally and artificially generated in all marine environments, especially near the sea surface. The ability to measure the acoustic propagation parameters of bubbly liquids in situ has long been a goal of the underwater acoustics community. One promising solution is a submersible, thick-walled, liquid-filled impedance tube. Recent water-filled impedance tube work was successful at characterizing low void fraction bubbly liquids in the laboratory [1].

This work details the modifications made to the existing impedance tube design to allow for submersed deployment in a controlled environment, such as a large tank or a test pond. As well as being submersible, the useable frequency range of the device is increased from 5 - 9 kHz to 1 - 16 kHz and it does not require any form of calibration. The opening of the new impedance tube is fitted with a large stainless steel flange to better define the boundary condition on the plane of the tube opening.

The new device was validated against the classic theoretical result for the complex reflection coefficient of a tube opening fitted with an infinite flange. The complex reflection coefficient was then measured with a bubbly liquid (order 250 micron radius and 0.1 - 0.5 % void fraction) outside the tube opening. Results from the bubbly liquid experiments were

inconsistent with flanged tube theory using current bubbly liquid models. The results were more closely matched to unflanged tube theory, suggesting that the high attenuation and phase speeds in the bubbly liquid made the tube opening appear as if it were radiating into free space. (Work supported by the US Navy Office of Naval Research.)

Contents

List of Figures

xix

Chapter 1

Introduction

This thesis details the design, construction, and validation of an instrument, a submersible, baffled, thick-walled, water-filled acoustic impedance tube, to measure acoustic propagation parameters of bubbly liquids. This section provides a historical introduction to bubbly liquid theory and outlines previous work with water-filled impedance tubes. But first, a discussion of the motivation behind this work is in order.

1.1   Motivation and Background

Why in the world would do people study bubbly liquids? That is fair and just question, for certain, with a simple answer: As any member of the underwater or biomedical acoustics communities will be quick to tell you, because *bubbles are everywhere.* They are formed in lakes and oceans by breaking waves [2, 3], falling rain [2, 4], and even snowflakes [2, 5]. Bubbles are often purposely injected into the human body as ultrasound image enhancers

[6] while the unwanted formation of bubbles in the body is responsible for decompression sickness ("the bends") [7]. Bubbles formed by high-intensity sound waves can be used to stop otherwise uncontrollable bleeding, clean teeth, and destroy kidney stones [8, 9] but are also speculated to be responsible for a number of recent marine mammal strandings [10]. One research team has even reported evidence of nuclear fusion occurring during a particularly violent bubble collapse[11, 12]! A second reason to study bubbles is that they can exhibit extraordinarily non-linear behavior in the presence of sound waves and remarkably, most of this behavior can be explained by straightforward theoretical considerations.

Bubbly liquid theory, the behavior of a distribution of gas bubbles in a liquid acting as an effective medium, was first investigated around the turn of the century [13, 14] but received little attention at the time. It was not until the advent of sound navigation and ranging (sonar, then referred to as *asdics* for anti-submarine division - *ics*) as a tool for detecting German U-boats in World War II that research in bubbly liquid theory began in earnest, both in the United States [15, 16] and in Germany [17]. Bubbly liquid work saw somewhat of a renaissance with the fall of the Soviet Union as the focus of sonar systems shifted from deep-water hunting of Soviet submarines to shallow-water mine detection. Bubbles are far more important in shallow water sound propagation as interactions of sound with the sea surface, where the highest concentrations of bubbles are found [18], must be considered. A short history of bubbly liquid theory is given in the next section.

Much work has been done to observe and measure the bubble propagation parameters predicted by competing bubbly liquid theories. This is a difficult task as bubbly liquids

attenuate sound very effectively over a relatively broad rang of frequencies. Methods that require measurement of forward propagation through a bubbly liquid often fail because the sound waves are attenuated before ever reaching the receiving hydrophone. Nevertheless, a number of researchers have presented measurements of both bubbly liquid phase speeds (the speed at which the acoustic wave propagates) and attenuation (how much acoustic energy is lost over distance) [19, 20, 21, 22, 23]. There is still a paucity of data around the resonant frequencies of the individual bubbles, especially for bubbly liquids with high void fractions (the percentage by volume of the free gas in the mixture).

One approach around the attenuation problem is to use measurement techniques that do not require sound to propagate through the bubbly liquid itself. The classic and most well known instrument of this sort (and perhaps of all acoustic measurement devices) is the impedance tube. A brief introduction to water-filled impedance tubes follows this Chapter's discussion of bubbly liquids.

1.2   A short history of bubbly liquid theory

Minnaert [24], in 1933, investigated what he believed to the cause of "the murmur of the brook, the roar of the cataract, or the humming of the sea" – resonating air bubbles trapped in the water. He devolved a formula for the resonant frequency of a gas bubble in a fluid by equating the potential energy of the compressed gas inside the bubble at minimum volume to the kinetic energy of the fluid at maximum bubble "wall" velocity. His result for the natural frequency, ω_0 (in radians per second), still valid today for many practical

applications, is

$$\omega_0 = \frac{1}{a_0}\sqrt{\frac{3\eta P_\infty}{\rho_\ell}}. \qquad (1.1)$$

Here, a_0 is equilibrium bubble radius, η is the polytropic index for the gas expansion and compression ($PV^\eta = \text{constant}$), and P_∞ and ρ_ℓ are the hydrostatic pressure and density, respectively, of the host liquid.

Minnaert neglected the Laplace pressure due to surface tension and assumed that the bubble behaved adiabatically, taking the polytropic index to be γ, the ratio of the gas' specific heats. Modern analysis has shown that both of these assumptions are acceptable for the "large" bubbles Minnaert was studying (> 1 millimeter in radius). Corrections making Eq. (1.1) applicable to a broader range of bubbles will be addressed in Section 2.2.

Twenty-three years before Minnaert published his bubble resonance work, Mallock [13] studied propagation of sound in bubbly liquids, calling them "frothy liquids." While the focus of his work was on the attenuation of sound, he derived an equation for the velocity of sound propagation in bubbly liquids. In his 1930 book, *A Textbook of Sound*, A. B. Wood [14] cast Mallock's result in a more useful form. A general derivation of their result follows and a more rigorous one is given in Appendix A.

The velocity of sound, c, is generally defined as

$$c^2 = \frac{1}{\rho\kappa} \qquad (1.2)$$

where ρ and κ are the density of compressibility of the medium, respectively. Both Mallock and Wood argued that for a mixture of gas bubbles in liquid the *effective sound speed* of the mixture, c_m, is the same as it would be for a fluid of the same mean density, ρ_m, and

mean compressibility, κ_m (here the subscript m refers to mixture). That is to say

$$\rho_m = (1 - \beta)\,\rho_\ell + \beta\rho_g$$

$$\kappa_m = (1 - \beta)\,\kappa_\ell + \beta\kappa_g$$

$$(1.3)$$

where the subscripts ℓ and g refer to the liquid and gas components and β is the *void fraction* – the ratio of volume of gas to the total volume of the mixture,

$$\beta = \frac{V_g}{V_m}. \tag{1.4}$$

Plugging Eq. 1.3 into 1.2, the speed of sound propagation in the effective medium, c_m, is

$$\frac{1}{c_m^2} = \frac{(1 - \beta)^2}{c_\ell^2} + \frac{\beta^2}{c_g^2} + \beta\,(1 - \beta)\,\frac{\rho_g^2 c_g^2 + \rho_\ell^2 c_\ell^2}{\rho_\ell \rho_g c_\ell^2 c_g^2}. \tag{1.5}$$

This is known as Wood's Equation[1]. The limiting assumption in this derivation is that a bubble's compressibility is essentially the same as the gas inside it. The compressibility of bubbles being driven well below their resonant frequencies is equivalent to the isothermal compressibility of the gas. Thus Eq. (1.5) holds for low driving frequencies (those frequencies well bellow the individual bubble resonance, $\omega << \omega_0$) if c_g is taken as the isothermal sound speed.

Equation (1.5) is plotted as a function of void fraction in Figure 1.1 for air bubbles in water. This plot shows how the addition of air bubbles into water representing as little as $10^{-5}\%$ of the total volume reduces the sound speed significantly. A minimum occurs at 50% void fraction, where the phase speed is around 20 m/s, about 1.3% of the sound speed in

---

[1]One may protest that Mallock derived the same result some 20 years earlier and should deserve credit for the equation. The only difference this author can find is that Wood used the definition of void fraction still prevalent today, while Mallock defined proportionality constants between the liquid and gas phases. Perhaps the underwater sound community should adopt the notation *Wood-Mallock Equation*.
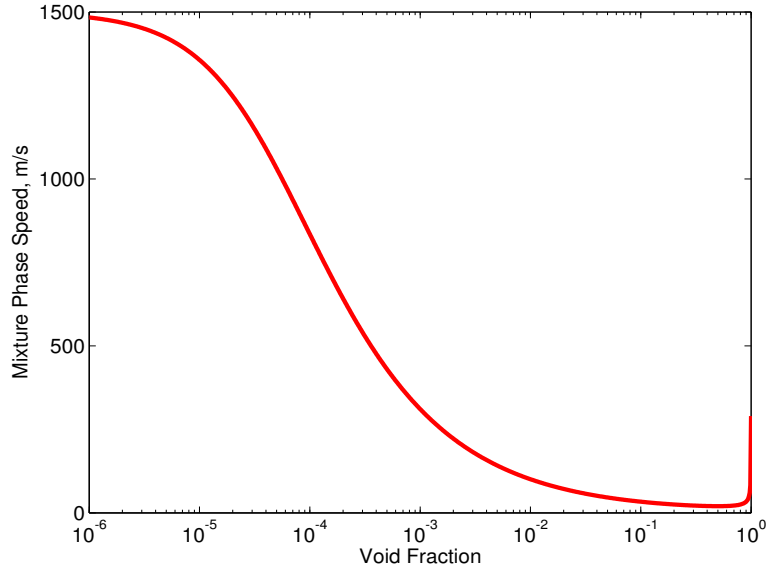
Figure 1.1: The speed of sound in a bubbly liquid predicted by Wood's equation at different void fractions; c_ℓ=1500 m/s, ρ_ℓ=1000 kg/m^3, c_g=290 m/s, ρ_g=1.2kg/m^3.

water and 6.9% of the sound speed in air. The steep reduction in sound speed experienced at very low void fractions results from the combination of a relatively high mixture density (approximately that of water) and high mixture compressibility caused by the addition of just a few air bubbles (similar to how just a little pocket of air in the brake lines of an automobile significantly reduces braking ability).

Significant work has been done to modify Eq. (1.5) to include the effects of bubble dynamics. The first successful attempts were made by Spitzer [15] and Foldy [16] working at the Division of War Research at Columbia University at the height of WWII. They modelled bubbles as damped harmonic oscillators with a resonant frequency given by Eq. (1.1) and a damping constant that was to be empirically measured. In fact, the only major differences between their results and those most commonly accepted today are the damping

constant and the polytropic exponent used to calculate the resonant frequency.

In 1959 Devin [25] derived an expression for the damping coefficient of a resonating bubble. He also corrected Minneart's resonant frequency expression to include a polytropic exponent that is a function of bubble size. Prosperetti [26, 27] extended Devin's work, developing the first complete model of the thermodynamic and heat transfer processes inside an oscillating gas bubble, providing an accurate expression for the damping constant and polytropic exponent for an arbitrary driving frequency. These were the missing pieces in bubbly liquid theory, at least for low void fractions, and Prosperetti [28] in 1987 and Commander and Prosperetti [29] in 1989 showed using the accurate single bubble model, the complete bubbly liquid model agreed reasonably well with experimental measurements. Recent attempts to correct for higher void fractions will be discussed in Section 2.2.3.

Needless to say, the history of bubbly liquid theory presented above is a bit cursory, but it does capture most of the advances relevant to this work. The amount of literature on single bubbles alone fills volumes. Leighton's monologue on the acoustic bubble [30] has well over 1,000 references to literature concerning bubbles and is a good starting point for those readers seeking more information about the wonderful world of bubbles and bubbly liquids. We will revisit bubbly liquid theory in more depth in Section 2.2, developing an expression for the complex sound speed that includes the effects of bubble dynamics.

1.3   The water-filled impedance tube

As mentioned earlier, impedance tubes are well-suited for the measurement of sound propagation parameters in a bubbly liquid. Measurement of bubbly liquids, however, requires that the impedance tube be filled with water (or some other liquid). Water-filled impedance tubes have received little attention since first developed by German scientists in WWII [17]. Only in the past five years have water-filled impedance tubes approached the accuracy of their air-filled predecessors [1, 31].

Wilson [1] was the first to apply the impedance tube technique to measure the acoustic properties of bubbly liquids, and obtained good results for low void fractions. An illustration of his apparatus is shown in Figure 1.2. This setup looks and behaves very much like a standard air-filled impedance tube setup. Sound waves generated by a sound source interact with a bubbly liquid confined in the upper portion of the tube. The complex transfer function between the two hydrophones is measured and used to determine the acoustic properties of the bubbly liquid interface, which we term the "measurement plane". This system is described in detail in Chapter 3.

While Wilson's approach was overall very successful, there were a number of limitations to his apparatus and method. In his work, a bubbly liquid was produced inside the tube using needles. These needles were located in the measurement plane of the impedance tube, possibly interfering with the measurement. As the bubbly liquid was inside a tube, the effects of the tube wall on bubble propagation must be considered and placed an upper bound on the measurable phase speed. Measurements were made with two wall-mounted
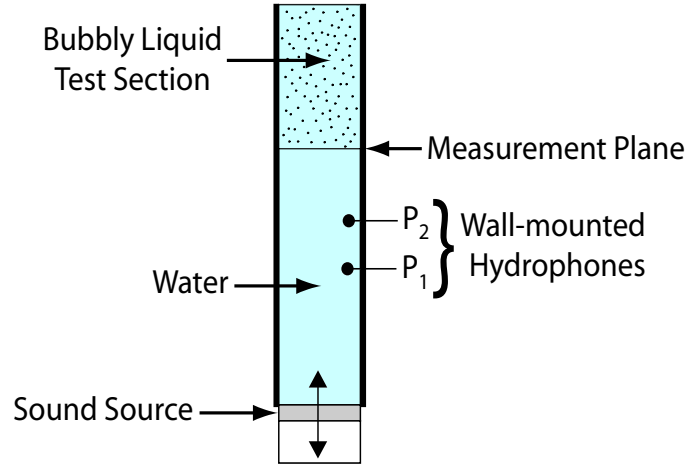
Figure 1.2: The impedance tube designed by Wilson to measure the acoustic properties of bubbly liquids in 5 to 9 kHz range.

hydrophones whose spacing fixed the usable frequency range of Wilson's instrument to 5-9kHz. The use of two independent hydrophones also made a calibration necessary before each use.

Water-filled impedance tubes have seen more use measuring the acoustic characteristics of water-saturated marine sediments. Dunlop [32] developed a water-filled tube to measure the acoustic properties of sediments *in situ* and was able to accurately measure attenuation but not sound speed. Park [33] used Wilson's impedance tube to measure the impedance of a length of sediment. Her results compared poorly with accepted sediment models due to difficulties accounting for interactions between the sediment sample and the tube wall. Wilson and Roy [34] used a single-hydrophone impedance tube, very similar to the one used in the present work, to measure the acoustic propagation parameters of a sediment sample. While their measurements of the phase speed were in line with accepted sediment models, those of attenuation were not, despite attempts to model interaction with the tube wall.

9

Wilson, et al. [35], in a first step towards the development of an *in situ* device, placed the impedance tube on a large sample of sediment entirely outside the tube. While this setup eliminated the problems with wall interactions, the system proved too difficult to model and no meaningful results were obtained.

The impedance tube design presented in this work overcomes some of the previous devices' limitations. Here the bubbly liquid sample is placed outside the tube completely, eliminating artifacts caused by the elastic tube walls and allowing the bubble production mechanism to be located far away from the measurement plane. The wall-mounted hydrophones are replaced with a single hydrophone which is remotely scanned along the tube axis, increasing the instrument's usable frequency range to 1 to 16 kHz and eliminating the need for calibration. Finally, all components of the new impedance tube are designed to operate remotely below up to 25 meters of water, allowing measurements to be made *in situ*.

The new device is illustrated in Figure 1.3. The opening of the tube is fitted with a large baffle and an acoustically transparent window. This baffle serves to better define the boundary condition along the measurement plane of the tube's opening, simplifying the theoretical model. The theoretical model is important as the standing wave field inside this baffled tube with a bubbly liquid is considerably different than that for the previous impedance tube (where the bubbly liquid was inside a section of the tube). In both cases, the high attenuation in bubbly liquids is used to our advantage. For the previous tube, the length of the bubbly liquid sample could be considered infinite as the incident wave was

completely attenuated in the sample section and no reflection from the far surface occurred. For the current tube, the attenuation makes the finite-sized baffle appear infinite in extent, as the radiated waves are attenuated before ever being in communication with the end of the baffle. Significant attention to baffled tube theory is paid in Section 2.1.
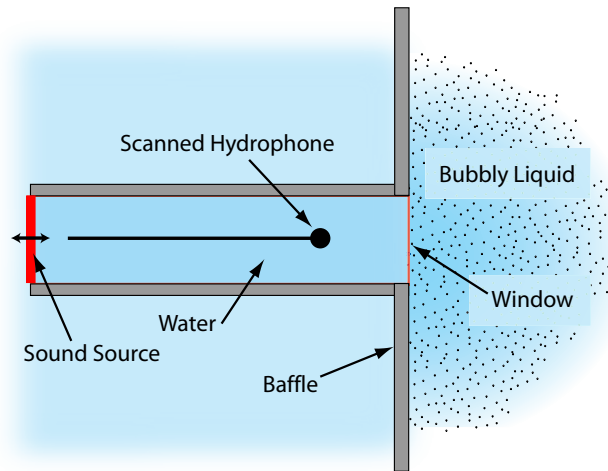
Figure 1.3: The submersible, baffled water-filled impedance tube.

1.4   Thesis roadmap

The remainder of this thesis is broken into five Chapters. Chapter 2 covers the theory of sound propagation in a rigid baffled tube and develops the full model for sound propagation in a bubbly liquid. Predictions are also made concerning the behavior of a water-filled baffled tube with a bubbly liquid outside it. Chapter 3 describes the experimental apparatus and measurement procedures. Attention is paid to the impedance tube measurement theory, the effects of elastic tube walls on the measurements, the design of the principal system components, and the preparation required by the system before measurements can be made.

Chapter 3 also includes measurements that serve to verify theoretical assumptions and design goals concerning sound propagation in our impedance tube, as well as an analysis of errors, uncertainty, and sensitivity that affect all measurements made with our impedance tube. Experimental data are presented in Chapter 4 for both water and bubbly liquids outside the tube. A detailed comparison to the theoretical work of Chapter 2 is also made. Suggestions and preliminary steps towards improving the system are covered in Chapter 5. Chapter 6 provides a concise review of this work, drawing a number of conclusions. This work concludes with a number of Appendices, providing mathematical derivations, technical drawings, computer codes and other supporting information.

Chapter 2

Theoretical Modeling

Even the most exciting experiments must lay their foundations in theory. While we may prefer to be in the laboratory, in the machine shop, or at sea, we experimentalists must be intimately familiar with the theory behind our apparati and that concerning what we intend to measure. With this in mind, this Chapter is divided into two sections. In the first we explore the theoretical modelling of our instrument, a baffled, sound-hard impedance tube. As we seek to measure the properties of bubbly liquids, the second half of this section is therefore devoted to acoustic propagation in bubbly liquids, a fascinating subject with a rich history.

2.1   The baffled, sound hard impedance tube

Impedance tube theory is generally considered very simple and straightforward. Most acoustics textbooks treat it early and in detail as a logical and practical topic when covering

acoustic wave propagation in tubes. We will follow a similar pattern, first discussing the theory of waves in cylindrical tubes and then applying it specifically to the impedance tube. We will then move on to the more complicated mathematics that arise at a tube opening fitted with a sound-hard baffle, as shown in Figure 2.1.

Figure 2.1: The baffled sound hard tube. A pressure wave traveling from the sound source at left hits the baffled opening. Some of the energy is reflected and some is radiated into the fluid outside the tube.

The general problem to be solved in this section is illustrated in this figure. A sound wave with pressure amplitude P_i is excited by the vibrating sound source at the left of the figure, travels to the right in a tube filled with a fluid with sound speed c_1 and density ρ_2. When this wave reaches the tube opening, some of its energy is reflected back to the left as a pressure wave with amplitude P_r while the rest is radiated into the fluid outside the tube (which has a sound speed and density c_2 and ρ_2). We aim to develop an expression for the ratio of the reflected and incident pressure amplitudes, called the *plane wave reflection*

coefficient.

2.1.1 Acoustic wave propagation in a sound hard tube

We will consider sound propagation in a circular tube whose walls are rigid (also known as "sound hard"). The propagation of a linear acoustic wave is governed by the wave equation. It is convenient to express the wave equation for the velocity potential, Φ:

$$\nabla^2 \Phi - \frac{1}{c^2}\frac{\partial^2}{\partial t^2}\Phi = 0 \tag{2.1}$$

where c is the speed of sound of the fluid. The velocity potential is related to the acoustic pressure, p, and velocity, u by

$$p = -\rho \frac{\partial}{\partial t}\Phi \tag{2.2}$$

$$u = \nabla \Phi \tag{2.3}$$

where ρ is the fluid density. For time harmonic excitation, $\Phi = \phi \exp(-i\omega t)$, the wave equation becomes

$$\nabla^2 \phi + k^2 \phi = 0. \tag{2.4}$$

where $k = \omega/c$ is the wave number. This is known as the Helmholtz equation.

For the study of circular tubes, it is convenient to use cylindrical coordinates, (w, θ, z). The radial coordinate is designated w, instead of r, to avoid confusion with the vector $\vec{r}$ used later in this work. The Helmholtz equation in cylindrical coordinates is:

$$\frac{1}{w}\frac{\partial}{\partial w}(w\phi) + \frac{1}{w^2}\frac{\partial^2}{\partial \theta^2}\phi + \frac{\partial^2}{\partial z^2}\phi + k^2\phi = 0 \tag{2.5}$$

If the system is assumed symmetric about the tube axis, then the θ dependence can be neglected. The general axisymmetric solution to Eq. (2.5) is

$$\phi\left(w, z\right) = e^{\pm i k_z z} J_0\left(k_w w\right) \tag{2.6}$$

where $k_w^2 + k_z^2 = k^2$ and J_0 is an ordinary Bessel function of the first kind of order zero. An important property of this Bessel function is

$$\frac{\partial}{\partial w} J_0\left(k_w w\right) = -k_w J_1\left(k_w w\right) \tag{2.7}$$

where J_1 is an ordinary Bessel function of the first kind of order one.
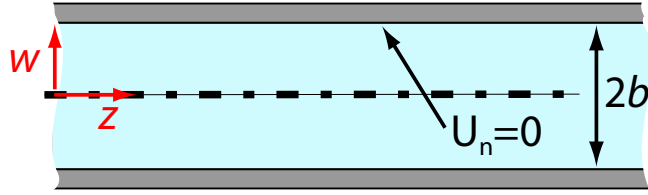
Figure 2.2: The sound-hard tube.

Boundary conditions must be imposed on Eq. (2.6) to determine the relative values of k_z and k_w. We will assume that the tube's walls are rigid ("sound-hard"). This boundary condition is illustrated in Figure 2.2. Mathematically speaking, the radial component of the velocity, u_w is zero at the wall $(w = b)$ of a sound-hard tube:

$$u_w\left(w = b\right) = \left.\frac{\partial}{\partial w}\phi\right|_{w=b} = 0. \tag{2.8}$$

Applying this condition to Eq. (2.6) gives

$$\frac{\partial}{\partial w} J_0\left(k_w b\right) = -\left(k_w b\right) J_1\left(k_w b\right) = 0. \tag{2.9}$$

where use has been made of Eq. (2.7). To satisfy this condition, the product $k_w b$ must be a root of the Bessel function J_1. The velocity potential inside the tube now takes the form of the series solution

$$\phi(w, z) = \sum_{n=0}^{\infty} A_n e^{\pm i k_{zn} z} J_0(k_{wn} w) \tag{2.10}$$

where:

$$k_{wn} = \frac{\alpha_{1n}}{b}$$

$$k_{zn} = \sqrt{k^2 - k_{wn}^2} \tag{2.11}$$

$$J_1(\alpha_{1n}) = 0$$

The roots of first Bessel function, α_{1n}, have been tabulated by many authors (see, for instance [36]).

Noting that $\alpha_{10} = 0$, the velocity potential in a sound-hard can be written:

$$\phi(w, z) = A_0 e^{ikz} + B_0 e^{-ikz} + \sum_{n=1}^{\infty} A_n e^{ik_{zn} z} J_0(k_{wn} w) + B_n e^{-ik_{zn} z} J_0(k_{wn} w) \tag{2.12}$$

Here, the first two terms are plane waves, the first (A_0) travels in the $+z$ direction, the second (B_0) travels in the $-z$ direction. For small values of k (low frequencies), k_{zn} is imaginary. This has an important consequence: the majority of the exponents in the sum are now real. In order to have a bounded solution as z gets large, we must discard the A_n terms for $z < 0$ and the B_n terms for $z > 0$ when k_{zn} is imaginary. The remaining terms will have purely real, negative exponents and will not propagate over a significant distance.

The values of ω for which $kb = \alpha_{1n}$ are known as the cut-off frequencies. Below the first cut-off frequency ($kb = \alpha_{11}$) only plane waves will propagate in a sound-hard tube as all higher order modes have real negative exponents. All modes that do propagate will travel

along the z axis with a phase speed, c_p, given by

$$c_p = \frac{\omega}{k_z}. \tag{2.13}$$

For the plane wave mode, $k_z = k$ and the speed of propagation equals the intrinsic speed of sound of the medium, c. For the higher order modes, the speed of propagation is a function of frequency. Figure 2.3 is a plot of the phase speed of the first three modes in a sound hard tube normalized by c. The cutoff frequency effect is easily seen around $kb \approx 3.8$ (α_{11}) and 7.0 (α_{12}).
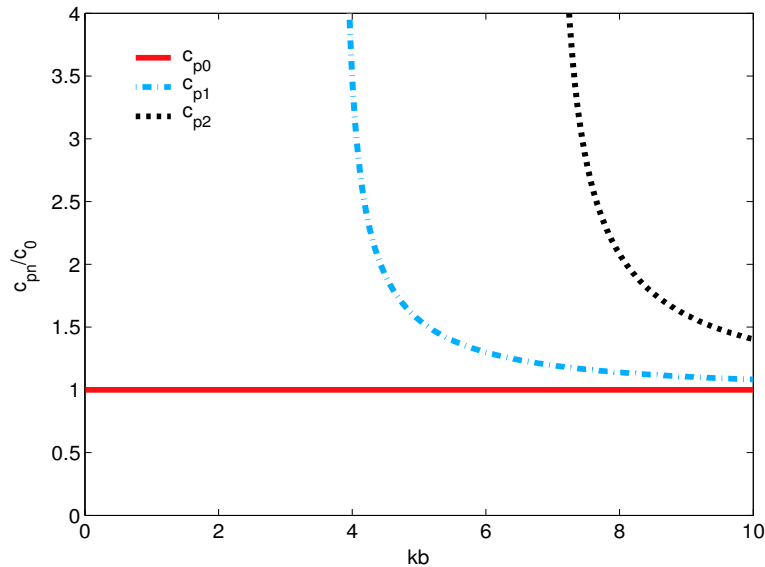
Figure 2.3: Speed of propagation of the first three modes in a sound-hard tube.

2.1.2 General impedance tube theory

As promised, we will now discuss the principles behind the impedance tube. Chapter 3 builds on of the theory developed here providing a bridge to the experimental setup. Most

18

standard acoustics textbooks cover impedance tube theory. The following closely follows

Blackstock [37], whose presentation is straightforward and intuitive. First, the general

definition of impedance is in order. The impedance, Z, of an acoustic wave is defined as

the ratio of the acoustic pressure and velocity at a given point,

$$Z = \frac{p}{u}. \tag{2.14}$$

Now consider a sound-hard tube of length L, with some sort of source at $z = 0$ (Figure

2.4). This source vibrates at frequency ω in such a way that it only excites a plane wave.

This plane wave will travel to the right with pressure amplitude A until it hits a uniform

impedance termination, Z_n, at $z = L$. At this point, some of the waves' energy is trans-

mitted through the termination ($+z$ direction) while the remaining is reflected as a plane

wave with pressure amplitude B. The pressure and velocity anywhere in the tube can be

written as (neglecting the $\exp(-i\omega t)$ time dependence):

$$\begin{aligned} p(z) &= Ae^{ikz} + Be^{-ikz} \\ u_z(z) &= \frac{-i}{\rho\omega}\frac{\partial}{\partial z}p(z) = \frac{1}{\rho c}\left(Ae^{ikz} - Be^{-ikz}\right) \end{aligned} \tag{2.15}$$

It is important to note that both A and B can be, and often are, complex quantities.
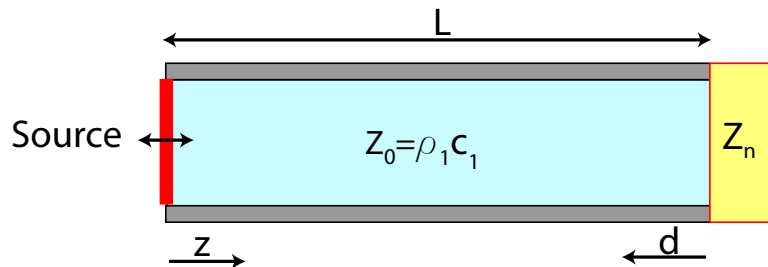
Figure 2.4: Tube terminated with unknown impedance, Z_n.

At $z = L$ we define an incident pressure, P_i, and a reflected pressure, P_r:

$$P_i = Ae^{ikL}$$
$$P_r = Be^{-ikL} = \Re P_i$$

(2.16)

Here $\Re$ is defined as the *plane wave reflection coefficient.* It is the ratio of the reflected and incident acoustic pressures. Changing the coordinate z to $d = L - z$ and combining Eqs. (2.15) and (2.16), the pressure and particle velocity anywhere in the tube can be written as

$$p(d) = P_i \left(e^{-ikd} + \Re e^{ikd} \right)$$
$$u_z(d) = \frac{P_i}{Z_0} \left(e^{-ikd} - \Re e^{ikd} \right).$$

(2.17)

Here Z_0 is the specific acoustic impedance of the medium inside the tube, $Z_0 = \rho c$. By Eq. (2.14), the acoustic impedance anywhere in the tube is

$$Z(d) = Z_0 \frac{e^{-ikd} + \Re e^{ikd}}{e^{-ikd} - \Re e^{ikd}}.$$

(2.18)

In particular, the impedance at the end of the tube, $d = 0$, must equal the termination impedance, Z_n:

$$Z_n = Z_0 \frac{1 + \Re}{1 - \Re}.$$

(2.19)

This is an important result because many techniques exist for measuring the plane wave reflection coefficient experimentally – and if $\Re$ is known, so is the termination impedance. The termination impedance is very often a strong function of the speed of sound and attenuation of the material at $z > L$. Indeed, if the tube were terminated with an infinitely long sample, the termination impedance would equal the specific impedance ($\rho_n c_n$) of that fluid. Section 3.1 explains the experimental method used to measure $\Re$, the single-hydrophone transfer function method.

2.1.3 Radiation from an open, baffled tube

Now consider the setup shown in Figure 2.1 where sound propagating down a sound-hard tube reaches the tube opening, fitted with a sound-hard baffle that extends infinitely in all directions (or is so large compared to the wavelength of sound that it may be considered infinite). For the time being, it shall be assumed that the fluid outside the tube is the same as that inside. It is convenient to define $z = 0$ at the tube opening so the baffle lies in the (x, y) plane and only negative values of z exist in the tube as shown in Figure 2.5. To ensure a bounded solution as $z \to -\infty$ in the tube, the A_n terms in Eq. (2.12) must be set to zero. The incident wave, traveling from left to right, is assumed to be plane and of such magnitude that $A_0 = 1$. The velocity potential, pressure, and particle velocity (in the direction of propagation) anywhere in the tube are given by[1]:

$$
\begin{aligned}
\phi(w, z) &= e^{ikz} + \Re e^{-ikz} + \sum_{n=1}^{\infty} B_n e^{-ik_{zn}z} J_0(k_{wn}w) \\
p(w, z) &= i\rho\omega \left(e^{ikz} + \Re e^{-ikz} + \sum_{n=1}^{\infty} B_n e^{-ik_{zn}z} J_0(k_{wn}w) \right) \\
u_z(w, z) &= ik \left(e^{ikz} - \Re e^{-ikz} \right) - i \sum_{n=1}^{\infty} B_n k_{zn} e^{-ik_{zn}z} J_0(k_{wn}w)
\end{aligned}
\tag{2.20}
$$

Here $\Re = B_0$ is the plane wave reflection coefficient, defined in Section 2.1.2.

The quantity of most interest turns is the particle velocity at the tube opening:

$$
u_z(w, 0) = ik(1 - \Re) - i \sum_{n=1}^{\infty} B_n k_{zn} J_0(k_{wn}w)
\tag{2.21}
$$

Aside from the tube opening, the rest of the (x, y) plane comprises the rigid baffle. As such,

---

[1]One may notice that the units for these expressions are not accurate. This is because we have neglected the units associated with the coefficients A_n and B_n when we set $A_0 = 1$. This simplification makes the derivation easier to follow so long as the reader remembers to attach "phantom" units of [length^2/time] to the equations.
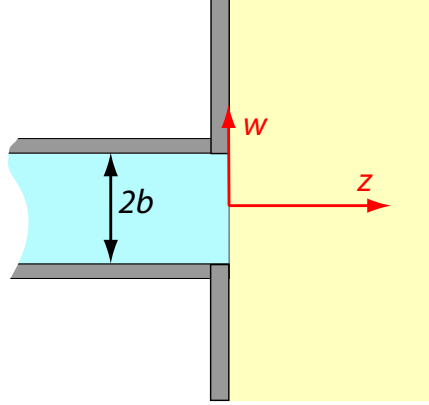
Figure 2.5: The cylindrical coordinate system with its origin on the plane of the tube opening.

the particle velocity normal (outward) to this plane is defined everywhere:

$$u_n(x, y) = \begin{cases} -u_z(w, 0) & x^2 + y^2 = w^2 \leq b^2 \\ 0 & x^2 + y^2 > b^2 \end{cases}. \tag{2.22}$$

This formulation makes it relatively straightforward to solve for the acoustic field outside the tube using a Green's function approach. This method is described in detail in Appendix B. The solution for the velocity potential outside the tube is given by:

$$\phi(\overrightarrow{r}) = \frac{-1}{4\pi} \iint\limits_{S_0} \phi(\overrightarrow{r_0}) \frac{\partial}{\partial n_0} G(\overrightarrow{r}|\overrightarrow{r_0}) - G(\overrightarrow{r}|\overrightarrow{r_0}) \frac{\partial}{\partial n_0} \phi(\overrightarrow{r_0}) \, dS_0 \tag{2.23}$$

where $\overrightarrow{r} = (x, y, z)$, $\overrightarrow{r_0} = (x_0, y_0, z_0)$, $G(\overrightarrow{r}|\overrightarrow{r_0})$ is a Green's function, and S_0 is a surface bounding the region of interest. In this case the region is the area outside the tube, defined by the tube opening and rigid baffle on the (x_0, y_0) plane and closed by a hemisphere of infinite radius in the positive z direction (Figure 2.6). This is a very convenient surface, as the normal derivative of the velocity potential, $\partial \phi(\overrightarrow{r_0})/\partial n_0$, is defined everywhere on the (x_0, y_0) plane by Eq. (2.22). The Sommerfeld radiation condition states that all acoustic

22

quantities are zero at infinity, allowing us to neglect the hemisphere portion of the bounding surface.
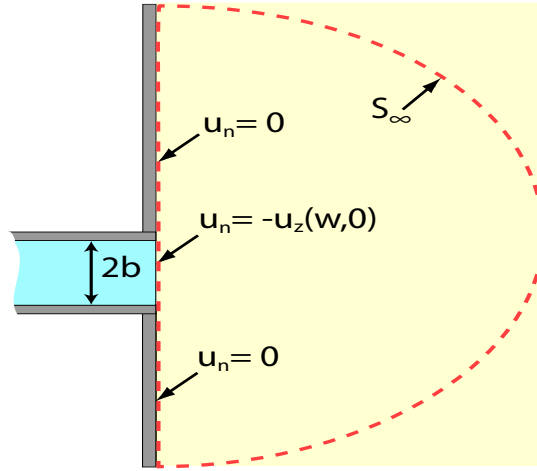
Figure 2.6: The integration surface used to evaluate Eq. (2.23)

Equation (2.23) can be greatly simplified if a Green's function is chosen such that its normal derivative, $\partial G\left(\vec{r}\,|\vec{r_0}\right)/\partial n_0$, is zero everywhere on the (x_0, y_0) plane. One such Green's function is (see Appendix B, Eq. (B.9))

$$G\left(\vec{r}\,|\vec{r_0}\right) = \frac{2e^{ik\left|\vec{r}-\vec{r_0}\right|}}{\left|\vec{r}-\vec{r_0}\right|} \tag{2.24}$$

where $\vec{r_0} = (x_0, y_0, 0)$ is the plane defined by $z_0 = 0$. Combining Eqs. (2.22), (2.23), and (2.24), the velocity potential outside the tube can be expressed as:

$$\phi\left(\vec{r}\right) = \frac{-1}{4\pi} \iint\limits_{x_0^2+y_0^2<b^2} \frac{2e^{ik\left|\vec{r}-\vec{r_0}\right|}}{\left|\vec{r}-\vec{r_0}\right|} \left[ik\left(1-\Re\right) - i\sum_{n=1}^{\infty} B_n k_{zn} J_0\left(k_{wn}w_0\right)\right] dx_0 dy_0. \tag{2.25}$$

23

As tempting as it may be to solve this equation now, the B_n terms remain undefined. However, the velocity potential given by Eq. (2.25) above for the field outside the tube must equal that given by Eq. (2.20) for the field inside the tube at the tube opening, $z = 0$:

$$1 + \Re + \sum_{n=1}^{\infty} B_n J_0\left(k_{wn}w\right) = \frac{-1}{4\pi} \int_0^{2\pi} \int_0^b \frac{2e^{ikR}}{R} \left[ik\left(1 - \Re\right) - i\sum_{n=1}^{\infty} B_n k_{zn} J_0\left(k_{wn}w_0\right)\right] w_0 \, dw_0 \, d\theta_0.$$

(2.26)

Here $R = |\vec{r} - \vec{r_0}| = \sqrt{(x - x_0)^2 + (y - y_0)^2} = \sqrt{w^2 + w_0^2 - 2ww_0 \cos\left(\theta - \theta_0\right)}$ and the (x_0, y_0) coordinates have been transformed to polar coordinates, (w_0, θ_0). For a given frequency and set of material properties the only unknowns in Eq. (2.26) are the coefficients of the Bessel functions, B_n, and the reflection coefficient, $\Re$. Using the orthogonality relationships of Bessel functions, it may be possible to solve for these coefficients, although no closed-form solutions exist in the open literature. Normura et al. [38] published a solution in 1960 as a coupled system of two infinite sets of linear equations, which must be solved numerically. Norris and Sheng [39] present a solution for $\Re$ as a single system of infinite linear equations. Their solution also requires numerical computation of the remaining co-efficients, B_n. Both of these solutions deviate very little from that developed here over the frequency range of interest. The work of Norris and Sheng is discussed in more detail in Appendix C.

Although Eq. (2.25) cannot be solved directly, it can be simplified tremendously with a single assumption. As the incident wave is plane, it is reasonable to assume that the wave-front at the tube opening remains sufficiently plane to neglect any radial curvature. With this assumption we can discard the Bessel functions. This assumption is most valid below

24

the first cutoff mode of the tube, where only plane waves (i.e., without radial curvature) can propagate. The velocity potential outside the tube is now

$$\phi\left(\overrightarrow{r}\right) = \frac{-U_z}{2\pi} \int_0^{2\pi} \int_0^b \frac{e^{ik\left|\overrightarrow{r}-\overrightarrow{r_0}\right|}}{\left|\overrightarrow{r}-\overrightarrow{r_0}\right|} w_0 dw_0 d\theta_0 \tag{2.27}$$

where $U_z = ik\left(\Re - 1\right)$ is the normal velocity[2] at the tube opening. Although this expression is significantly simpler, it is still difficult to evaluate for all $\overrightarrow{r}$. A number of authors have evaluated this integral for specific conditions: on the tube opening itself $(z = 0)$, along the propagation axis $(w = 0)$, in the far field $\left(\sqrt{x^2 + y^2 + z^2} >> w_0\right)$, and in the Rayleigh limit $(kb << 1)$. The first two are the most relevant to the present work.

2.1.4 Radiation along the tube axis

Consider the propagation of sound along the axis of the tube, $(w = 0)$. The pressure at a distance z from the tube opening is given by:

$$p\left(z\right) = \frac{i\rho\omega U_z}{2\pi} \int_0^{2\pi} \int_0^b \frac{e^{ik\left(w_0^2 + z^2\right)^{1/2}}}{\left(w_0^2 + z^2\right)^{1/2}} w_0 dw_0 d\theta_0 \tag{2.28}$$

The integration over θ_0 is straightforward and contributes a factor of 2π. With the change of variables $\nu = \left(w_0^2 + z^2\right)^{1/2}$, the pressure field along the axis can be expressed as:

$$p\left(z\right) = i\rho\omega U_z \frac{(-i)}{k} \int_z^{\left(z^2 + b^2\right)^{1/2}} e^{ik\nu} d\nu. \tag{2.29}$$

Evaluating the remaining integral the pressure is

$$p\left(z\right) = \rho c U_z \left[e^{ik\left(b^2 + z^2\right)^{1/2}} - e^{ikz}\right] \tag{2.30}$$

---

[2]See Footnote 1 for an explanation of the units of this term.

25

which is often written [40]:

$$p\left(z\right) = \left(2i\right)\left(\rho c U_z\right)\exp\left(\frac{ik}{2}\left(\left(z^2+b^2\right)^{1/2}+z\right)\right)\sin\left(\frac{k}{2}\left(\left(z^2+b^2\right)^{1/2}-z\right)\right). \quad (2.31)$$

Equation (2.31) is plotted in Figure 2.7 for three different values of the non-dimensional wavenumber kb. There is a very apparent transition from the near to far field.
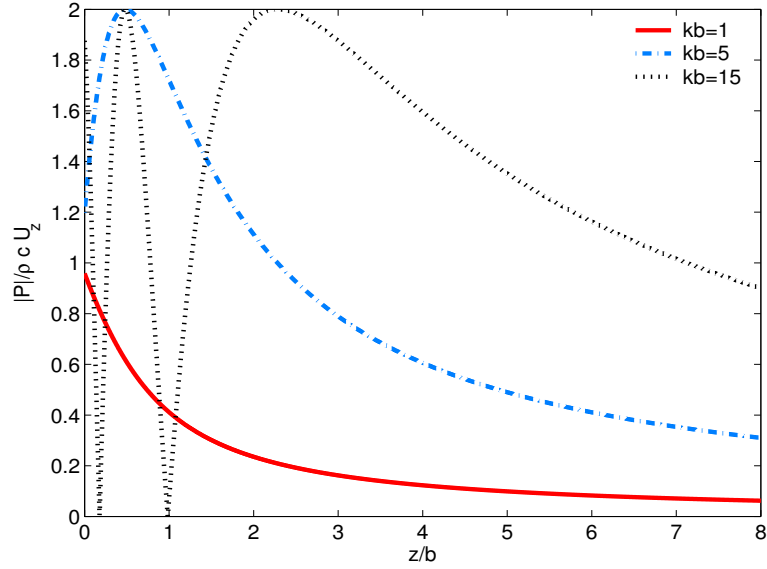
Figure 2.7: Magnitude of the radiated pressure along the tube axis.

2.1.5 Radiation impedance of the baffled tube

Calculating the pressure at the tube opening ($z = 0$) is more difficult. It is easier to consider the *average* pressure,

$$p_{ave}\big|_{z=0} = \left(\frac{1}{\pi b^2}\right)\int\limits_0^{2\pi}\int\limits_0^b \frac{-i\rho\omega U_z}{2\pi}\iint\limits_{x_0^2+y_0^2<b^2}\frac{e^{ikR}}{R}dx_0 dy_0 w dw d\theta. \quad (2.32)$$

26

Notice that we have returned to the (x_0, y_0) coordinate system for the time being. By Eq. 2.14, the average acoustic impedance, Z, at the opening is:

$$Z = \left(\frac{1}{\pi b^2}\right) \frac{-i\rho\omega}{2\pi} \int_0^{2\pi} \int_0^b \iint_{x_0^2+y_0^2<b^2} \frac{e^{ikR}}{R} dx_0 dy_0 w dw d\theta. \tag{2.33}$$

This quadruple integral is often called the Helmholtz integral. This integral was first applied to acoustics by Rayleigh [41] in 1878, studying the impedance of a vibrating rigid disc in an infinite rigid baffle. He reckoned, as we do, that to a first approximation a tube opening can be modelled as having a uniform velocity profile and therefore has the same impedance as the rigid vibrating disc. His work was revisited by Warren [42] in 1928, applying the solution to loudspeakers. McLachlan [43], also working with loudspeakers, was the first to present the solution in the modern form and considered other, non-uniform, velocity distributions in 1932.

There are two classical mathematical tricks used to solve Eq. (2.33). The first is to restrict the range of integration such that only points where $x_0^2 + y_0^2 < w^2$ are considered. In doing this the problem is effectively divided in half and the result must be multiplied by two[3]:

$$Z = \left(\frac{1}{\pi b^2}\right) \frac{-i\rho\omega}{\pi} \int_0^{2\pi} \int_0^b \iint_{x_0^2+y_0^2<w^2} \frac{e^{ikR}}{R} dx_0 dy_0 w dw d\theta \tag{2.34}$$

The second trick is a brilliant coordinate transform which Rayleigh [41], attributed to James

_____

[3]Eq. (2.33) can be written:

$$Z = \left(\frac{1}{\pi b^2}\right) \frac{-i\rho\omega}{2\pi} \left\{ \int_0^{2\pi} \int_0^b \iint_{x_0^2+y_0^2<w^2} \frac{e^{ikR}}{R} dx_0 dy_0 w dw d\theta + \int_0^{2\pi} \int_0^b \iint_{x^2+y^2<w_0^2} \frac{e^{ikR}}{R} dx dy w_0 dw_0 d\theta_0 \right\}$$

but as R is invariant under $(x, y) \leftrightarrow (x_0, y_0)$ the quadruple integrals are equal to each other.

27

Clerk Maxwell in an 1871 paper [44] [4]. The transformed coordinate system, (x'_0, y'_0), has its origin at the point (x, y) and is aligned such that the origin of the (x, y) and (x_0, y_0) axes lies at $x'_0 = w$. We then consider a vector pointing from the origin of the new coordinate system to some point (x_0, y_0) inside the circle defined by $x_0^2 + y_0^2 < w^2$. As shown in Figure 2.8, we transform the new coordinate system into a cylindrical system defined by:

$$x'_0 = R \cos \varphi_0$$
$$y'_0 = R \sin \varphi_0$$

(2.35)

Here R is the distance from (x, y), the origin of (x'_0, y'_0), to (x_0, y_0):

$$R = \sqrt{(x - x_0)^2 + (y - y_0)^2}.$$

This is the same R in Eq. (2.34)! Switching the variables in (2.34) from (x_0, y_0) to (x'_0, y'_0) and change to cylindrical coordinates via (2.35) to obtain:

$$Z = \left(\frac{1}{\pi b^2} \right) \frac{-i\rho\omega}{\pi} \int_0^{2\pi} \int_0^b \iint\limits_{x_0^2 + y_0^2 < w^2} e^{ikR} dR d\varphi_0 w dw d\theta$$

(2.36)

Without the R in the denominator, it is a much easier integral to evaluate.

All that remains before Eq. (2.36) can be evaluated is to determine the limits of integration on R and ϕ_0. The largest allowable value of (x_0, y_0) is (x, y). As shown in Figure 2.9, the limit on R is $R_{\max} = 2w \cos \varphi_0$ and φ_0 is limited to values for which $x'_0 > 0$, that is, $-\pi/2 < \varphi_0 < \pi/2$. The impedance integral is now in a relatively easy to solve form:

$$Z = \left(\frac{1}{\pi b^2} \right) \frac{-i\rho\omega}{\pi} \int_0^{2\pi} \int_0^b \int_{\frac{-\pi}{2}}^{\frac{\pi}{2}} \int_0^{2w \cos \varphi_0} e^{ikR} dR d\varphi_0 w dw d\theta$$

(2.37)

---

[4]Rayleigh incorrectly cites the date of his paper as 1870, which was the date it was submitted to the Royal Society. The full and accurate reference is given the bibliography. It should also be noted that Rayleigh, then John William Strutt (his father, the Baron Rayleigh, had yet to die), and not Maxwell, was the author of the paper cited by Rayleigh in *The Theory of Sound*. Rayleigh merely mentions Maxwell's assistance in solving a similar integral in the paper.
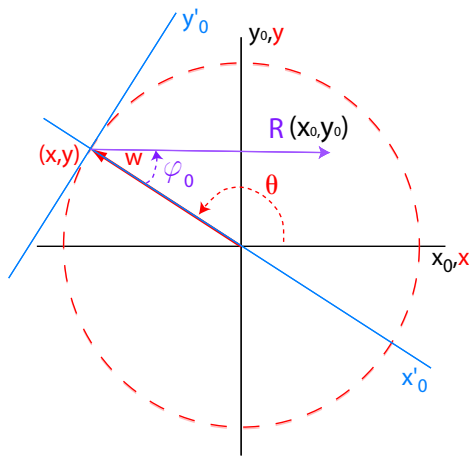
Figure 2.8: The (x'_0, y'_0) coordinate transform.
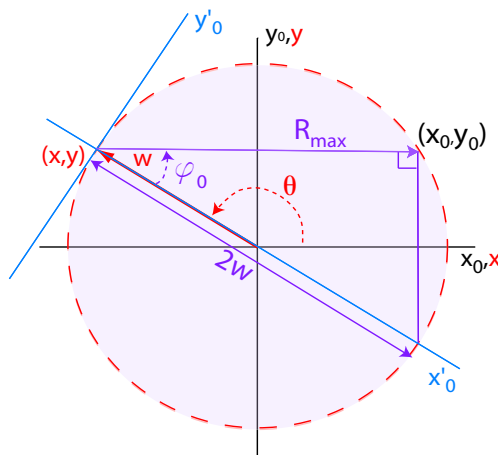
Figure 2.9: The limits of integration on R and φ_0.

The straightforward R and θ integrations give us:

$$Z = \left(\frac{1}{\pi b^2}\right)(-2\rho c\pi)\int_0^b \left(\frac{1}{\pi}\int_{-\frac{\pi}{2}}^{\frac{\pi}{2}} e^{i2kw\cos\varphi_0}d\varphi_0 - 1\right)wdw \qquad (2.38)$$

As the cosine is an even function we need only consider half the interval in the φ_0 integration and multiply the result by 2. Breaking the complex exponential function via Euler's formula the integral becomes:

$$Z = \left(\frac{-1}{\pi b^2}\right)(2\rho c\pi)\int_0^b \left(\frac{2}{\pi}\int_0^{\frac{\pi}{2}}\cos(2kw\cos\varphi_0)\,d\varphi_0 - 1 + i\frac{2}{\pi}\int_0^{\frac{\pi}{2}}\sin(2kw\cos\varphi_0)\,d\varphi_0\right)wdw$$

$$(2.39)$$

Rayleigh recognized the first φ_0 integral as a definition of the Bessel function J_0. He expanded the second integral in a power series and called the function K_0. McLachlan [43], citing the extensive work of Watson [36], recognized the second integral as a definition of the Struve function, $\mathbf{H_0}$ (the boldface notation is commonplace for Struve functions). These definitions are repeated here for reference:

$$J_0(2kw) = \frac{2}{\pi}\int_0^{\frac{\pi}{2}}\cos(2kw\cos\varphi_0)\,d\varphi_0$$
$$\mathbf{H_0}(2kw) = \frac{2}{\pi}\int_0^{\frac{\pi}{2}}\sin(2kw\cos\varphi_0)\,d\varphi_0$$

The average impedance at the tube opening is now given by:

$$Z = \left(\frac{-1}{\pi b^2}\right)(2\rho c\pi)\int_0^b (J_0(2kw) - 1 + i\mathbf{H_0}(2kw))\,wdw. \qquad (2.40)$$

The following properties of the Bessel and Struve functions are useful in evaluating the remaining integral (for more information see [41, 36, 40]):

$$xJ_0(x) = \frac{d}{dx}(xJ_1(x))$$

$$x\mathbf{H_0}(x) = \frac{d}{dx}(x\mathbf{H_1}(x))$$

30

Using these properties and the transform $x = 2kw$ we can write (2.40) as:

$$Z = \left(\frac{1}{\pi b^2}\right)(2\rho c\pi)\left(\frac{b^2}{2} - \frac{1}{(2k)^2}\int_0^{2kb}\frac{d}{dx}\left(xJ_1\left(x\right)\right)dx - i\int_0^{2kb}\frac{d}{dx}\left(x\mathbf{H_1}\left(x\right)\right)dx\right). \quad (2.41)$$

Evaluating the remaining integrals and rearranging, the impedance is given by:

$$Z = \rho c\left(1 - \frac{1}{kb}J_1\left(2kb\right) - i\frac{1}{kb}\mathbf{H_1}\left(2kb\right)\right). \quad (2.42)$$

Equation (2.42) is commonly written [40, 45, 46, 47]:

$$Z = \rho c\left(R\left(2kb\right) - iX\left(2kb\right)\right)$$

$$R\left(2kb\right) = 1 - \frac{2}{2kb}J_1\left(2kb\right) \quad . \quad (2.43)$$

$$X\left(2kb\right) = \frac{2}{2kb}\mathbf{H_1}\left(2kb\right)$$

Here $R\left(2kb\right)$ is the real part of the impedance, or the resistance, and $X\left(2kb\right)$ is the imaginary part, or reactance.

While the Bessel function in the resistance is commonplace in most numerical solvers, the Struve function in the reactance is not. Computation of the reactance has historically been achieved through a truncated series expansion. A recent paper [48] proposes a numerical approximation for $\mathbf{H_1}\left(x\right)$ which the authors claim to have an absolute error on $[0,\infty)$ of less than 0.005. The approximation is repeated here for reference:

$$\mathbf{H_1}\left(x\right) \approx \frac{2}{\pi} - J_0\left(x\right) + \left(\frac{16}{\pi} - 5\right)\frac{\sin\left(x\right)}{x} + \left(12 - \frac{36}{\pi}\right)\frac{1 - \cos\left(x\right)}{x^2}. \quad (2.44)$$

Using this formula, values of the reactance and resistance are plotted in Figure 2.10.

2.1.6   Reflection from a baffled tube opening

We now have all the pieces needed to determine the plane wave reflection coefficient from a baffled tube opening. To determine how the reflection coefficient is governed by the
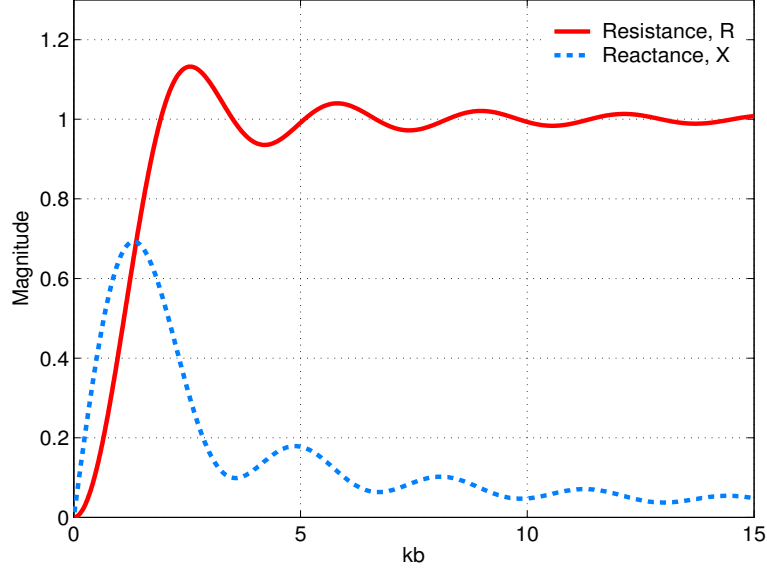
Figure 2.10: Resistance and reactance at the opening of a baffled tube as a function of kb.

impedance at the tube opening, we rewrite Eq. (2.19) as:

$$\Re = \frac{Z_n - Z_0}{Z_n + Z_0}. \tag{2.45}$$

We then let the termination impedance, Z_n, equal the average impedance at the tube opening, Z, given by Eq. (2.43). If the fluid at the tube opening is the same as the fluid inside the tube, the reflection coefficient for the baffled, sound-hard tube is given by:

$$\Re = \frac{R(2kb) - 1 - iX(2kb)}{R(2kb) + 1 - iX(2kb)} \tag{2.46}$$

which is a complex quantity. If the two fluids are different, the reflection coefficient becomes (denoting the fluids inside and outside the tube with subscripts 1 and 2, respectively):

$$\Re = \frac{R(2k_2 b) - \gamma - iX(2k_2 b)}{R(2k_2 b) + \gamma - iX(2k_2 b)} \tag{2.47}$$

where $\gamma = \rho_1 c_1 / \rho_2 c_2$. The validity of these equations is explored in Appendix C, comparing them to other published results and numerical models. Figure 2.11 shows the predicted

32

reflection coefficient for three different values of γ.
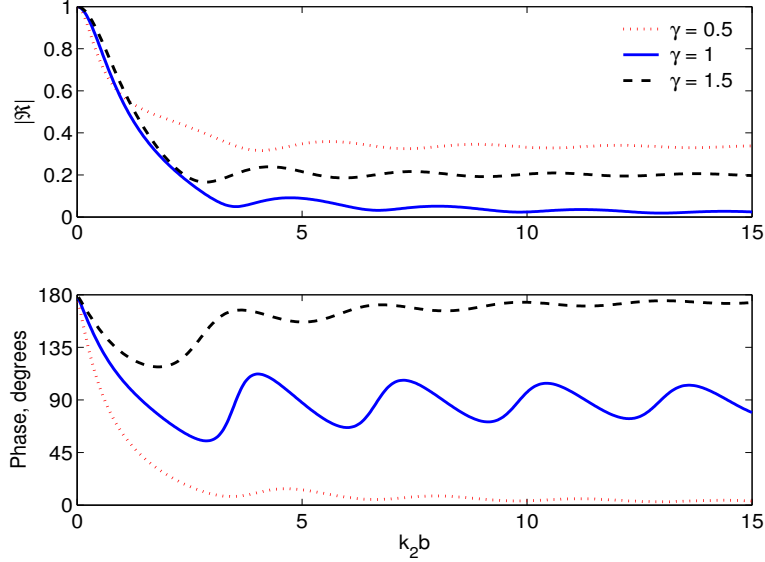
Figure 2.11: Magnitude and phase of the reflection coefficient predicted by Eq. (2.47) for three different values of γ, the ratio of specific impedances.

2.1.7 Other tube terminations

We have derived an expression for the plane-wave reflection coefficient for a tube opening fitted with an infinite, rigid baffle. Much work has been done developing solutions for tubes terminated with other openings and, although these solutions will not be discussed in detail, they merit mentioning. The most well-known is the solution for an unflanged opening of a tube with vanishingly small wall thickness, published in 1948 by Levine and Schwinger [49]. They present a solution for the plane wave reflection coefficient in closed form,

$$\Re = -|\Re|e^{2ik\ell} \tag{2.48}$$

where

$$|\Re| = \exp\left(-\frac{2kb}{\pi}\int_0^{kb}\frac{\tan^{-1}\left(-J_1\left(x\right)/N_1\left(x\right)\right)}{x\sqrt{\left(kb\right)^2-x^2}}dx\right) \tag{2.49}$$

and

$$\ell = \frac{b}{\pi}\int_0^{kb}\frac{\ln\left(\pi J_1\left(x\right)\sqrt{\left(J_1\left(x\right)\right)^2+\left(N_1\left(x\right)\right)^2}\right)}{x\sqrt{\left(kb\right)^2-x^2}}dx+\frac{b}{\pi}\int_0^{\infty}\frac{\ln\left(1/\left(2I_1\left(x\right)K_1\left(x\right)\right)\right)}{x\sqrt{\left(kb\right)^2+x^2}}dx. \tag{2.50}$$

Here $N_1\left(x\right)$ is an ordinary Bessel function of the second kind and $I_1\left(x\right)$ and $K_1\left(x\right)$ are modified Bessel functions of the first and second kind, respectively.

Jones [50] adapted Levine and Schwinger's work to study the scattering of waves off solid tubes of finite thickness. Ando [51] investigated the reflection from the opening of a tube of finite thickness, deriving a solution in the form of an infinite number of simultaneous equations (which may be truncated for certain thickness to diameter ratios) in 1969. In 1996, Bernard and Denardo [52] cast Ando's results in a more useful form. More recently, numerical methods, such as the finite element method, finite difference method, and boundary element method, have been used to solve for a variety of different tube termination geometries [53, 54].

The theoretical solutions for the plane wave reflection coefficient of unflanged and finite-thickness tubes require that the fluid inside the tube be the same as the fluid outside. This makes them of little use to us in their present form, as we are interested in the case where the two fluids are different. We can, however, apply a first-order correction to approximate the reflection coefficient for the two-fluid case. As we saw in the previous sections, the reflection coefficient for a specific tube termination is a function of both the specific acoustic

impedance inside the tube, Z_0, and the impedance at the tube opening, Z_n. However, so long as only plane waves exist at the tube opening, the impedance at the opening is the same as that of a uniformly vibrating disc and *only depends on the fluid outside the tube.* We have seen that this is indeed the case for the impedance of a baffled tube opening as developed here (see Eq. 2.43).

The correction procedure is as follows. First, let both the fluid inside and outside the tube be the same, with density and sound speed ρ_2 and c_2. The impedance at the tube opening is given by Eq. (2.19),

$$Z_n = \rho_2 c_2 \frac{1 + \Re'}{1 - \Re'},$$

where $\Re'$ is the plane wave reflection coefficient predicted by the single-fluid model. We will assume, as stated above, that this impedance is independent of the fluid inside the tube. Letting the fluid inside the tube have a different density and sound speed, ρ_1 and c_1, the reflection coefficient becomes

$$\Re = \frac{Z_n - \rho_1 c_1}{Z_n + \rho_1 c_1} \approx \frac{(1 - \gamma) + \Re'(1 + \gamma)}{(1 + \gamma) + \Re'(1 - \gamma)} \tag{2.51}$$

where, as before, $\gamma = \rho_1 c_1 / \rho_2 c_2$. Again, this relationship is only a first-order correction and may not hold if higher-order modes play a significant role at the tube opening.

2.2   Bubbly Liquids

Now that we have detailed the theory behind the measurement device we will delve deeper into the theory of what we intend to measure – bubbly liquids. We will start our analysis as we did in Chapter 1 – with the behavior of a single, oscillating bubble.

2.2.1 Bubble dynamics - The bubble as a simple harmonic oscillator

A number of models exist (see [30], pages 302-308) that attempt to explain the linearized dynamics of an oscillating gas bubble in a liquid. For small amplitude radial oscillations about the bubble's equilibrium radius, a_0,

$$a\left(t\right) = a_0 + s\left(t\right) \tag{2.52}$$

where $|s| << a_0$, all the models linearize to the same differential equation that governs a damped harmonic oscillator (see, for instance, [25, 26]),

$$\frac{d^2}{dt^2}s + 2b\frac{d}{dt}s + \omega_0^2 s = 0. \tag{2.53}$$

Here b is a damping coefficient and ω_0 is the resonant frequency given (for now) by Eq. (1.1) and we have neglected any acoustic or hydrodynamic forcing. For resonating air bubbles in water, the damping coefficient is given in Devin's 1959 paper [25] and has three components, radiation damping, viscous damping, and thermal damping which sum together linearly:

$$b = b_{rad} + b_{vis} + b_{th}. \tag{2.54}$$

Expressions for these terms (for all driving frequencies) will be given in the next section. As Devin's work focused on resonating bubbles, in his work each of these terms are a function of bubble size only (and not driving frequency).

The assumption that an oscillating bubble can be modelled as a damped harmonic oscillator is a very important step in the derivation of the speed of sound in bubbly liquids. The simplest way to convince the reader skeptical of applying a linear oscillator model to

a bubble is to present some experimental data (my apologies to those who would object to the presence of measured data in the theory chapter). Figure 2.12 is a plot of the acoustic pressure radiated to the far-field as a 1.45 mm air bubble breaks off a needle in water. The act of breaking off the needle excites the bubble's natural mode which radiates an acoustic pressure that, in the far field, is proportional to the oscillating bubble's radius with time. Also plotted is the impulse response of Eq. (2.53) using the damping coefficient predicted by Devin for a bubble of this size (the bubble was sized using the measured natural frequency and the amplitude of the response was fitted to the data). The model predicts the response of the bubble, especially the decay, after it breaks off the needle completely, very well.
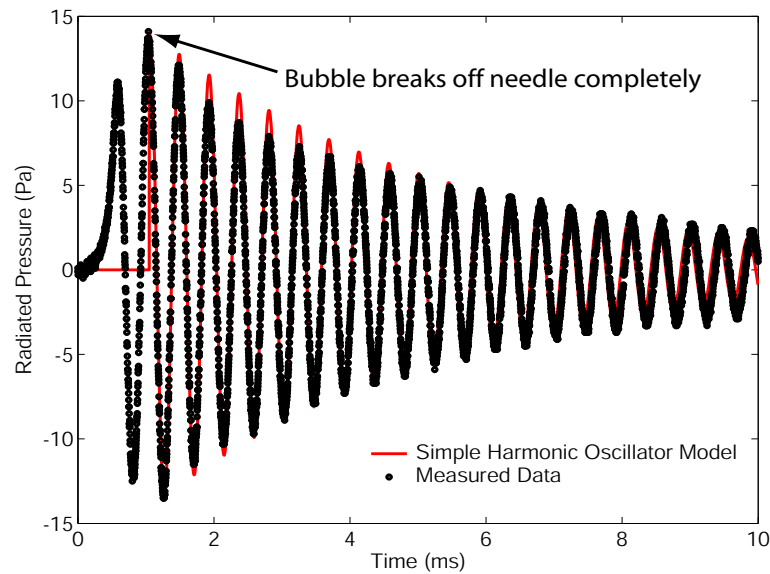
Figure 2.12: The damped harmonic oscillator model for a 1.45-mm air bubble in water is compared with measured data. The only fitting parameter is the pressure amplitude.

37

2.2.2 Sound propagation in bubbly liquids

There are many different approaches to deriving the equations that govern sound propagation in a bubbly liquid. Spitzer [15] and Foldy [16] used a point-scatter approach while Commander and Prosperetti [29] used the continuity and conservation of mass approach of van Wijngaarden [55]. The approach taken here, which may be the most intuitive, begins with Wood's Equation and uses the damped harmonic oscillator bubble model to account for bubble dynamics. This method was first reported by Kuhl, et al. [17] working in Germany during WWII and has also been adopted by Carey [56] and Carey and Roy [57]. Recall from Chapter 1 that the sound speed for a bubbly liquid at low frequencies is given by Wood's Equation is

$$\frac{1}{c_m^2} = \left[(1 - \beta) \, \rho_\ell + \beta \rho_g \right] \left[(1 - \beta) \, \kappa_\ell + \beta \kappa_g \right]. \tag{2.55}$$

It was stated in Section 1.2 that for low frequencies, the compressibility of the bubbles was the same as the isothermal compressibility of the gas inside them. At higher frequencies, bubble dynamics become important and the compressibility of the bubble differs from that of the gas, $\kappa_g \to \kappa_b \, (\omega)$. We will explore these effects now.

In general, the compressibility of the gas phase (bubbles) of the mixture is defined as the change in gas volume with acoustic pressure normalized by the instantaneous volume:

$$\kappa_b = \frac{1}{\rho_g} \left(\frac{\partial p}{\partial \rho_g} \right)^{-1} = \frac{-1}{V_g} \frac{\partial V_g}{\partial p}. \tag{2.56}$$

where p is acoustic pressure, and ρ_g and V_g are the density and volume of the gas phase,

respectively. The volume of gas in a given control volume, V_m is

$$V_g = \frac{4}{3}\pi V_m \int_0^\infty \wp(a)\, a^3 da \qquad (2.57)$$

where $\wp(a)$ is the bubble radius probability density function (the number of bubbles per unit volume with equilibrium radius between a and $a + da$). The void fraction can be expressed in this notation as

$$\beta = \frac{V_g}{V_m} = \frac{4}{3}\pi \int_0^\infty \wp(a)\, a^3 da. \qquad (2.58)$$

Plugging (2.57) into (2.56), the bubble compressibility is

$$\kappa_b = -4\pi \frac{1}{\beta} \int_0^\infty \wp(a)\, a^2 \left(\frac{\partial a}{\partial p}\right) da. \qquad (2.59)$$

The problem is now to determine an expression for $\partial a/\partial p$.

As shown in the previous section, a bubble driven at low acoustic pressures behaves as a linear, damped harmonic oscillator. Adding an acoustic forcing pressure, $P_a e^{-i\omega t}$, to Eq. (2.53) the bubble radius is governed by the differential equation (see [26] or [30], page 372)

$$\frac{d^2}{dt^t}s + 2b\frac{d}{dt}s + \omega_0^2 s = \frac{-P_a}{\rho_\ell a_0}e^{-i\omega t}. \qquad (2.60)$$

The negative sign on the right hand side arises as an increase in acoustic pressure results in a decrease in bubble size in the limit of zero frequency. The steady-state solution for the bubble radius is

$$a(t) = a_0 + \mathrm{Re}\left(\frac{-P_a e^{-i\omega t}}{\rho_\ell a_0 (\omega_0^2 - \omega^2 + i2b\omega)}\right). \qquad (2.61)$$

The partial derivative in (2.59) can now be evaluated as

$$\frac{\partial a}{\partial p} = \frac{-1}{\rho_\ell a_0 (\omega_0^2 - \omega^2 + i2b\omega)}. \qquad (2.62)$$

39

The bubble compressibility is now completely given by

$$\kappa_b = 4\pi \frac{1}{\beta} \frac{1}{\rho_\ell} \int_0^\infty \frac{\wp(a)\, a}{\omega_0^2 - \omega^2 + i2b\omega} da. \tag{2.63}$$

Plugging (2.63) into (2.55), the speed of sound in a bubbly liquid is given by:

$$\frac{1}{c_m^2} = \left[(1-\beta)\rho_\ell + \beta\rho_g\right]\left[(1-\beta)\kappa_\ell + \frac{4\pi}{\rho_\ell} \int_0^\infty \frac{\wp(a)\, a}{\omega_0^2 - \omega^2 + i2b\omega} da\right]. \tag{2.64}$$

For naturally occurring air bubbles in water two simplifications can be made, $\rho_g \ll \rho_\ell$ and $\beta \ll 1$. In these limits, the complex mixture sound speed is given by:

$$\frac{1}{c_m^2} = \frac{1}{c_\ell^2} + 4\pi \int_0^\infty \frac{\wp(a)\, a}{\omega_0^2 - \omega^2 + i2b\omega} da. \tag{2.65}$$

This is the essentially the same result derived by Foldy [16] in 1944 and reported by Commander and Prosperetti [29] in 1989. The only remaining unknown is the damping coefficient, b, which we have neglected detailed discussion of thus far.

As mentioned in Chapter 1, one of the most important advances in the study of bubbly liquids in the second half of the 20th century was Prosperetti's [26, 27] solution for the heat transfer and thermodynamics inside an oscillating gas bubble. This solution manifests itself in two related ways, the first being the frequency dependent polytropic exponent and the second being the frequency dependent thermal damping coefficient. Both are encapsulated in the following expression:

$$\Phi = \frac{3\gamma}{1 - 3(\gamma-1)\, i\chi \left[\sqrt{\frac{i}{\chi}} \coth\left(\sqrt{\frac{i}{\chi}}\right) - 1\right]} \tag{2.66}$$

where γ is the ratio of specific heats of the gas inside the bubble and $\chi = D_g/\omega a^2$ is the thermal diffusion length. Here D_g is the thermal diffusivity of the gas, given by

$$D_g = \frac{(\gamma-1)\, K_T T}{\gamma p_0}, \tag{2.67}$$

where K_T is the gas' thermal conductivity, T is the absolute temperature and p_0 is the bubble equilibrium pressure, defined below. The derivation of the expression for Φ, which can be used to relate the instantaneous radius and internal pressure of oscillating gas bubble in a liquid, is far beyond the scope of the present work although it is important to note that it is both dimensionless and complex.

The polytropic exponent and thermal damping coefficient are, respectively,

$$\eta = \frac{1}{3}\mathrm{Re}\,(\Phi) \tag{2.68}$$

and

$$b_{th} = \frac{p_0}{2\rho_\ell a^2 \omega}\mathrm{Im}\,(\Phi)\,. \tag{2.69}$$

Using the proper polytropic exponent, an accurate expression for the bubble resonance frequency, correcting for the Laplace pressure, is

$$\omega_0^2 = \frac{1}{\rho_\ell a^2}\left(3\eta p_0 - \frac{2\sigma}{a}\right) \tag{2.70}$$

where σ is the surface tension and $p_0 = P_\infty + 2\sigma/a$ is the bubble equilibrium pressure. The remaining damping terms, viscous and radiation damping are

$$b_{vis} = \frac{2\mu}{\rho_\ell a^2} \tag{2.71}$$

and

$$b_{rad} = \frac{\omega^2 a}{2c_\ell} \tag{2.72}$$

where μ is the viscosity of the host liquid. The total bubble damping constant is

$$b = \frac{p_0}{2\rho_\ell a^2 \omega}\mathrm{Im}\,(\Phi) + \frac{2\mu}{\rho_\ell a^2} + \frac{\omega^2 a}{2c_\ell}\,. \tag{2.73}$$

41

The wave number, k_m, of a plane progressive wave in a bubbly liquid is given by

$$k_m^2 = \frac{\omega^2}{c_m^2} = \frac{\omega^2}{c_\ell^2} + 4\pi\omega^2 \int_0^\infty \frac{\wp(a)\,a}{\omega_0^2 - \omega^2 + i2b\omega} da. \tag{2.74}$$

It is straightforward to determine expressions for the phase velocity, c_p and attenuation, α, of the sound wave using the plane wave formulism

$$\exp\left(ik_m x - i\omega t\right) = \exp\left(-\alpha x\right) \exp\left(i\omega \left(\frac{1}{c_p}x - t\right)\right),$$

giving us

$$\alpha = \mathrm{Im}\left(k_m\right) \tag{2.75}$$

and

$$\frac{1}{c_p} = \frac{\mathrm{Re}\left(k_m\right)}{\omega} = Re\left(\frac{1}{c_m}\right). \tag{2.76}$$

Figures 2.13 and 2.14 are plots of the phase speed and attenuation for bubbly liquids of various void fractions and size distributions. A Gaussian bubble size distribution,

$$\wp(a) = C \exp\left(-\frac{(a - a_0)^2}{s_a^2}\right), \tag{2.77}$$

is used in these calculations where s_a is the standard deviation and C is a constant given by Eq. (2.58) as a function of void fraction. For a thorough investigation of the effects of different parameters, the investigative reader is directed to [1].

It is important to note that four distinct regimes are visible in all plots. The first is the low frequency or Wood's equation regime. Here the effects of bubble dynamics are minimized and the sound speed is only weakly dispersive and accurately predicted by Wood's equation, Eq. (1.5). As the driving frequency approaches the bubble resonance frequency
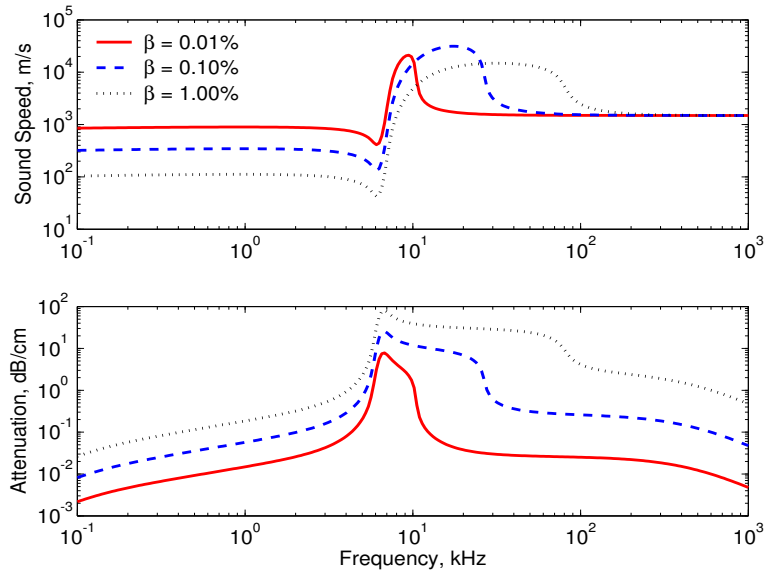
Figure 2.13: Phase speed and attenuation in a bubbly liquid at different void fractions. The mean bubble radius is 500 μm with a 20 μm standard deviation.
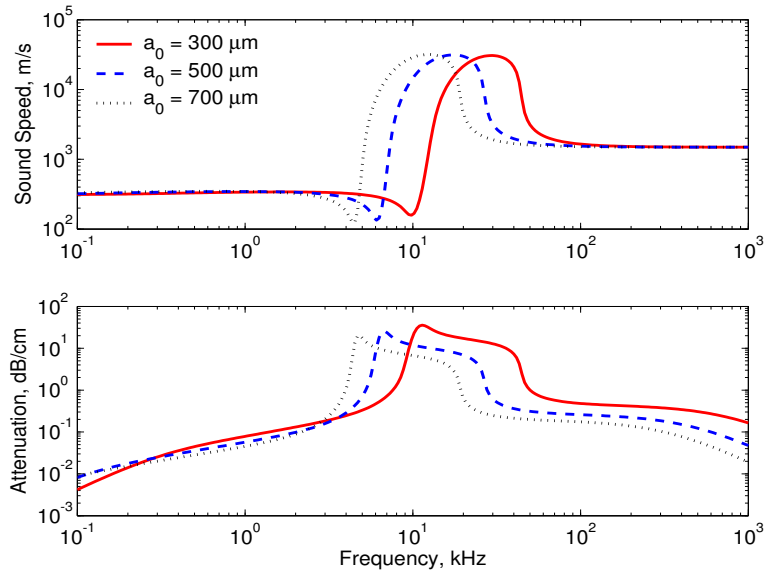
Figure 2.14: Phase speed and attenuation in a bubbly liquid at different mean bubble radii. The void fraction is 0.1% and the standard deviation in bubble radius is 20 μm.

the phase speed becomes strongly dispersive, dropping considerably as the attenuation rises sharply. This is the resonant regime. Just above resonance the phase speed rises quickly and plateaus at a value that is super-sonic relative to the host medium while the attenuation declines steadily. Here the bubble oscillations are out of phase with the driving pressure, making the effective fluid appear very stiff. This is the super-resonant regime. At higher frequencies, the response of the bubbles, like any harmonic oscillator, goes to zero as the system becomes dominated by the inertia of the fluid mass loading the bubbles. At these frequencies, known as the "sonic velocimeter" limit, the bubbles behave essentially as a suspension of rigid spheres in the host liquid and the phase velocity is independent of bubble size or void fraction and equal to that of the host fluid.

2.2.3 Multiple scattering considerations

An important assumption used to derive the expression for the bubble compressibility, Eq. (2.63), in the previous section was that the presence of any individual bubble does not effect the response of any of the other bubbles. That is to say that the sound field scattered from a given bubble is never incident on neighboring bubbles or is at least of much, much lower magnitude than the driving sound field. While this assumption holds for bubbly liquids of low void fraction, it is certainly not applicable at higher void fractions. Just where the transition from low to high void fraction lies is an open question. Commander and Prosperetti [29], in presenting the theory derived here alongside a half century's worth of published data, estimated the transition to lie above 1-2% void fraction.

In 2001, Kargl [58] attempted to account for higher order scattering effects. He reasoned

that each individual bubble interacts not with the host fluid, but with the effective fluid. As such, the terms ρ_ℓ, μ, and c_ℓ in equations (2.70) and (2.73) should be replaced with ρ_m, μ_m, and c_m, respectively. Because the density and viscosity of the host liquid and the effective fluid are the very close to each other for small void fractions, the only term that Kargl suggested changing is b_{rad}, the acoustic radiation damping which is dependent on the sound speed,

$$b_{rad} \to \frac{\omega^2 a}{2c_m}. \tag{2.78}$$

This model predicts that the transition from low to high void fractions (defined as the significant departure between the two models) occurs around 0.1%. Figure 2.15 compares the phase speed and attenuation predicted using Kargl's model to Commander and Prosperetti's for a 1% void fraction population of 500 μm radius bubbles. While the two theories predict similar low frequency responses, they quickly deviate around bubble resonance. Kargl's correction does not predict the sharp dip in sound speed and rise in attenuation of the original theory. The rise is phase velocity is pushed to a higher frequency, where it quickly skyrockets to close to 10^7 m/s, about 3% the speed of light!

While the attenuation predicted by Kargl's correction is in line with published data (indeed, his attenuation predictions very only slightly from those of Commander and Prosperetti), his blistering phase speed predictions are not. Figure 2.16 compares phase speed measurements made using hydrophones and a laser interferometer in a 1% void fraction 1.11 mm radius bubble population made by Cheyne, Stebbings, and Roy [59] with those predicted by Commander and Prosperetti and Kargl. Clearly, the former's "uncorrected"
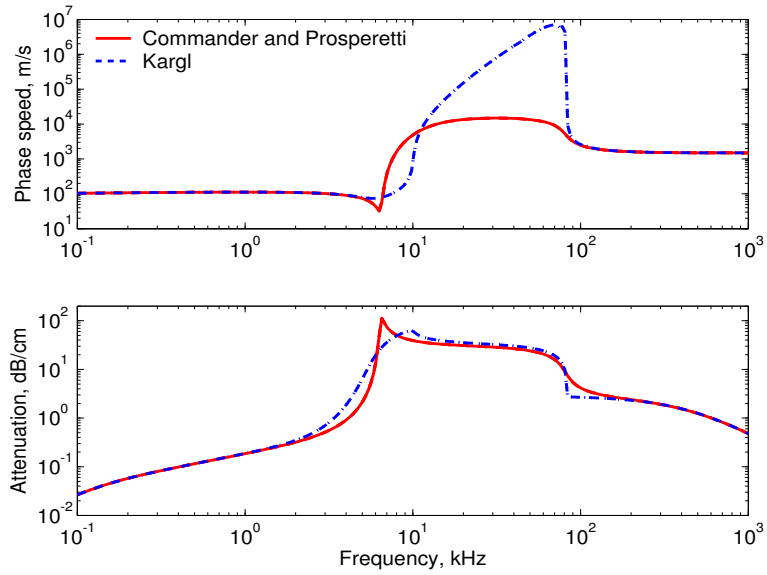
Figure 2.15: Comparison of Kargl's theory to that of Commander and Prosperetti for a 1% void fraction mono-dispersed 500 μm bubble popluation.

formulation fits the measurements best. The proverbial jury is still out on multiple scattering, which remains one of the last remaining hurdles in bubbly liquid theory.
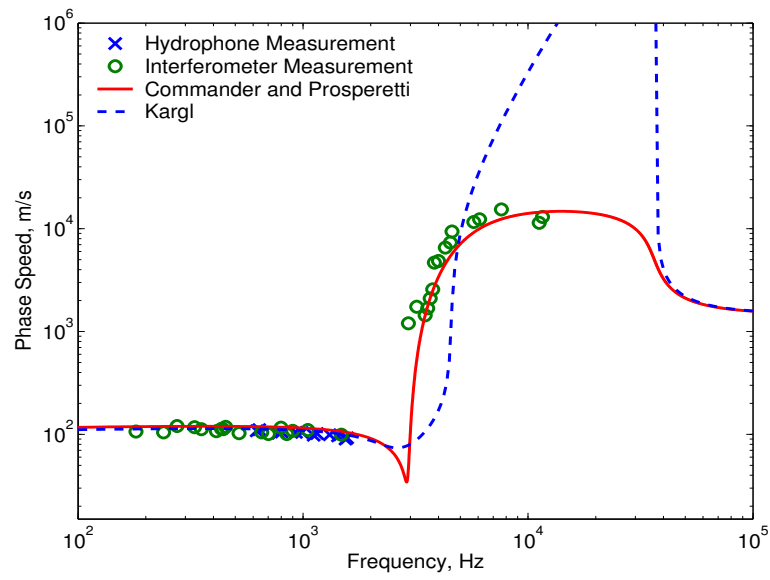
Figure 2.16: Comparison of Cheyne et al.'s phase velocity measurements to the theoretical results of Commander and Prosperetti and Kargl for 1.0% void fraction of mono-disperesed 1.11 mm radius bubbles.

Chapter 3

Experimental Setup and Procedure

The development of the apparatus described here is a continuation of the work of Wilson [1, 31]. Wilson's apparatus, shown in Figure 1.2, was the first impedance tube used to measure bubbly liquids. This Chapter details the theory, design, construction, and verification of a successor impedance tube system. The new impedance tube, shown in Figure 1.3, overcomes a number of limitations with its predecessor, but these improvements come with their own limitations on performance, as will also be shown this Chapter. We will begin with an overview of the theory behind the measurement method.

3.1   The single hydrophone transfer function method

The transfer function method (TFM) was developed in its present form by Chung and Blaser [60] in 1979. The TFM exploits the power of modern spectral analyzers, whose fast Fourier transform routines can calculate the complex transfer function between two

signals in near-real time. This method allows for the calculation of the complex plane wave reflection coefficient in a tube over a fairly broad range of frequency in a matter of seconds. The theory behind the TFM is derived below for the simple case of time-harmonic excitation. Prior to the advent of the TFM, measurements of reflection coefficients were made predominantly by the standing wave ratio (SWR) method (see [37], for instance). The SWR is a bulky and time consuming method which requires the measurement of the pressure field at every point in the tube from its termination back at least half a wavelength at a single frequency.

3.1.1 TFM theory

Recall that Eq. (2.17) gives the pressure anywhere in a tube subject to time-harmonic plane wave excitation as

$$p\left(d,t\right) = P_i\left(e^{-ikd} + \Re e^{ikd}\right)e^{-i\omega t}. \tag{3.1}$$

where $\Re$ is the plane wave reflection coefficient and d is the distance from the tube opening. Now consider the arrangement shown in Figure 3.1 where two hydrophones are located in a tube at distances $d = \ell$ and $d = \ell - s$ from an impedance termination, Z_n. The pressure at each hydrophone is given by

$$p_1\left(t\right) = P_i\left(e^{-ik\ell} + \Re e^{ik\ell}\right)e^{-i\omega t} \tag{3.2}$$

$$p_2\left(t\right) = P_i\left(e^{-ik(\ell-s)} + \Re e^{ik(\ell-s)}\right)e^{-i\omega t}. \tag{3.3}$$

Now divide Eq. (3.3) by (3.2)

$$\frac{p_2}{p_1} = \frac{e^{-ik(\ell-s)} + \Re e^{ik(\ell-s)}}{e^{-ik\ell} + \Re e^{ik\ell}} \tag{3.4}$$
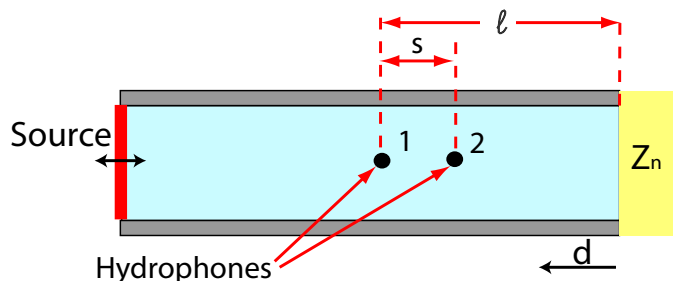
Figure 3.1: Test arraignment and hydrophone locations for the transfer function method.

and note that there is no longer any time dependence. This expression is defined as the transfer function, $H_{12} = p_2/p_1$, between the two hydrophone pressure measurements. With a little algebraic rearrangement, an expression for the plane wave reflection coefficient is obtained:

$$\Re = \frac{H_{12} - e^{iks}}{e^{-iks} - H_{12}} e^{-ik2(\ell)} \tag{3.5}$$

It is important to note that H_{12} is a complex quantity containing both the amplitude ratio and phase difference between the pressures at the two points. The pioneering study by Chung and Blaser derived Eq. (3.5), in a much more rigorous fashion, showing that it holds not only for harmonic but broadband random or swept sine excitation as well, provided only plane waves exist. As such, the transfer function and reflection coefficient in Eq. 3.5 can be functions of frequency, $H_{12}(\omega)$ and $\Re(\omega)$. The beautiful point is that a modern two-channel spectral analyzer can measure $H_{12}(\omega)$ over a broad range of frequency in a

couple of seconds[1,2].

3.1.2 Hydrophone location and spacing considerations

Chung and Blaser also showed that the singularity in the denominator of (3.5), $\exp{(iks)} - H_{12} = 0$, is avoided so long as the hydrophone spacing is such that

$$s \leq \frac{\lambda_{\min}}{2} = \frac{c}{2 f_{\max}} \qquad (3.6)$$

where λ_{min} is the acoustic wavelength of the highest measurement frequency, f_{max}. This condition limits the usable frequency range of the TFM for a given sensor spacing. The ASTM standard [63] concerning acoustic impedance measurements using the TFM recommends using a sensor spacing of no more than 80% of $c/2f_{max}$, while Chu [61] suggests the optimal spacing is 70% of this upper limit. In their rigorous analysis of errors inherent in the TFM, Seybert and Soenarko [62] determined that certain bias errors are minimized when the sensor spacing is small, but recognized that at low frequencies the magnitude of the transfer function approaches unity for small s, reducing the accuracy of the measurements. Gibiat and Laloe [64] state that the optimum spacing is a quarter of a wavelength and recommending a frequency range of a tenth to one-third of a wavelength for a given sensor

---

[1]Spectrum analyzers, like the HP 89410A and HP 39562A used for this work, measure the transfer function as a function of frequency. By definition (see, for instance, [61, 62]),

$$H_{12}(f) = P_2(f)/P_1(f) = G_{p_1 p_2}(f)/G_{p_1 p_1}(f)$$

where $P(f)$ is the Fourier transform of a hydrophone signal. $G_{p_1 p_2}(f)$ is the cross spectral density of the two hydrophone signals, equal to $\frac{1}{2}(P_1(f) * P_2(f))$ and $G_{p_1 p_1}(f)$ is the auto-spectral density of the signal from hydrophone 1.

[2]It is important to note that most spectrum analyzers use a different imaginary variable notation, replacing i with j. As j is commonly defined as $j = -i$, it is often necessary to change the sign of the imaginary part of the data collected from the analyzer.

spacing. Clearly the determination of sensor spacing is as much of an art as a science. In this work a sensor spacing such that

$$\frac{\lambda}{10} \leq s \leq \frac{\lambda}{4} \tag{3.7}$$

was found to work sufficiently well. To increase the frequency range beyond these limits more than one sensor spacing must be used.

Figure 3.2 is a plot of the limits given by Eq. (3.7) as a function of frequency for a sound speed of 1460 m/s, representative of the plane wave phase speed of water in our tube. Based on the nature of this curve, our tube's 1-16 kHz operational frequency range is divided into four separate measurement bands. These bands are 1-2, 2-4, 4-8, and 8-16 kHz with respective hydrophone spacings of 16, 8, 4, and 2 cm, and are also shown on the plot as solid lines.
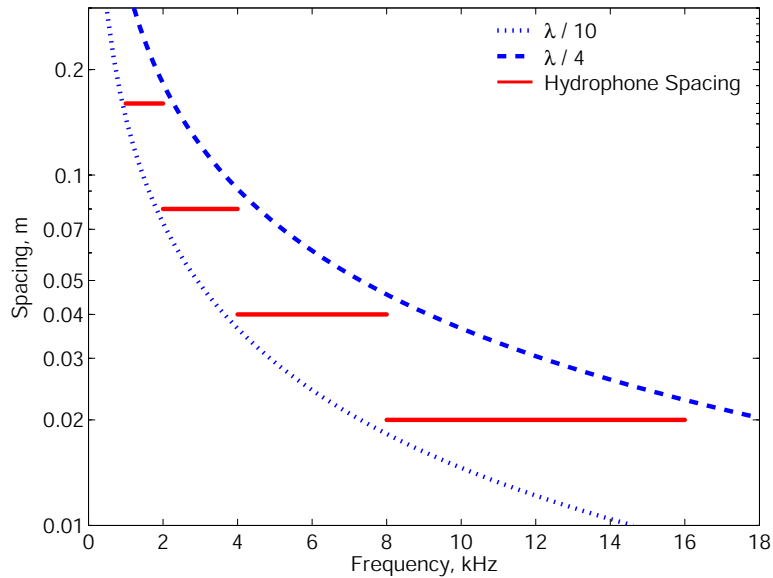
Figure 3.2: Limits on hydrophone spacing as a function of frequency (broken lines) and hydrophone spacing used in this work (solid lines).

The absolute location of the hydrophones must also be chosen. Seybert and Soenarko [62] recommend placing the sensor as close as possible to the measurement plane to minimize bias errors. The ASTM standard [63] suggests placing the closest sensor anywhere from at least one half to two tube diameters away, depending on the nature of the termination, to allow reflections of higher order modes (which do not propagate) to decay. Although we neglected them in the derivation of the plane wave reflection coefficient, higher order modes must exist at a baffled tube opening to completely define the boundary conditions (see Section 2.1.3). It was found that the tube performed best when the closest hydrophone was roughly three tube diameters from the opening.

3.1.3   Transfer function measurement with a single hydrophone

In order to measure the pressure simultaneously at points 1 and 2, two hydrophones must be used. In a perfect world, the signal from the hydrophone at point 1 divided by the signal from its counterpart at point 2 would equal H_{12}, as the two hydrophones would have identical magnitude and phase response. Unfortunately, no two real hydrophones behave this ideally, and a calibration must be performed if two hydrophones are used. For the previous impedance system, Wilson used a two microphone (hydrophone), three calibration (TMTC) method developed in the early 1990's [64]. While extremely accurate, the hydrophones used were very susceptible to shock and vibration and the calibration measurement was susceptible to small changes in temperature (as the speed of sound of the water in the tube is strongly temperature dependent). The hydrophones were also wall-mounted, placing a permanent restriction on the usable frequency range via Eq. (3.6).

Both the need for calibration and the fixed frequency range imposed by using wall-mounted hydrophones can be overcome simply by using a single hydrophone that is scanned along the tube axis. This method, developed for air-filled tubes, was first presented by Chu [61] in 1986. The pressure spectrum measured by the hydrophone at one location is stored and compared, without calibration or correction, with the signal from the same hydrophone moved to the second location. In order to preserve phase information, the hydrophone signals must be referenced to a third signal at each point. The transfer function between the two hydrophones is given by

$$H_{12}\left(f\right) = \frac{G_{p_1 s}}{G_{p_1 p_1}} \frac{G_{s p_2}}{G_{ss}} = H_{1s}\left(f\right) H_{s2}\left(f\right) \tag{3.8}$$

where the subscript s refers to the reference signal. It is convenient and practical to use the signal driving the sound source (before it is amplified, of course) as the reference, as it is generated at the spectrum analyzer and has a very flat frequency spectrum.

As mentioned before, this method works over a much broader frequency range than most two sensor methods. In practice the low end of the usable frequency range is usually determined either by tube length (at least half a wavelength in length is recommended) or by the efficiency of the driving source (most piezoelectric crystals have very high electrical impedance below their resonance frequency). In this work, the source was the limiting factor as we found it difficult to sufficiently excite the tube below 1 kHz. The upper bound on frequency is usually determined by the cutoff frequency for the first higher-order mode. Although more than one mode can exist in a fluid-filled tube at all frequencies (see next section), the first cutoff frequency for a sound-hard tube of the same dimensions is generally

54

a good indicator of the upper usable limit. For our water-filled tube, the upper frequency limit was around 14 kHz.

3.2 Corrections for elastic waveguide effects

In Section 2.1 it was assumed that the walls of the impedance tube were sufficiently rigid that the radial acoustic velocity is zero at the tube wall. This assumption works remarkably well for air-filled tubes, as relative to air most all solids appear rigid. When the fill fluid is water, or another liquid, the walls can no longer be assumed rigid as the bulk modulus and density of the liquid and the wall enclosing it are often of similar magnitude. The tube walls must be treated as elastic solids, resulting in a number of effects that must be taken into consideration.

While a number of approximate solutions to wave propagation in fluid-filled elastic tubes exist (see, for instance, [17, 65, 66, 67]), they are generally only valid under certain limits, such as tubes with very thin walls or for very low acoustic frequencies. Del Grosso [68, 69], in the late 1960's, used the complete longitudinal and shear wave equations to obtain an exact solution for acoustic wave propagation in an inviscid fluid contained in an elastic tube of arbitrary thickness and material. His results were rediscovered and simplified by Lafleur and Shields [70] in 1994. More recently, in 2000, Elvira-Segura [71], using Del Grosso's formulation, added the dissipative effects of fluid viscosity to the solution.

Accounting for the elasticity reveals three significant departures from rigid tube theory. First, more than one mode can propagate at all frequencies. Recall that in a rigid tube, only

one mode can propagate at frequencies below the first cutoff frequency. In an elastic tube, two modes exist below this cutoff frequency: the lowest order, where most energy travels in the liquid, and the next highest order, where most energy travels in the tube walls. The second effect is that all modes, including the lowest order, have a radial velocity component and a radially dependent pressure profile. In the rigid waveguide, the lowest order mode was a plane wave, with a uniform pressure profile and no radial velocity component. And finally, all modes, including the lowest order, have dispersive (frequency-dependent) phase speeds. The plane wave mode in a rigid tube has a constant speed of propagation, equal to the intrinsic speed of sound of the fluid.

As impedance tube theory and the TFM both require pure plane wave propagation, the effects caused by an elastic waveguide could render the technique useless. However, if careful consideration is given to the elastic solution, these effects can be minimized to a negligible level. Wilson [1], designing the predecessor of the tube described here, optimized the tube parameters in Lafleur and Shield's solution to minimize the departure of the lowest order mode's radial profile and speed of propagation from the ideal, plane-wave case. He showed the optimum design is to have the tube's moduli of elasticity and density be as large as possible (stainless steel, he found, is preferable to a hardened aluminum) and to have the inner radius of the tube equal to the wall thickness.

The inner diameter is determined by the required upper bound on frequency. As is the case with rigid tubes, it is difficult to selectively propagate energy in one tube mode and not another above the first cutoff frequency. This is the frequency where half an acoustic

56

wavelength is equal to the inner diameter of the tube. Wilson selected an inner diameter of about 5 cm. With water in the tube, this corresponds to a cutoff frequency around 14 kHz. In practice, the tube worked sufficiently well up to at least 16 kHz. In a water filled stainless steel tube with a 5 cm inner diameter and 15 cm outer diameter, the lowest order mode has less than 0.5% dispersion in phase speed and a radial pressure profile that changes at most 5% from the tube's central axis to its wall over the 0 to 16 kHz frequency range. Wilson showed that, for use in the TFM, the lowest order mode can be modelled as a plane wave, travelling at a constant phase speed representative of that predicted by the elastic waveguide solution over the frequency range. The selective coupling of energy into the lowest order mode only is discussed in Section 3.3.1.

The elastic waveguide solutions discussed above all assumed that the outer diameter of the tube was in contact with air, or another gas, and could be modelled having zero tangential and normal stress there. As the impedance tube in this work is to be submerged, it is necessary to consider any effects that liquid loading outside the tube may have. Holmes [72] has shown, in a rigorous mathematical analysis, that any such effect is negligible for water loading on a stainless steel tube of the dimensions used in this work. Dunlop [32] reached the same conclusion using a simplified elastic tube model for a tube of somewhat different dimensions.

To confirm that external fluid loading is negligible, the phase speed of the lowest order mode was measured at a number of different frequencies with the tube submerged in water. The measurements, showing excellent agreement with La Fleur and Shield's prediction, are

shown in Figure 3.3. Measurements were made in both the time and frequency domains. Time domain measurements were made using three cycle pulses at different frequencies. For each frequency, the pulse recorded by a hydrophone at one position is compared to that with the hydrophone moved a prescribed distance. The phase speed is given by this distance divided by the time lag between the two signals, determined using the cross correlation

$$\Delta t = \max \left(\int_{\tau_1}^{\tau_2} p_1 \left(\tau + t \right) p_2 \left(\tau \right) d\tau, t \right).$$ (3.9)

The frequency domain measurements were made by measuring the distance between consecutive nulls in the pressure spectrum at a given frequency. This distance corresponds to one half an acoustic wavelength which is a direct function of the sound speed. A number of frequency points can be measured at once by looking at a single frequency spectrum a known distance from a *pressure release* surface, such as a water-air interface. As will be shown in a Section 3.5.1, the pressure anywhere inside a tube terminated with such a surface is:

$$p \left(d \right) \propto \sin \left(kd \right)$$ (3.10)

where d is the distance from the surface. The pressure tends to zero whenever kd is an interger multiple of π. As $k = 2\pi f/c$, the sound speed, c_n, at f_n, the nth frequency null, is given by

$$c_n = f_n \frac{2d}{n}.$$ (3.11)

The error bars on the plot represent uncertainty in the measured time, frequency and length parameters.

The measurements and theoretical solution shown in Figure 3.3 also give a good indication as to just how little dispersion there is in tube. The magnitude of the phase speed is only slightly more than 2% lower than the intrinsic speed of sound of water and the
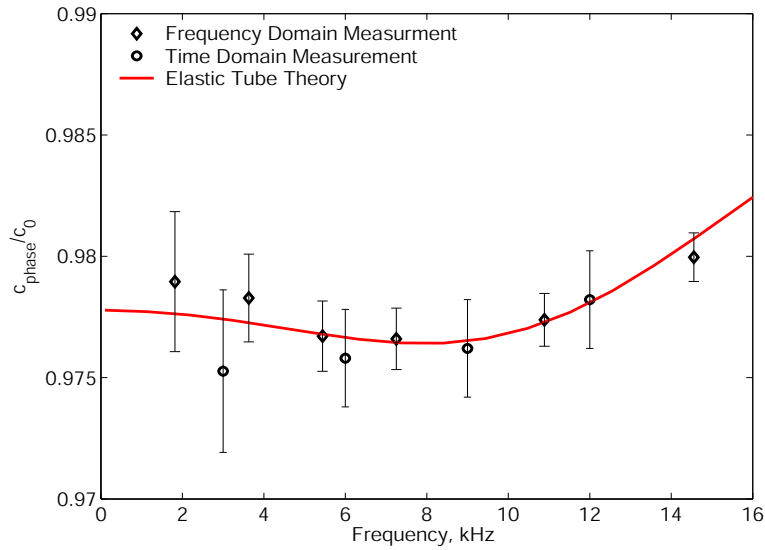
Figure 3.3: Measured waveguide phase speed, c_{phase}, in our submersed, water-filled impedance tube is compared to the theoretical prediction for the non-submersed waveguide. The values are normalized by c_0, the intrinsic sound speed of water. Error bars represent uncertainty in the measured length, time, and frequency parameters.

3.3 Design and construction of the impedance tube system

A general overview of the mechanical impedance tube system is shown in Figure 3.4. The impedance tube is solid 304 stainless steel with an overall length, excluding the baffle, of 68.6 cm. The inner radius is precision machined to 2.601 cm while the outer surface, about 5.08 cm in radius, has a rough finish. A 1.27 cm thick stainless steel baffle about 61 cm in diameter, is bolted to a flange at one end of the impedance tube. The mounting bolts

are counter-sunk into the baffle to maintain a flat profile at the tube opening. A sound source, described in detail in the next section, is mounted to the other end of the tube. As mentioned in Section 3.1.3, a single hydrophone is scanned along the tube axis. This hydrophone is mounted in a sheath that is aligned with an acoustically transparent centering start and positioned along the tube axis using a stepper motor and timing belt assembly described in Section 3.3.2. The system electronics and instrumentation are discussed in Section 3.3.4.
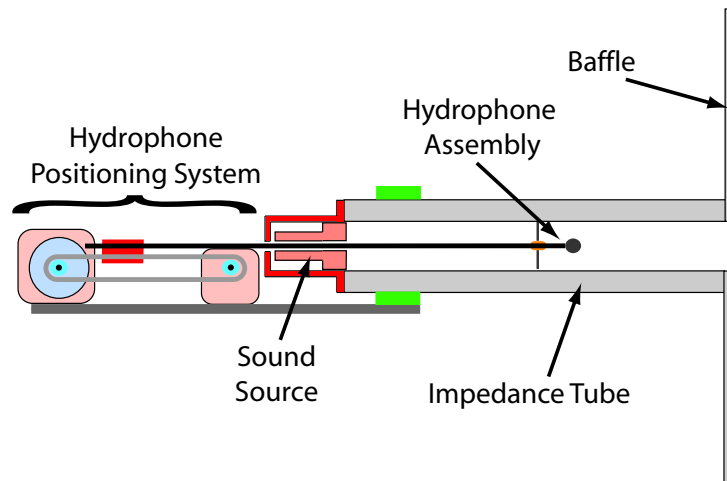
Figure 3.4: General overview of the mechanical components of the baffled, submersible impedance tube system.

3.3.1 The sound source

The sound source is used to generate the acoustic waves in the tube. The sound source must meet two objectives. One is that it must couple sufficient energy into the lowest order, "plane-wave like," tube mode while minimizing coupling into the next highest mode. The other is that, in order for a hydrophone to be scanned along the tube axis, our design

must also allow for the hydrophone sheath to pass through it. We chose a modified *Tonpilz* (German for "singing mushroom") style transducer, shown in Figure 3.5 and Figure 3.6. Dimensioned technical drawings are shown in Appendix D.
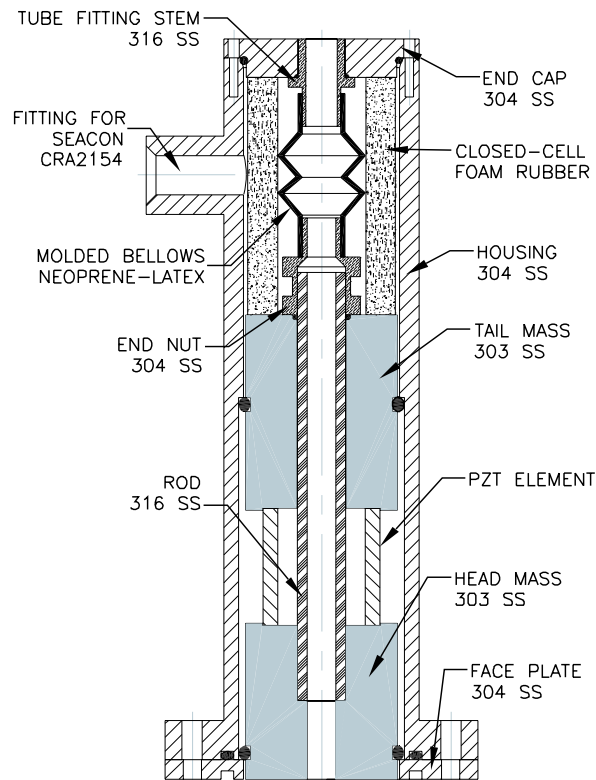
Figure 3.5: Cutaway drawing of the source transducer with pass-through hole. Electrical wires are not shown.

The standard Tonpilz design consists of a piezoelectric element, in our case lead zirconate-lead titanate (PZT), sandwiched between two masses, a head mass (the face of which radiates sound into the tube) and a tail mass. The "sandwich" is held together with a connecting bolt that threads into the head mass and is tightened against the tail mass with an end nut. The connecting bolt compresses the ceramic to ensure that it does not encounter a tensile
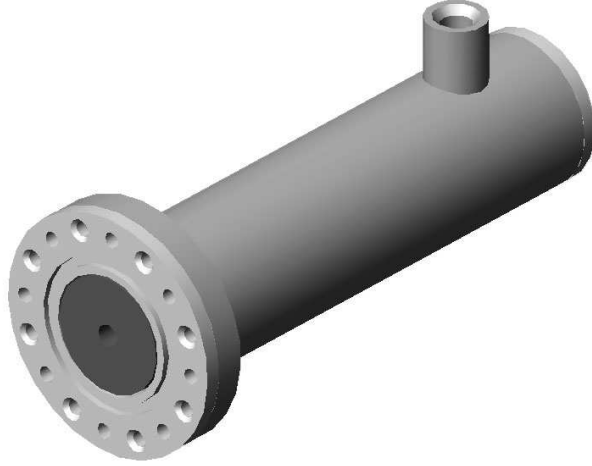
Figure 3.6: Outside view of the source transducer

strain in operation (ceramics have very low tensile strengths).

Design choices were made so that the source will couple very efficiently into the lowest order tube mode (which has a relatively flat radial profile and very little energy travelling in the tube walls) and not into the next highest mode (which has a significant radial profile and most of its energy travelling in the tube walls). Our modified design encloses the active elements inside a stainless steel housing and has a $^3/_8$ inch diameter hole along the axis of the masses and connecting rod. The head and tail masses are suspended in the housing with rubber o-rings. These serve to decouple the linear motion (as well as any radial motion) of the masses from the housing and therefore the tube walls. The face of the head mass, which is in contact with the fluid in the tube, is machined very flat so as not to impart any radial motion to the fluid.

Ideally, no acoustic energy should radiate out from the back of the source and no fluid should enter into its inner workings. The tail mass is isolated from the housing's end cap

with a flexible neoprene-rubber bellows. The bellows are supported by a thick closed-cell foam-rubber sheath. The foam rubber keeps the bellows from over-expanding from fluid pressure on the inside (if the apparatus is operated at depth). The foam also serves to decouple the end cap from the motion of the tail mass should the compartment flood with water.

The signal cable is attached to the transducer via a waterproof connector. This connector, a SEACON Model CRA 2154, has a custom coaxial connection on the outer, or "wet" side and two wire leads on the inside ("dry") of the transducer housing. These leads are soldered onto the inside and outside of the PZT crystal. The connector screws into the fitting jutting out from the housing, labelled in Figure 3.5.

Ideally, the source transducer would have a flat frequency response across the range of use. A Tonpilz, however, is a strongly resonant device. So long as the acoustic wavelength is smaller than the length of the piezoelectric element, the Tonpilz can be modelled as two masses coupled by a single spring (the PZT element) [73]. Such a system has a steep rise in response with frequency below resonance, a very strong response at resonance, and a flat, slightly less strong, response at frequencies above resonance. The resonant frequency of a Tonpilz is given by

$$f_0 = \frac{1}{2\pi}\sqrt{\frac{K}{M}} \tag{3.12}$$

where K is the effective stiffness of the PZT element,

$$K = \frac{AE_{11}}{L}, \tag{3.13}$$

and M is the effective mass,

$$M = \frac{m_H m_T}{m_H + m_T}. \tag{3.14}$$

Here A, E_{11}, and L are the cross-sectional area, principle modulus of elasticity, and length of the PZT element and the mass of the head and tail masses are given by m_H and m_T, respectively. Typical values of E_{11} for PZT are between 60 and 120 GPa.

In order to keep the frequency as flat as possible over the broadest range of frequency, the source was designed to resonate at as low a frequency as reasonably possible. A hollow cylindrical PZT element, 1.5 inches long with a 1.5 inch outer diameter and 0.188 inch thickness was used. The element has a resonance frequency around 28 kHz when driven in the longitudinal mode. This element was selected because it was largest cylindrical element available in our laboratory. A large element is desirable because the maximum electric field (and therefore drive level) that can be applied to a piezoelectric crystal is proportional to its volume. A longer element would have allowed for a lower effective stiffness and reduced the overall resonant frequency, but would have made the overall length of the source too long to be practical.

The volume occupied by the masses was dictated by the allowable size of the source. Stainless steel was selected for the masses to minimize the formation of a galvanic cell when in contact with sea water (the tube is also stainless steel). The only design parameter open to choice was the relative size of the two masses. For a fixed total mass, $(m_H + m_T)$, the largest effective mass, M, and therefore the lowest resonant frequency, is achieved when the two masses are equal, $m_H = m_T$. The masses were designed such that each had roughly

the same mass.

The source, as originally built, resonated around 4 kHz, somewhat lower than predicted by Eq. (3.12), even with the lowest value E_{11} in the range. This was not viewed as a problem, as the design objective was a low resonant frequency. However, it was necessary to coat the entire PZT element with an epoxy resin to waterproof, and thereby electrically isolate, it as problems with electrical shorting were encountered with even a little bit of sea water flooding into the source housing (we speculate one of the original o-rings was poorly fitted and responsible for the breach). The epoxy coating significantly raised the cross-sectional area and effective stiffness of the system, raising the resonant frequency to around 7 kHz, slightly higher than desirable. Figure 3.7 shows the measured acceleration profile of the head mass, measured with a shear accelerometer mounted on the head mass with the entire source assembly submerged in water. The sub-resonance, resonant, and super-resonant regimes are clearly visible.

3.3.2 Hydrophone positioning system

In order to scan the hydrophone along the tube axis, as required by the single sensor TFM, it had to be mounted in a relatively rigid sheath. A Brüel and Kjær model 8103 miniature hydrophone was used. These hydrophones have an exceptionally flat response across the 1 to 16 kHz frequency range, are relatively small in size (9.5 mm in diameter by 50 mm in length) and have a well defined (within ± 0.3 mm) acoustic center. The hydrophone is mounted in a sheath as shown in Figure 3.8. The sheath has two sections. The first is a short, ∼10 cm long, hollow Teflon rod whose outer and inner diameters are about
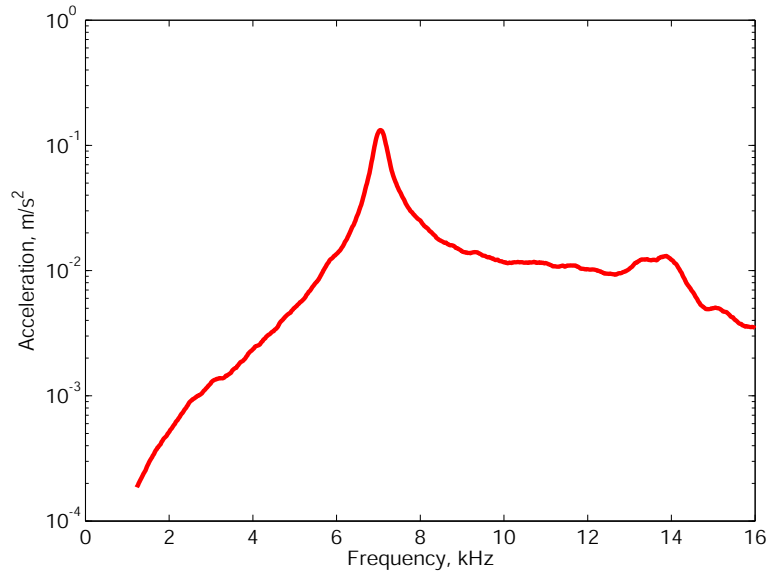
Figure 3.7: Typical acceleration profile of the source transducer head mass, submerged in water. There is a clear mechanical resonance at 7 kHz.

9mm and 6mm. Teflon was chosen because it is easier to machine, more closely impedance matched to water than steel, and, when machined thin, is transparent enough to spot any air bubbles trapped inside it. The inner diameter is bored out to 7mm on one end to accept the hydrophone. A long, hollow stainless steel shaft is press fit into the other end of the Teflon piece. This shaft runs the length of the impedance tube, through the sound source, and is fixed to a positioning track, to be described below, behind the source. The outer diameter of the shaft is $1/4$ inch, which allows for ample clearance between the shaft and the $3/8$ inch bore through the source. The stainless steel sheath has a 0.035 inch wall thickness. The far end of the sheath is open to allow for easy flooding before use.

The hydrophone sheath is centered in the impedance tube with a simple centering star device, also shown in Figure 3.8. The centering star consists of a small broken ring made of
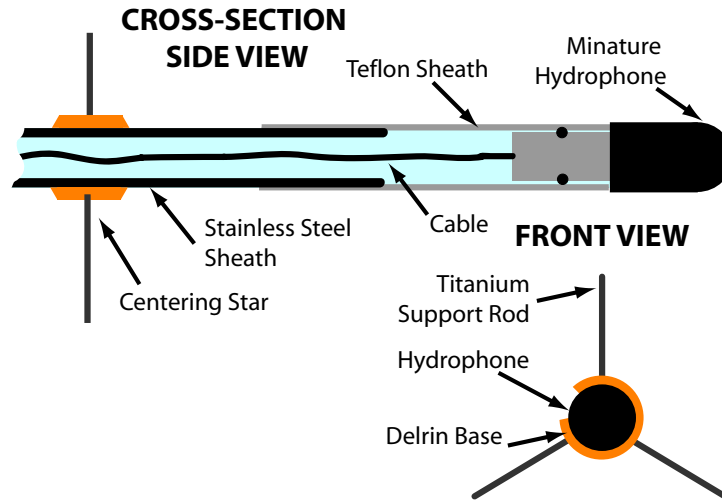
Figure 3.8: Illustration of the hydrophone sheath and centering star.

Delrin that can be snapped on and off the stainless steel portion of the sheath. The ring fits tightly on the shaft, avoiding any unwanted slipping. Three $1/16$ inch diameter titanium rods are press fit into the base, making $120\,^{\circ}$ angles with each other. Titanium was used simply because our supplier did not have any stainless stock on hand. The lengths of the rods are such that the entire star-sheath assembly forms a clearance fit with the inner diameter of the impedance tube. This keeps the hydrophone centered in the tube while allowing it to move unopposed. The entire centering star device is kept as small as possible to avoid interfering with the acoustic field.

As mentioned above, the hydrophone is moved by a positioning system mounted behind the source[3]. The entire positioning system is illustrated in Figure 3.9. The hydrophone sheath is mounted on a Kevlar-reinforced nylon timing belt. The timing belt is held taught

---

[3]Although I wish I could claim to have designed the entire apparatus myself, I owe the design and construction of the positioning system and stepper motor housing to Jason Holmes, who helped work on this project from the fall of 2003 through the summer of 2004.

between two toothed pulleys on $\frac{1}{4}$ inch diameter stainless steel shafts. One shaft is free to rotate, supported on both ends by bearings set in thick acrylic blocks which act as a shaft supports. The other shaft is driven on one end by a stepper motor, enclosed in a waterproof housing (described below) and on the other end is supported in the same manner as the freely rotating shaft. The pulley on the drive shaft was cross-drilled and fixed against free rotation with an expansion pin. The shaft supports, as well as the motor housing support, are attached to two lengths of extruded aluminum which are mounted to the tube using a standard plastic and stainless steel 4 inch pipe support. The aluminum supports are also attached to a frame which surrounds the entire impedance tube apparatus, keeping the system in place once aligned.
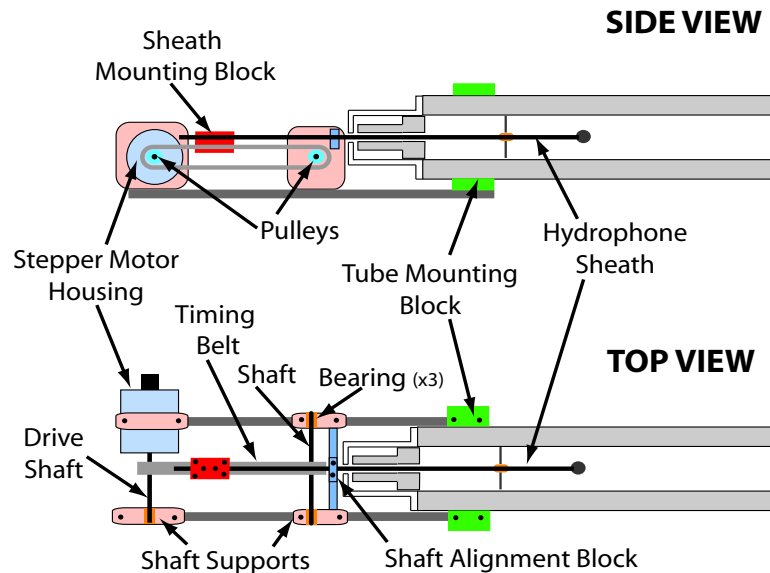
Figure 3.9: Illustration of the hydrophone sheath positioning system.

The stepper motor housing, shown in Figure 3.10, has a relatively simple design. The stepper motor, an Intelligent Motion Systems M-2222-3.0ES-XXX 200 step motor, is bolted

to a large Delrin mounting block. The mounting block has a bore through it slightly oversized to the shaft diameter, helping to keep the motor's drive shaft aligned. On the wet side of the mounting block, a waterproof rotary shaft seal (APM Hex Seal N9030x1/4) seals against the drive shaft and keeps water from entering the housing. The mounting block is held in place by a PVC pipe cap threaded into a section of 4 inch PVC pipe. Another PVC pipe cap is threaded into the other end of the pipe section, holding in place another Delrin block. Compressed o-rings seal both blocks against the pipe. A waterproof connector (SEACON AWM8XSBC) is mounted through the second block. This connector has 8 leads, although only 4 are required for proper motor operation. The other leads were reserved for the possibility of adding a rotation encoder to the stepper motor (to record position) or a temperature sensor. The stepper motor housing was pressure tested, in water, to roughly 300 kPa without failure.
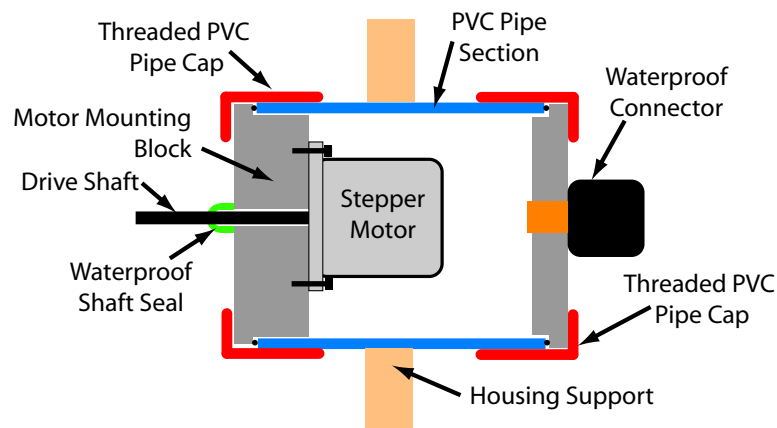
Figure 3.10: Illustration of the stepper motor housing assembly.
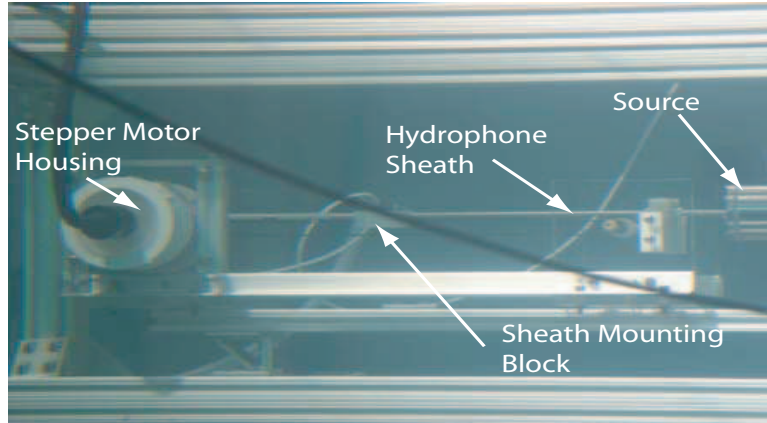
Figure 3.11: Photograph of the positioning system. Principle components are labelled.

3.3.3 Acoustically transparent window

An acoustically transparent 0.8 mm thick high-density polyethylene (HDPE) window can be attached to the tube opening. This window provides a physical barrier between the water inside the tube and the measurement plane. This is very important when measuring bubbly liquids, as it imperative that no bubbles enter the tube. A number of other windows were tested before deciding on the HDPE sheet: a 1 mm thick aluminum sheet, a 1.5 mm thick silicone rubber sheet, and a custom-cast BF Goodrich rho-c rubber[4] insert. The windows were evaluated by comparing the measured complex transfer function, H_{sh} between the signal from a hydrophone inside the tube and the source both with and without the windows in place. Performance was based on how much the windowed transfer function deviated from the windowless measurement. Ranked from best, with the least deviation, to worst the windows performed as follows: silicon rubber, HDPE, aluminum, and rho-c

---

[4]Rho-c rubber is specially formulated two-part compound that, once cured, is impedance matched to sea water. The shelf-life rho-c material used in the casting had expired in 1997 which, although it was kept frozen, could account for its poor performance against the other window materials.

rubber. Although the silicone rubber sheet performed best, it was too flimsy to adequately seal the tube opening against bubbles without permanently bonding it to the baffle. The results from the HDPE test are shown in Figure 3.12. There is almost no deviation between the measurements made with and without the window in place, save for a slight departure near 10 kHz. The window is held in place with three small 6-32 machine screws.
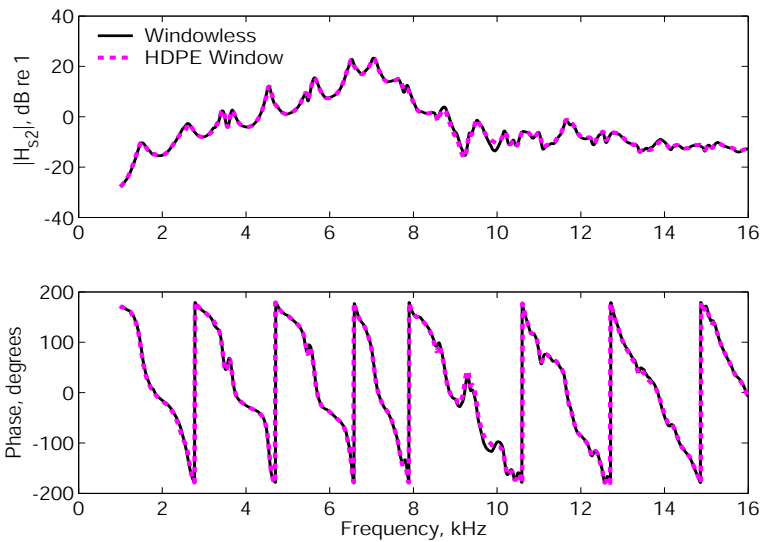
Figure 3.12: Magnitude and phase of the transfer function between the hydrophone and the source measured both with and without the HDPE window in place.

3.3.4 System instrumentation and control

Figure 3.13 is an illustration of the principal components of the complete experimental apparatus. The electronic instrumentation can be divided into three main areas: hydrophone signal conditioning and processing, sound generation, and positioning system control. The primary component is the vector signal analyzer (VSA), which performs the transfer func-

tion measurements and creates the source excitation signal.
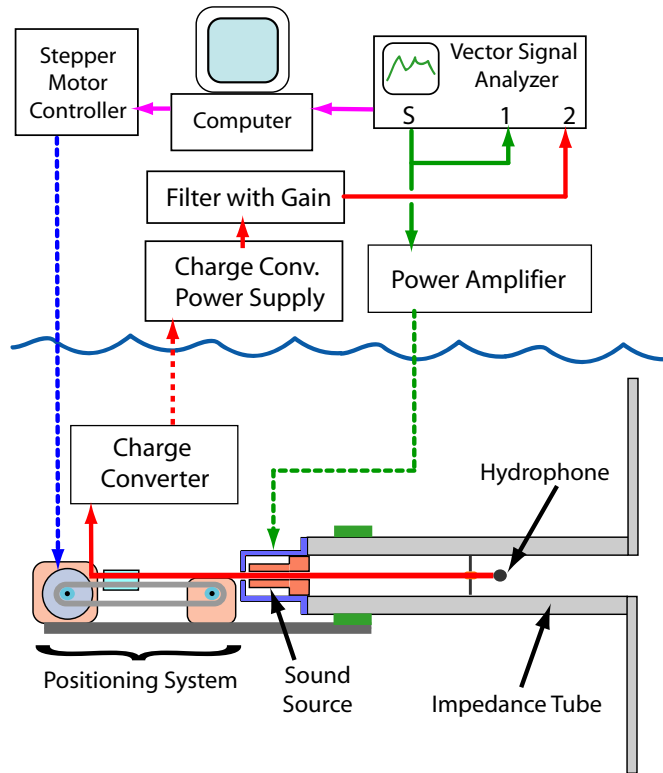
Figure 3.13: Schematic of the experimental apparatus and accompanying instrumentation. 30-meter SEACON cables are shown as dotted lines.

We will begin by discussing the hydrophone signal conditioning. The hydrophone, described in Section 3.3.2, is connected to an Endevco 2771B-1 remote charge converter, providing 1 mV per pC of electric charge produced by the hydrophone. For the B & K 8103 hydrophone used, this corresponds to 96 mV/kPa. The charge converter is enclosed in a waterproof housing, shown in Figure 3.14, constructed out of a thick Delrin block (which can be bolted to the extruded aluminum frame). The double-shielded coaxial hydrophone cable enters the housing through a waterproof cord-grid fitting (Hummel CD09NR-BR, rated to 90 m of water) and connects to the charge converter. The signal is carried from

the charge converter to a waterproof coaxial connector (SEACON CRA2154) via a short length of BNC cable. A custom 30 m length of neoprene coated BNC cable carries the signal from the charge converter housing to a power supply box, located on dry land. The power supply box provides the 18-36 V DC bias required by the charge converter. The hydrophone signal, which is purely AC, is extracted in the power supply box and then band pass filtered with a Krohn-Hite 3940 digital filter to remove both high and low frequency noise. For our measurements, made between 1 and 16 kHz, the low and high filter cutoff frequencies were set at 500 Hz and 20 kHz, respectively. The filter has an optional 20 dB input and/or output gain setting. The 20 dB output gain was sometimes used in transfer function measurements to improve the signal strength. After filtering and amplification, the signal is processed by a two channel VSA. Both an HP 89410A or an HP 3562A VSA were used at different stages of this work.
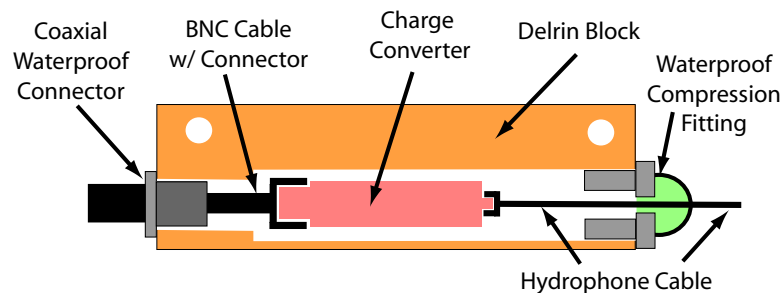
Figure 3.14: Illustration of the charge converter housing.

The VSA is also used to generate the signal used to drive the sound source. In this work, pseudo-random noise was most often used as the driving signal. The signal is amplified by a wideband power amplifier, either a Crown CE-1000 or a Krohn-Hite 7500. A second 30 m neoprene-coated coaxial cable, identical to the one used for the hydrophone signal, carries

the driving signal to the sound source[5].

As mentioned previously, the hydrophone is translated along the tube axis with a stepper motor enclosed in a waterproof housing. The stepper motor is controlled by a Phytron micro-stepping controller (Model GCD 93-70-W-RS232) which is in turn controlled by a computer via a RS-232 connection. The controller is capable of moving our 200 step motor in $1/8$ step increments, a resolution of less than 7/100 of a degree. However there is too much play in pulleys and timing belt driven by the motor for the system to be sensitive to such a small displacement. For the pulley and belt sizes used in this work, the hydrophone was moved 1 cm linearly about every 315 motor $1/8$ steps. The exact calibration was recalculated before each experiment. We found the positioning system accurate to ± 0.12 mm over 35 cm of travel, repeatable to ± 0.05mm. The ± 0.12 mm accuracy corresponds to less than $\pm 0.15\%$ of the shortest wavelength in the tube, sufficient accuracy for the TFM (see Section 3.6).

3.4 Measurement preparation and procedure

Thomas Hobbes would have certainly remarked that the preparation required by our system before making measurements is nasty, brutish, and *long*. Indeed, the preparation procedure described in this section is very time-consuming and detailed, but thus is science. The

---

[5]It should be noted that an expensive coaxial cable is not necessary for this application. A pair of heavy gauge water-blocked wires (similar to those run to the stepper motor, see below) would have been sufficient (and much cheaper). We had, however, contemplated using a measurement of the electrical impedance of the source to estimate the acoustic impedance at the source head (which is in turn a function of the acoustic impedance at the tube opening). This method would have required the signal integrity provided by a coaxial cable. Although the idea was eventually dismissed as being too difficult to model and not sufficiently sensitive to acoustic impedance, the source was (over) designed to accommodate the coaxial cable.

upside is that, as will be shown here, actually making measurements (once the system is properly prepared) is relatively quick and painless. Suggestions for improvement, and there is considerable room for improvement, will be given in a later Chapter.

3.4.1   Preparing the impedance tube for measurements

While the TFM and our computer-controlled positioning system allow for very fast and easy reflection coefficient measurements, as will be discussed later in this Section, preparing the apparatus for measurements is not. Our chief nemesis is, almost ironically, the very beast we set out to study – air bubbles. As explained in Section 2.2, bubbles are very responsive to acoustic waves, and even the most minuscule air bubble trapped anywhere inside the tube, source, or hydrophone sheath completely squashes any chance of an accurate measurement made in its presence. *Extreme* care must be taken to remove any and all air bubbles trapped in the apparatus when preparing it for measurements. The tube alignment, preparation and submersion procedure is as follows.

In order to align the positioning system, the source must be perfectly centered on the tube. An alignment tool was designed for this purpose. The alignment tool is a stepped cylinder, with the largest diameter a clearance fit to the inside of the tube and the other a clearance fit to the hole through the source head mass. The alignment procedure is illustrated in Figure 3.15. First, (1), the alignment tool is inserted into the source until the diameter step is flush with the face of the head mass. Next, (2), the source is bolted to the tube. The alignment tool keeps the source centered on the tube. Last, (3), the alignment tool is pushed out through the tube opening with a rod inserted through the back of the

source.
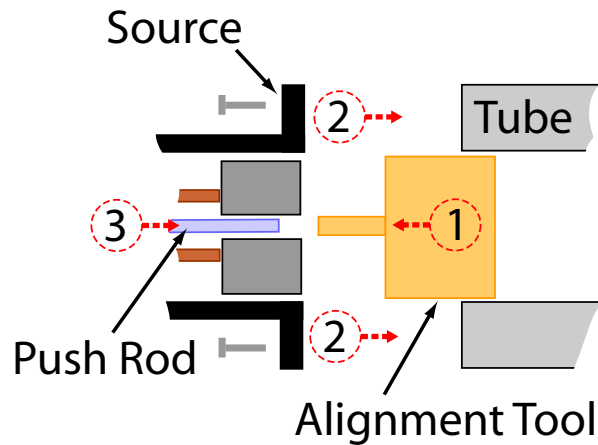
Figure 3.15: Source alignment procedure.

Once the source is centered on the tube, it is used to help align the positioning system. Alignment of the positioning system is crucial to ensure that the hydrophone travels strictly along the tube axis and that the hydrophone sheath does not come in contact with the vibrating source. This procedure is illustrated in Figure 3.16. The hydrophone sheath, or a rod of the same outer diameter, is run through the source / tube assembly (1). The centering star is snapped on the sheath at the tube opening and set back into the tube a couple centimeters (2). The sheath is then mounted on the timing belt, as close to the drive shaft pulley as possible (3). The entire positioning system assembly, which pivots where it is attached to the impedance tube, is then adjusted up and down (and side to side) at the far end until the hydrophone sheath is centered on the opening of the sound source (4). The system is then fixed in place by fastening a mounting bracket, located on the underside of the assembly, to a cross member on the extruded aluminum frame that encases the entire

apparatus (5).
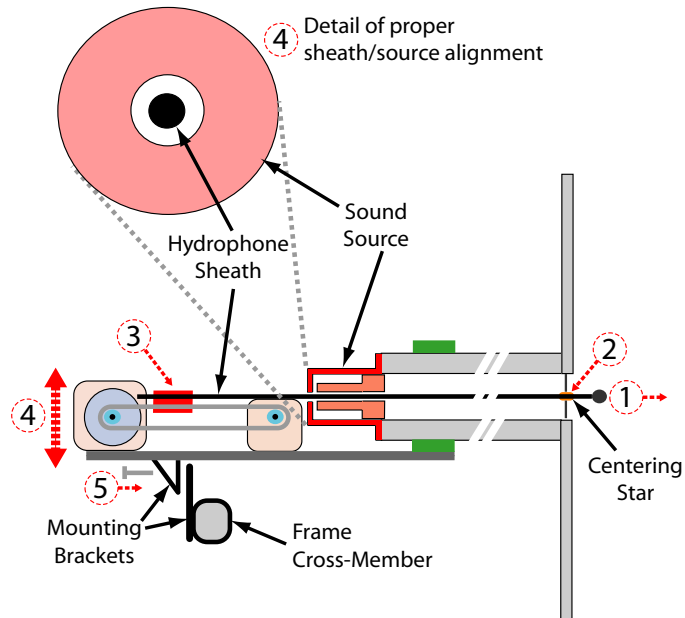
Figure 3.16: Positioning system alignment procedure.

Once the positioning system is aligned and fixed in place, the centering star, hydrophone sheath, and source must be removed to be reattached underwater. Before the tube can be submersed in water, all SEACON connectors are fastened. The coaxial connectors on the source and charge converter housing must be dry-mated, while the steeper motor cable can be connected underwater. Care must be taken not to lose the o-rings that sit in the coaxial connecters. The inside of the tube, baffle face, source face, and hydrophone sheath may also be coated with a hydrophilic wetting agent. Simple Green® detergent and Rain-X® Anti-Fog glass treatment were both found to work well. Wetting makes the surfaces more attractive to water and less attractive to bubbles, making the removal of air bubbles somewhat easier.

The entire assembly, with the source separate from the rest, is then lowered under water, suspended just below the surface. Ideally, the tube assembly should be allowed to reach thermal equilibrium with the water it is submersed in. This reduces problems with air bubbles forming by thermally-driven gas diffusion out of the water. Once submerged, the system is ready for the painstaking underwater de-bubbling and assembly.

First, any bubbles visible on the tube walls are removed with a squeegee. Next, keeping it completely submersed, the source is shaken violently to remove any air trapped inside, especially in the bellows section. A small blunt rod can also be run up and down the length of the source to remove any trapped air. Any air caught in the o-ring groove or on the o-ring must also be removed. Once all the air is removed, the source is aligned and mounted to the tube in the same manner described earlier. The alignment tool has a number of holes drilled through it to allow for water flow. We found that pushing the alignment tube as slowly as possible with the push rod reduces the number of bubbles formed inside the tube during this process. The tube should be re-checked for bubbles at this point, and any bubbles must be removed with the squeegee. We found that a hand-held vanity mirror and a waterproof flashlight worked well for looking inside the tube.

Once the source is attached, the hydrophone sheath must be flooded. The hydrophone sheath is easily flooded by removing the hydrophone and running its cable back and forth through the sheath. Air bubbles trapped inside tend to stick to the hydrophobic hydrophone cable and are dragged out with it as it is passed through the sheath. Bubbles do tend to get caught where the sheath diameter increases at the stainless steel / Teflon junction. These

bubbles are clearly visible through the thin-walled Teflon sheath and can be removed with a pick. Once all the bubbles are removed, the hydrophone is reseated in its sheath and is ready for attachment to the tube.

The hydrophone is then run through the source and into the tube, taking care to keep it completely underwater. As before, the sheath is run out the baffled opening of the tube to attach the centering star. The centering star should be inspected to make sure no air is trapped on it before snapping it in place, about 10 cm behind the hydrophone. The hydrophone is then pushed back into the tube, such that the sheath-hydrophone junction is approximately in line with the plane of the tube opening. The proper setup is shown in Figure 3.17. The hydrophone sheath is then attached to the timing belt, close (within 5 mm) to the lower, non-drive shaft, pulley. After the sheath is attached to the timing belt, the stepper motor is used to accurately align the hydrophone with the tube opening. This is easily done by holding a machinist's scale or another straight, flat, thin object flush with the tube opening, and moving the hydrophone sheath until the tail of the hydrophone is in plane with the scale. The positioning system is zeroed at the computer at this point, allowing us to determine the position of the hydrophone inside the tube relative to the tube opening as required by the TFM. We found this method to be accurate in absolute position to ± 0.5 mm.

Once the positioning system is zeroed, the hydrophone is retracted into the tube approximately 2 centimeters. The tube is again rechecked for bubbles using the mirror and flashlight. If care was taken while de-bubbling the source and the tube (and the water is
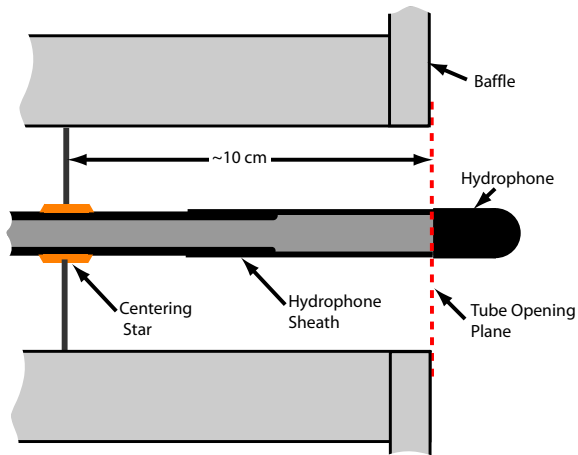
Figure 3.17: Proper hydrophone / tube alignment.

not super-saturated with air), there should not be any bubbles in the tube at this point. If bubbles are present, they can sometimes be removed with a miniature squeegee, or by inserting a tube with a bubble-free flow of water through it into the tube. Neither of these methods proved overly reliable, and the more than once the hydrophone sheath and source had to both be removed and realigned. If the rigging at the test facility permits it, we found that swinging the tube such that it is oriented vertically, with the tube opening facing up, de-bubbling around the hydrophone sheath was much easier as bubbles quickly rose out of the tube once swept away from the tube walls. If necessary, the HDPE window is attached at this point. The system is then lowered to testing depth and ready for measurements.

3.4.2 Reflection coefficient measurement procedure

Before reflection coefficient measurements are made, the sound speed inside the tube is measured. The sound speed is not only necessary for the TFM, its measurement also serves to verify that the tube is behaving properly. A number of electrical and mechanical problems with the tube were discovered making these measurements early in this work. The sound speed is measured using the two-point time of flight cross-correlation method described in Section 3.1.3.

The measurement of the transfer function, H_{12}, is straightforward. The hydrophone is positioned approximately 3 tube diameters from the tube opening, point 2 in Figure 3.1. As mentioned before, the tube's 1-16 kHz frequency range is broken into four bands. The transfer function between the hydrophone and the source excitation signal, H_{s2}, is measured by the VSA for each frequency band. The real and imaginary parts of the transfer function, as well as the measured coherence between the two signals, are transferred to a computer via GPIB and stored. The hydrophone is then positioned a distance s further back in the tube for the highest frequency band (8-16 kHz, $s = 2$cm). The signal cables (hydrophone and source) are switched at the VSA so that the transfer function between the source and the hydrophone, H_{1s}, is measured. This transfer function is measured and stored for all frequency bands, moving the hydrophone to the proper location for each band (see Section 3.1.2).

The transfer function between the hydrophone signals at each point is given by Eq. (3.8). The reflection coefficient is obtained using this transfer function and the measured

81

sound speed by Eq. (3.5). The measurement can be made over the entire frequency range in about 3 minutes. The underlying assumption behind this approach to measuring the reflection coefficient is that the sample being measured has acoustic properties that do not change within this time frame. This issue will be revisited later.

3.5 Verification of the impedance tube system

Before measurements of the baffled tube opening were made, a series of experiments were performed to verify tube performance[6]. The principal goal of these experiments was to show that the plane wave model, with a few corrections, can indeed be applied to our water-filled tube. Measurements were made with the tube oriented vertically, with the tube open to air, as illustrated in Figure 3.18. The tube was suspended in a large, cylindrical HDPE tank filled with filtered tap water. The water was partially degassed by heating it to 35° C and then allowing it to cool to room temperature. The water-air interface is the only termination to a water-filled tube whose theoretical result is truly "known." This termination is known as a *sound-soft* or *pressure-release*. The mathematics behind this termination are discussed in the next section, followed by a series of measurements made with the tube in this configuration.

---

[6]It should be noted that some of the data presented in this section were measured using earlier versions of certain components, such as the hydrophone sheath, centering star, and even the sound source (which had to be rebuilt twice over the course of the project). These components were replaced generally because they failed when deployed in the ocean, not in the laboratory. As these measurements were all made under relatively controlled conditions in the laboratory, any issues arising from use of these components are minimized. In all cases, although not every experiment presented in this section was repeated after each modification, the newer components can be expected to behave better than their predecessors.
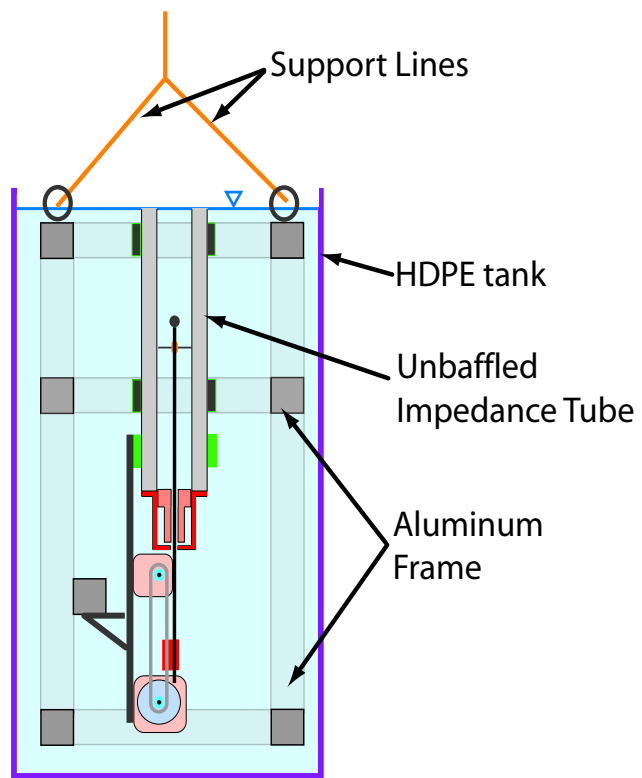
Figure 3.18: Laboratory setup for the verification of the impedance tube system.

3.5.1 The pressure release termination

As stated above, the only tube termination that is well-grounded in theory for a water-filled tube is the water-air interface. The specific acoustic impedance, $Z_0 = \rho c$, of air is around 400 kg/s m^2 while that of water is about 3700 times greater at $1.5 \cdot 10^6$ kg/s m^2. Equation (2.45) predicts a reflection coefficient of $\Re = -0.9994$ for a plane wave in water incident on air. For all practical engineering purposes we can take the value to be $\Re = -1$.

This is a very strong reflection and it creates a very strong standing wave pattern in the tube. When the sound field is excited by a rigid piston, as our source head may be modelled, the plane-wave pressure spectrum in the tube is

$$p\left(\omega, d\right) = \rho c u_0 \frac{\sin\left(kd\right)}{\cos\left(kL\right)} \tag{3.15}$$

where u_0 is the velocity of the sound source, L is the length of the tube, and d is the distance from the water-air interface. There are very strong resonances ($\cos kL = 0$) and anti-resonances ($\sin kd = 0$) in the spectrum, as will be plotted in the next section. As the sound speed in a water-filled tube is dispersive, all measurements and calculations used the frequency-dependent speed of sound predicted by the elastic tube theory (Section 3.2) for the experimental temperature.

3.5.2 Standing wave field

The only term in Eq. (3.15) that is dependent on position is $\sin kd$. To measure this dependence, the hydrophone was scanned from the tube opening in 6 mm steps until it was 30 cm into the tube. Measurements of the pressure spectrum were taken at each point.

Figure 3.19 shows the measured pressure as a function of distance from the tube opening at 7 representative frequencies. The data are normalized such that the largest pressure is 1. There is excellent agreement between the measurements and the theory for the lower frequencies, less than 10 kHz, and good to fair agreement at the higher frequencies[7].
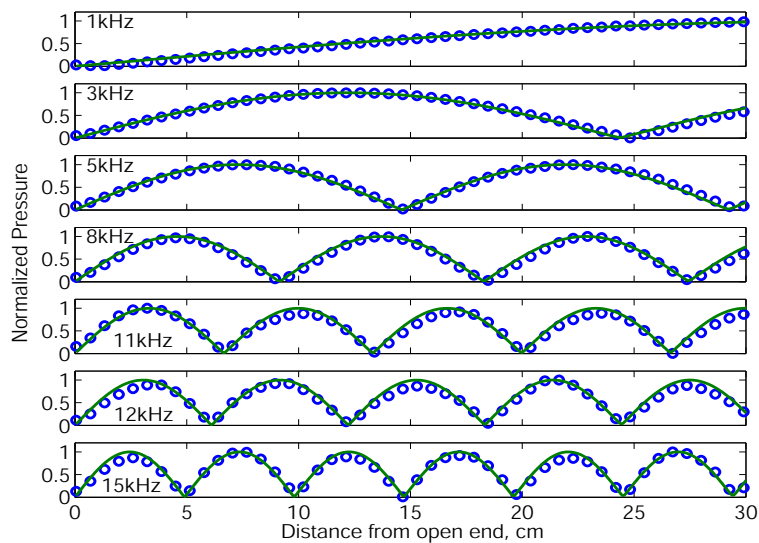
Figure 3.19: Measurement (open circles) of the standing wave pattern inside the tube at certain frequencies compared with theory (solid line).

The pressure spectrum as a function of axial position is shown in Figure 3.20. The tube resonances, clearly visible as white bands that run horizontally, occur a fixed frequencies independent of location. The anti-resonances, which are visible as curved black stripes, are functions of both frequency and location. For a given frequency, the distance between the

---

[7]It was eventually discovered that there was some mechanical coupling between the hydrophone sheath used in this experiment (which had an outer diameter 1/16 of an inch greater than the one described in Section 3.3.2) and the source, even when care was taken to properly align the two. This resulted in waves propagating along the sheath. This coupling was shown to be most pronounced (by looking at time-domain waveforms) at frequencies above 9 kHz, and could be responsible for the less-than-perfect measurements at these frequencies.

black lines corresponds to half a wavelength.
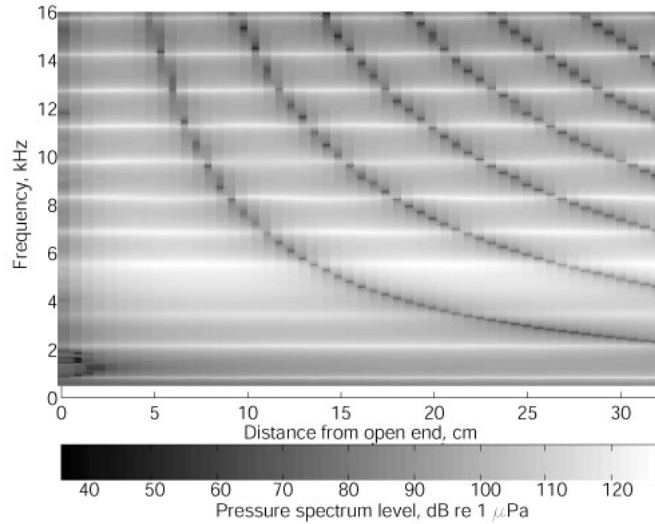
Figure 3.20: Measured pressure spectrum field inside the impedance tube at typical drive levels. Pressure resonances (white bands) and nulls (black bands) are clearly seen.

A measurement was made to confirm the validity of Eq. (3.15) in its full glory. A shear accelerometer was glued to the head mass of the source transducer such that it sat in the through hole flush with the face of the mass. The accelerometer cable is run out the back of the source through the hole. The accelerometer is used to determine the velocity of the source head, $u_0 = a/(-i\omega)$, where a is the measured acceleration. The hydrophone, which can no longer be run through the source, enters the tube from above and is positioned just below the air-water interface.

As absolute values are important in this measurement, it is necessary to account for the attenuation of sound in the tube. Although we neglected attenuation of sound in tubes before this point, there is always some, however little, due to viscous and thermal

losses. Attenuation manifests itself as the addition of a small imaginary component to the wavenumber which can be modelled as [64]:

$$k^2 = \frac{\omega^2}{c^2}\left(1 + \frac{\varepsilon\,(1-i)}{b}\sqrt{\frac{2c}{\omega}}\right)$$ (3.16)

where b is the inner radius of the tube and ε is a parameter accounting for the heat conductivity and viscosity of the fluid in the tube. Typical values of ε for clean water at $20°$ C are on the order of $10^{-4}\sqrt{\text{m}}$.

Figure 3.21 compares the measured pressure spectrum, in dB, to that predicted by Eq. (3.15) using the measured accelerometer data. The attenuation parameter, ε, was fit to these data, $\varepsilon = 7 \cdot 10^{-4}\sqrt{\text{m}}$. The measured and theoretical data agree rather well, although the peaks of the pressure resonances measured by the hydrophone are not as high as predicted by the theory for the lower frequencies. This suggests that attenuation in the tube has a frequency dependance not captured by Eq. (3.16) or, more probably, that the sound source does not act as a perfectly rigid reflector at all frequencies. In any case, the overall magnitude of the measurements and the theory are very much in line, especially at the high frequencies. If significant energy was being coupled into a higher mode, we would not see the high frequency agreement seen here.

The measurements shown here provide a good indication that our impedance tube / source combination met the design object of only propagating acoustic energy in a plane-wave like fashion. In the next section we will investigate how well the impedance tube serves its purpose as a measurement device.
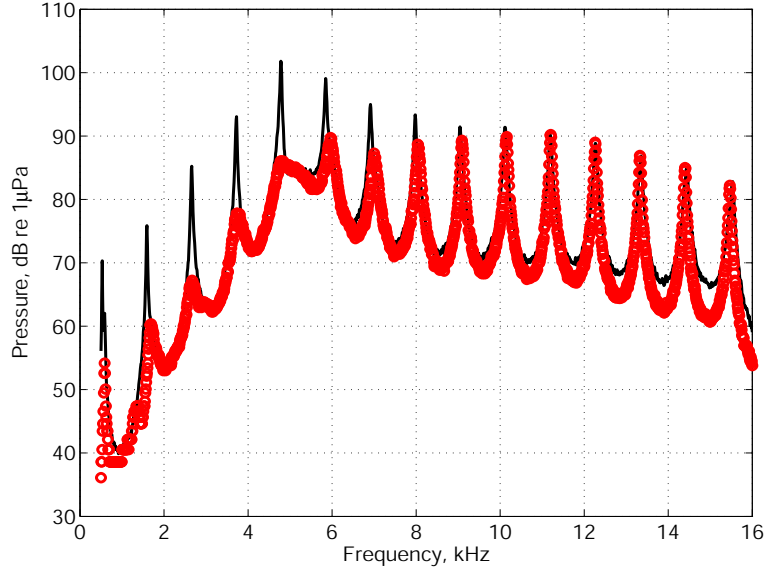
Figure 3.21: Pressure spectrum at a point just past the tube opening. Pressure level measurements (open circles) are plotted against Eq (3.15) using measured accelerometer data. The only fitting parameter used is the attenuation in the tube.

3.5.3   Impedance of a water-filled transmission line

In Section 2.1.2 it was shown that the impedance at any point in a tube is given by Eq. (2.18), repeated here for reference:

$$Z\left(d\right) = Z_0 \frac{e^{-ikd} + \Re e^{ikd}}{e^{-ikd} - \Re e^{ikd}}.$$

When $\Re = -1$ this reduces to

$$Z\left(d\right) = iZ_0 \tan\left(kd\right). \tag{3.17}$$

Note that when $d = 0$, $Z = 0$. It is not practical to try and measure the impedance at the tube opening directly as it is very difficult to measure zero. Instead, we measured the impedance at a plane some distance d from the tube opening. The impedance at this point

is given by Eq. (3.17) above. The section of tube between this plane and the tube opening

is known as a *water-filled transmission line*.

The impedance of a 25 cm long water-filled transmission line was measured using the procedure described in Section 3.4.2, only the distances ℓ and $\ell - s$ were taken from the imaginary plane at d, not from the tube opening. Figure 3.22 is a plot of the measured magnitude and phase of the transmission line. Also plotted is the impedance predicted by Eq. (3.17). Again, the attenuation parameter ε was fitted to the data, here $\varepsilon = 6 \cdot 10^{-4} \sqrt{\mathrm{m}}$. The data agree very well in both magnitude and phase with the theoretical prediction.
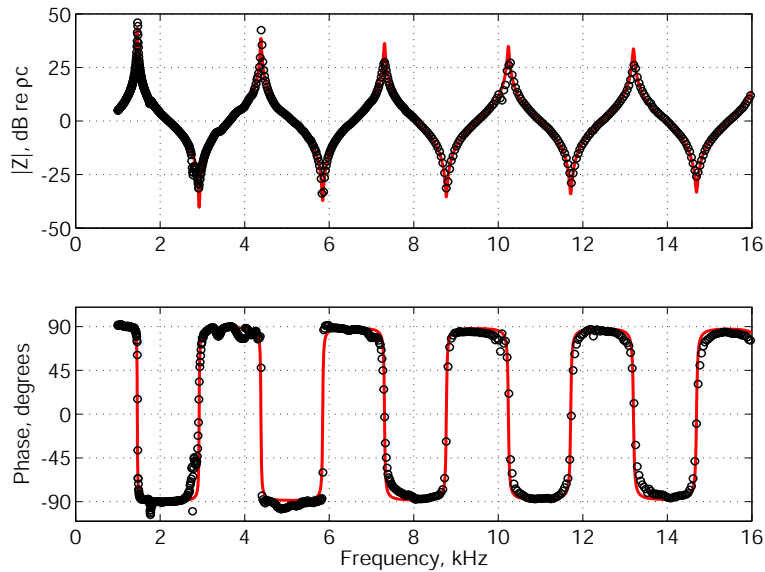
Figure 3.22: Impedance of an air-terminated 25.0 cm long water-filled transmission line, measurements (open circles) and theory (solid line).

Wilson [31] showed that the previous water-filled tube could measure, extremely accurately, the magnitude (1) and phase (180°) of the reflection coefficient, $\Re = -1$ at the water-air interface. In an attempt to duplicate his result, the data shown above were repro-

cessed. The TFM parameter ℓ was adjusted so that it fell at the water-air interface. The reflection coefficient was then recalculated. The results are shown in Figure 3.23 against the expected values. Even though this set of data gave very good results for the impedance of a water-filled transmission line (which are in line with those reported by Wilson and Roy [34] for a single-hydrophone system), the corresponding measurement of the reflection coefficient is in poor agreement with our expectations.
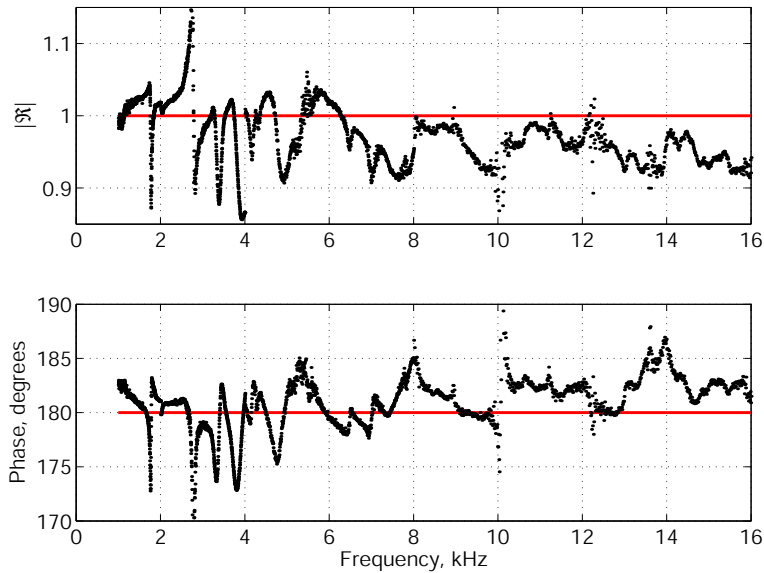
Figure 3.23: Magnitude and phase of measured reflection coefficient (dots) at the tube opening. Solid lines represent the theoretical sound-soft solution.

As the measurement of the water-air interface made by this tube was significantly worse than those made its predecessor, an explanation is in order. The previous tube was more precise in this measurement for at least three reasons. The first is that it was calibrated against a pressure-release termination (see [1]), thereby forcing the system to behave nicely in a situation where the TFM would otherwise not perform as well (see next section). A

second reason is that the previous tube was used solely in the laboratory and did not require submersion for normal use, allowing all variables to be near-perfectly controlled. With the new impedance tube, which must be submersed during both assembly and use, control over such things as alignment, water quality, and bubbles is much more difficult. Finally, the previous impedance tube used two, high mechanical impedance, wall-mounted hydrophones instead of a single scanned sheathed hydrophone. Both the wall-mounted and the scanned hydrophones perturb the sound field in the tube ever so slightly. As the wall-mounted hydrophones are fixed in place and the signals from the two hydrophones are measured at the same time, any perturbations have little effect. Unlike the previous system, the scanned hydrophone used here is moved between measurements, which are made at two distinct times. Any perturbation caused by the presence of the hydrophone and its sheath will be slightly different when each measurement is made. As we will see in Section 4.3, the single-hydrophone TFM is very sensitive to slight changes of system parameters between the two measurements.

3.6   Error, uncertainty, and sensitivity analysis

Errors in our measurement procedure come from two possible categories: those errors inherent in the transfer function measurement itself and those due to uncertainty in the measured TFM input parameters. Errors inherent in the transfer function method are addressed by reviewing works in the open literature and applying those results to our system. The uncertainty and sensitivity analysis are performed with a numerical model of the impedance tube

system. In all cases, discussion is limited to two tube terminations: the water-air interface and the theoretical baffled tube opening (with water both inside and outside the tube). The reflection coefficient predicted for bubbly liquids generally behaves as if somewhere between these limits.

3.6.1 Errors in the transfer function measurement

Errors inherent in the measurement of the transfer function come in two flavors: bias errors and random errors. Bias errors arise because of noise, nonlinearities and poor spectral resolution. Bias errors tend to be largest for highly reflective surfaces (such as a water-air interface), and are typically worst when one of the hydrophones is located at a pressure null. The maximum normalized bias error, ϵ_b in the measured transfer function, H_{12} is [74]

$$\left| \epsilon_b \left(|H_{12}| \right) \right| \leq \frac{8\pi^2 \Delta f^2 \ell^2 |\Re|^2}{3c^2 \left(1 - |\Re| \right)^2} \tag{3.18}$$

where Δf is the measurement frequency resolution. The most startling feature of this equation is that there is a singularity when $|\Re| = 1$, confirming our statement that strongly reflecting surfaces are most prone to these errors. It is important to note that although this is an upper bound on the error at all frequencies, it provides a good estimate of the error at those frequencies corresponding to pressure nulls at either hydrophone [74]. Away from the pressure nulls, the bias error is usually much smaller than predicted above.

Equation (3.18) also provides insight into what parameters can be changed to minimize bias error, such as placing the hydrophones close to the measurement plane and using small frequency resolution. In the case of the water-air interface, where $|\Re| = 0.9994$, Eq. (3.18)

dictates a value of

$$\ell^2 \Delta f^2 \leq 0.00029$$

is required if the bias error in the transfer function measurement is to be less than 1%. This is a very small number, requiring a frequency resolution that is not practically achieved with even the most modern signal analyzers. For the values of ℓ and Δf used in the reflection coefficient measurement in Section 3.5.3, the maximum bias errors predicted by Eq. (3.18) are well above 50%. This could explain the poor reflection coefficient measurement, as the the closest hydrophone was 30 cm from the tube opening (5 cm from the imaginary plane marking the start of the water transmission line) and there were many nulls in the pressure spectrum at the measurement points.

When the reflection coefficient is not as strong, such as that for the water-filled baffled tube radiating into water (Figure 2.11), the maximum bias error is much lower for reasonable values of $\ell^2 \Delta f^2$. Figure 3.24 shows the predicted bias errors in the measurement of the transfer function in a baffled tube whose reflection coefficient is given by Eq. (2.46). Here the values of ℓ and Δf are the same as those used in actual experiments (see Section 3.1.2).

Unlike bias errors, random errors do not depend on any tube parameters (such as sound speed, measurement location, or reflection coefficient) directly. The normalized random error, ϵ_r, in the measurement of the transfer function is [62]

$$\epsilon_r \left(|H_{12}| \right) \approx \sqrt{\frac{1 - \gamma^2}{2N\gamma^2}} \tag{3.19}$$

where γ^2 is the measured coherence function between the two hydrophone signals and N is the number of averages. While Eq. (3.19) is not directly dependent on the reflection
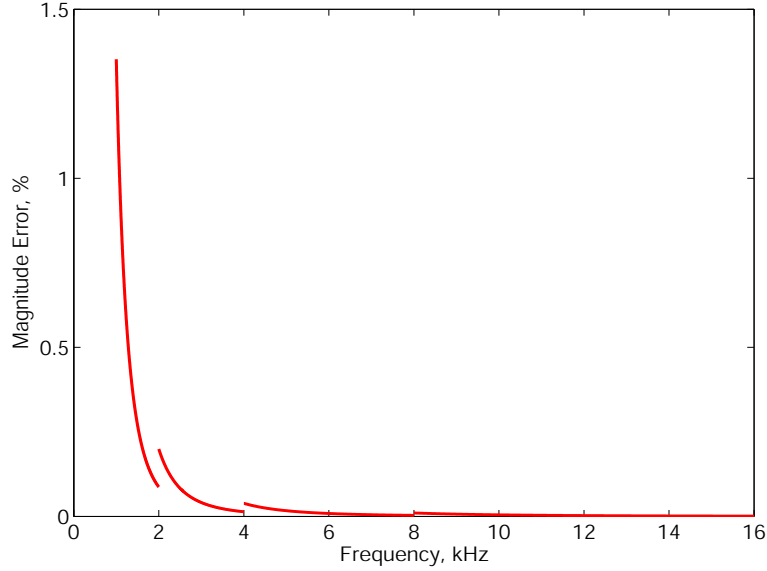
Figure 3.24: Predicted bias error for in the measurement of the transfer function for a baffled tube opening using the measurement parameters (hydrophone locations, frequency resolution) used for actual measurements. The discontinuities in the curve are the result of the discrete hydrophone positions.

coefficient, the coherence function is usually lowest when one hydrophone is located at a null in the pressure spectrum. Measurements of strongly reflecting terminations, which have sharp pressure nulls, will therefore be more suspectable to random errors. In general, coherence is improved if the spacing between hydrophones is minimized [74, 62]. Estimates of random errors will be given for measurements presented in Chapter 4.

Estimates of bias and random errors in the measured phase of the transfer function can be predicted in the limits of $|\epsilon_b| << 1$ and $\epsilon_r << 1$ [74]. The maximum bias error, β_b of the phase, φ, in radians, of the measured transfer function, H_{12} is

$$|\beta_b(\varphi)| \leq |\epsilon_b(|H_{12}|)|. \tag{3.20}$$

The standard deviation, σ_r, of the variation in phase, φ of the measured transfer function

94

due to random errors can be approximated as

$$\sigma_r \left(\varphi \right) \leq \epsilon_r \left(|H_{12}| \right).$$

(3.21)

3.6.2 Uncertainty and sensitivity analysis

A numerical simulation of the pressure field inside was used to investigate how sensitive the transfer function method is to the uncertainty in system inputs (wave number and hydrophone location), and to noise other perturbations from the ideal setup. This simulation was carried out in the frequency domain, where the pressure at any point in a tube excited by a rigid piston source is given by

$$p \left(\omega, d \right) = P_0 \frac{e^{-ikd} + \Re e^{ikd}}{e^{-ikL} - \Re e^{ikL}}$$

(3.22)

where L is the length of the tube, d is the distance from the tube opening, and $P_0 = -\rho c u_0$ and u_0 is the velocity of the source face. For these simulations $P_0 = 1$ was used for simplicity.

A significant cause of error in the measured reflection coefficient stems from uncertainty in the measured input parameters to Eq. (3.5), repeated here for reference

$$\Re = \frac{H_{12} - e^{iks}}{e^{-iks} - H_{12}} e^{-ik2(\ell)}.$$

These parameters include the measured phase speed, c_p, absolute hydrophone location, ℓ, and relative hydrophone spacing s. The phase speed was generally known to within ± 4.5 m/s. Uncertainty in the absolute location of the hydrophones stems from three factors: hydrophone / tube alignment, positioning system accuracy, and the location of the hydrophone's acoustic center. In Section 3.4.1 it was stated that this alignment was generally

better than ± 0.5mm. The positioning system was much more accurate, within ± 0.12mm over its full range. The acoustic center of the Brüel and Kjær is known within ± 0.3mm. Together, these three sources result in a total uncertainty of ± 0.92mm. Uncertainty in the relative location of the two hydrophones (the hydrophone spacing, s) is only dependent on the positioning system, ± 0.12mm.

Uncertainties in hydrophone position influence the reflection coefficient calculations as $\exp(ikx)$, (see Eq. (3.5)) where x is the distance parameter ℓ or s. As $k = \omega/c_p$, the maximum uncertainty in the measured reflection coefficient occurs when the smallest value of c_p is used with the largest value of x within their respective uncertainties (and vice-versa). These uncertainties are simulated in the numerical model as follows. First, Eq. (3.22) is used to provide the ideal complex pressures at the exact points in the tube required by the TFM ($p_1 (d = \ell)$ and $p_2 (d = \ell - s)$). The ideal "measured" transfer function, H_{12} is obtained by dividing p_2 by p_1. The reflection coefficient is calculated as usual, except the values of kx reflecting the uncertainties are used.

Figures 3.25 and 3.26 show the uncertainty envelopes in magnitude and phase for simulated pressure-release and baffled tube openings, respectively. As shown in the figures, measurement uncertainties in the TFM input parameters lead to error in the phase alone. The uncertainty in the relative hydrophone locations, s was found to be negligible, contributing at most $0.5°$ change in phase at the highest frequency.

This numerical model was also used to simulate the effect of noise on the system. The noise was added in the frequency domain as follows. Equation (3.22) was used to create the
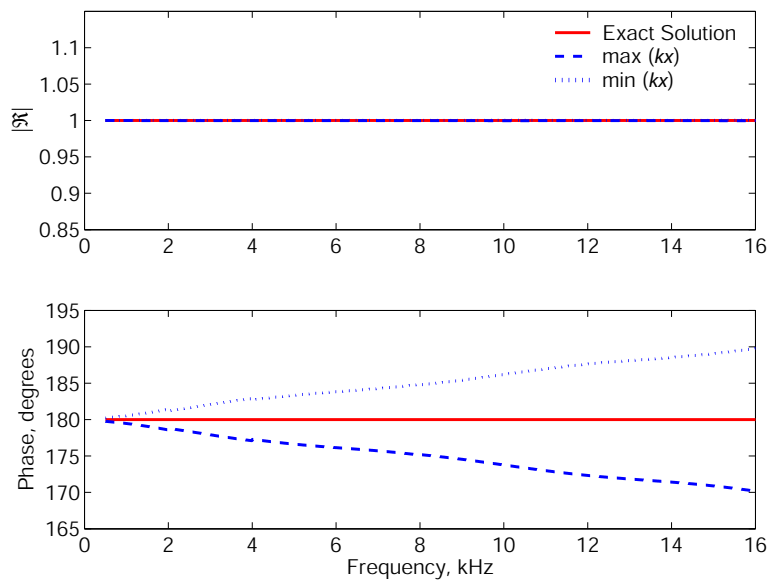
Figure 3.25: Effect of uncertainty in measured TFM input parameters for a simulated pressure-release tube termination.
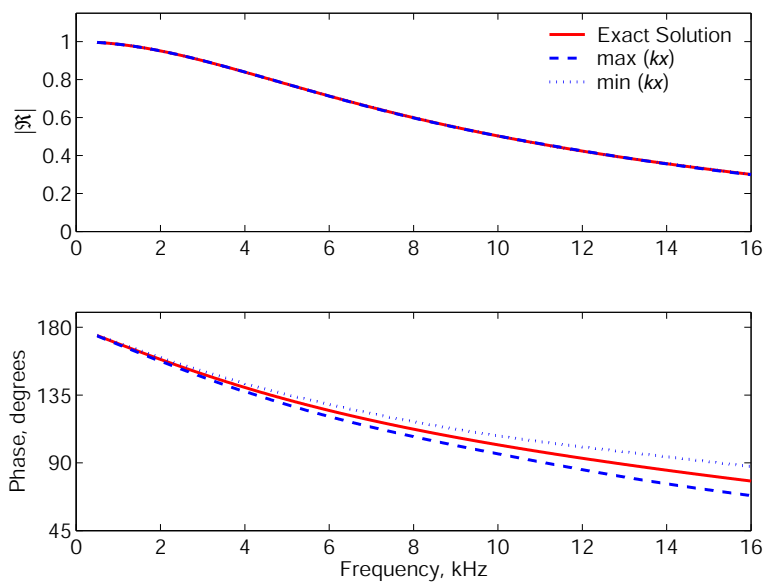
Figure 3.26: Effect of uncertainty in measured TFM input parameters for a simulated baffled tube opening.

97

ideal pressures at the two points. Before the calculating the transfer function, "noise" was added to the pressure spectra as

$$p_{n1,n2} = \mathrm{Re}\,(p_{1,2}) + \xi\,(f)\,P_0 + i\,(\mathrm{Im}\,(p_{1,2}) + \xi\,(f)\,P_0) \qquad (3.23)$$

where $p_{n1,n2}$ is the noisy pressure measurement, P_0 is the pressure spectrum coefficient in Eq. (3.22), and $\xi\,(f)$ is a random noise function, re-calculated each time it is called, bounded by $-2.0\% < \xi < 2.0\%$. The pressures were kept as complex quantities (hydrophones only measure real pressures) to simulate noise in the measured complex transfer functions between the hydrophones and the source, H_{2s}, H_{s1} used in the single-hydrophone TFM. The transfer function between the two "measured" pressures was then calculated as $H_{12} = p_{n2}/p_{n1}$ and the "measured" reflection coefficient was calculated as usual.

Again, both the pressure-release and baffled tube openings were investigated. The results of the simulation are shown in Figure 3.27 for the pressure-release termination and in Figure 3.28 for the baffle tube opening. Three plots are shown in each figure. The upper plot is the magnitude of both the ideal, p_2, and the noisy, p_{n2} pressures at the hydrophone closest to the measurement plane. The two plots are almost indistinguishable on the decibel scale, giving an indication of just how little noise was added. The middle and lower plots are the magnitude and phase of the reflection coefficient, respectively. Here, the effect of the noisy "data" on the measurement is clearly visible.

Equation (3.18) predicts that the transfer function method is most susceptible to bias errors when measuring strongly reflective surfaces, and this effect is shown in the noise simulations. The strongly reflecting pressure-release simulation (Figure 3.27) shows a rela-
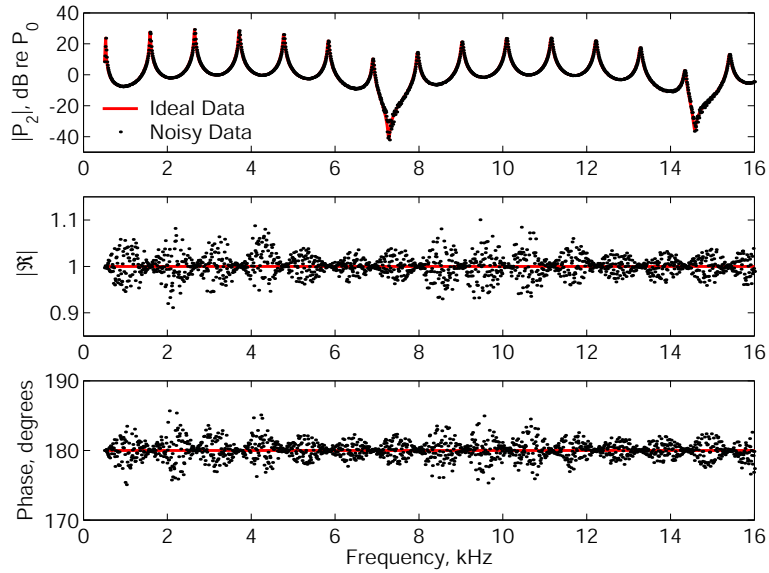
Figure 3.27: Numerical simulation of an impedance tube terminated with a sound soft surface. Both ideal (line) and noisy (dots) data are shown.
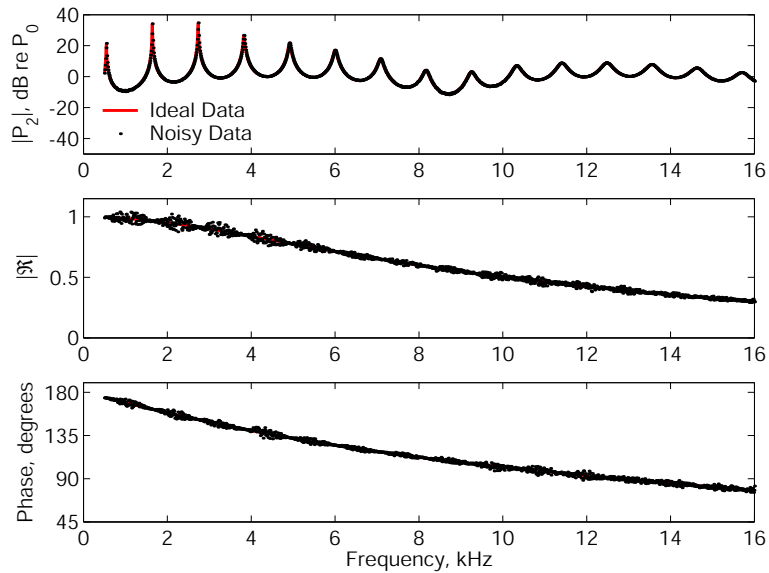
Figure 3.28: Numerical simulation of an impedance tube terminated with an infinite, rigid baffle. Both ideal (line) and noisy (dots) data are shown.

tively constant amount of error at all frequencies. The amount of error in the magnitude of the measured reflection coefficient for noisy baffled opening simulation (Figure 3.28), which is strongly reflective at low frequencies but significantly weaker at high frequencies, gets noticeably smaller as the frequency increases. In both simulations, the noise affects the measurement less at tube resonances, where the magnitude of the pressure is much greater than the noise level.

Chapter 4

Experimental Results and Analysis

This Chapter is divided into three sections. The first deals with experiments carried out to visit how well our baffled tube system is modelled by the theory developed in Section 2.1 for a rigid tube with an infinite, rigid baffle. These experiments were made with water both inside and outside the tube. The second section covers a preliminary experiment made with an uncharacterized bubbly liquid outside the tube in our laboratory. The final section details a set of experiments conducted with a well-characterized bubbly liquid outside the tube at a state-of-the-art Naval facility.

4.1   Radiation of a baffled water-filled tube into water

Experiments were carried out at the Naval Undersea Warfare Center's acoustic test facility at Dodge Pond in Niantic, CT. Dodge Pond is a freshwater reservoir with remarkably low ambient noise. The 133,500 m^2 pond is about 16m deep in the center with a very soft,

muddy bottom. The primary test facility is a climate-controlled building located at the center of the pond and kept afloat by a number of large pontoons. The center of the facility is open to the water, with a number of large overhead winches for the deployment of underwater acoustic experiments. The facility is also instrumented to allow for a quick measurement of the temperature and sound speed profile as a function of water depth.

The impedance tube system was aligned and prepared in the standard manner outlined in Section 3.4.1. The test facility allowed for access to the tube at the waterline, allowing it to be completely flooded and assembled underwater. Once assembled and the positioning system zeroed, the device was lowered to a depth of about 8 m, as illustrated in Figure 4.1. A series of measurements were made of the impedance at the tube opening and of the pressure field radiated out from the tube along its axis. A discussion of these measurements follows.

4.1.1 Radiation impedance of a baffled tube opening

The first measurements made at Dodge Pond were of the radiation impedance and reflection coefficient at the opening of our baffled tube. Measurements of the reflection coefficient, $\Re$, were made exactly as described in Section 3.4.2. The impedance of the opening, Z_n, was then calculated from the reflection coefficient by Eq. (2.19). Typical measurements of the magnitude and phase of the reflection coefficient and impedance are shown in Figures 4.2 and 4.3, respectively. The measurements are compared with the theoretical result predicted by Eq. (2.47). Equation (2.47) was used for the theoretical result even though there was water both inside and outside the tube (as opposed to Eq. (2.46) which assumes the two
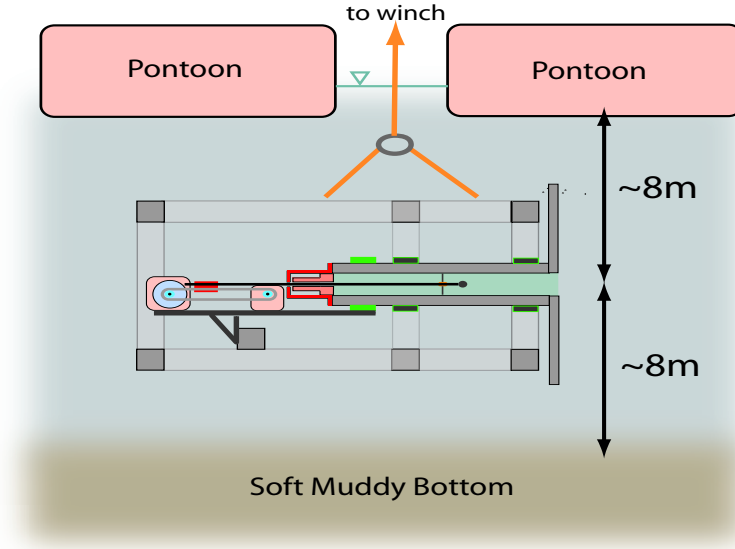
Figure 4.1: Relative impedance tube deployment location at the Dodge Pond acoustic test facility (not to scale).

fluids are the same), allowing us to correct for the slightly lower phase speed inside the tube. The ratio of specific impedances, γ, was taken as

$$\gamma = \frac{\rho c_p}{\rho c} \tag{4.1}$$

where c_p is the measured phase speed in the tube and c is the intrinsic speed of sound in the water at the experimental temperature.

These measurements show fair agreement with the theoretical prediction. The low frequency data (< 3 kHz) are particularly poor and messy, most likely due to the relatively low source level (and therefore low signal to noise ratio) at these frequencies. The data also show poor agreement with the theory in the 10-12 kHz range. The exact cause of this disagreement remains unknown, but this feature disappeared in later measurements leading us to believe one or more bubbles were caught either in the tube or on the baffle during
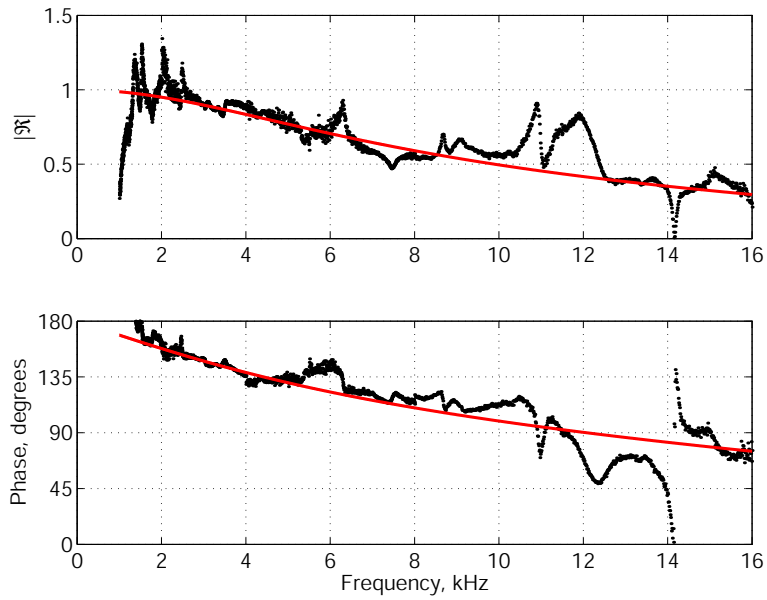
Figure 4.2: Magnitude and phase of the measured (dots) and theoretical reflection coefficient at the tube opening.
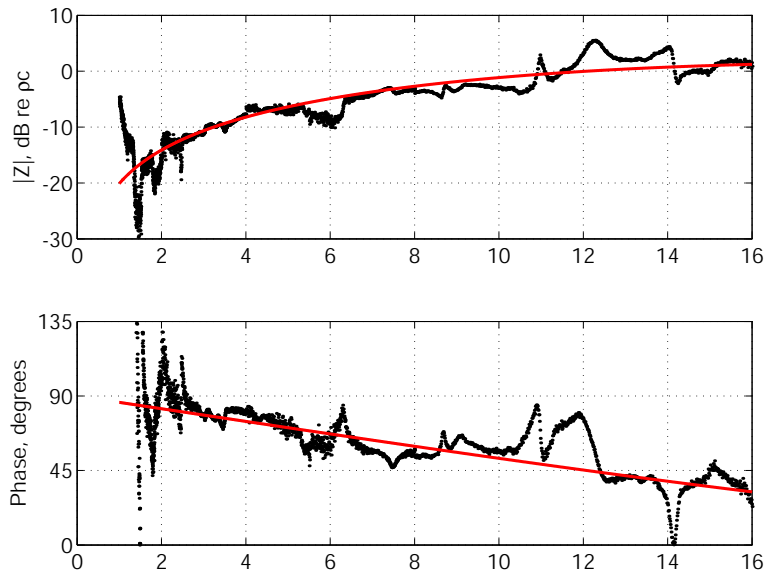
Figure 4.3: Magnitude and phase of the measured (dots) and theoretical impedance at the tube opening.

the first experimental measurements. Another noticeable deviation from the theory occurs around 14 kHz, where there is a small dip in the magnitude and a large blip in the phase of the measured reflection coefficient. As mentioned before the first cutoff frequency in a water-filled tube of our dimensions is around 14 kHz (the exact value is a function of the temperature dependent sound speed of water). This feature almost certainly results from an unmodelled higher-order mode (or modes) either propagating in the tube or present at the tube opening.

Experiments were then carried out to visit how sensitive the apparatus was to the depth of deployment. The reflection coefficient was measured at ~ 1.9 m intervals from 8 to 0.3 m below the surface. One would expect that the closer the instrument is to the surface, reflections from the water's surface would interfere with the sound field at the tube opening and corrupt the measurements. This effect, if present, would be most pronounced at lower frequencies, where the acoustic wavelengths are longest. The measured reflection coefficients are shown in Figure 4.4.

There is some disagreement between the measured data for all depths below about 2.5 kHz, where the data were noisy to begin with. The data from the two depths closest to the pond surface (2.2 and 0.3 m) do show significant departures from the other data and the theoretical result up to 4 kHz. For the 0.3 m depth, the top of the baffle was right at the waterline. This suggest that, for our impedance tube system, surface reflections may not play that significant of a role at frequencies above 4 kHz, regardless of depth. This is encouraging because we model our finite sized baffle as being infinitely large. Another

105
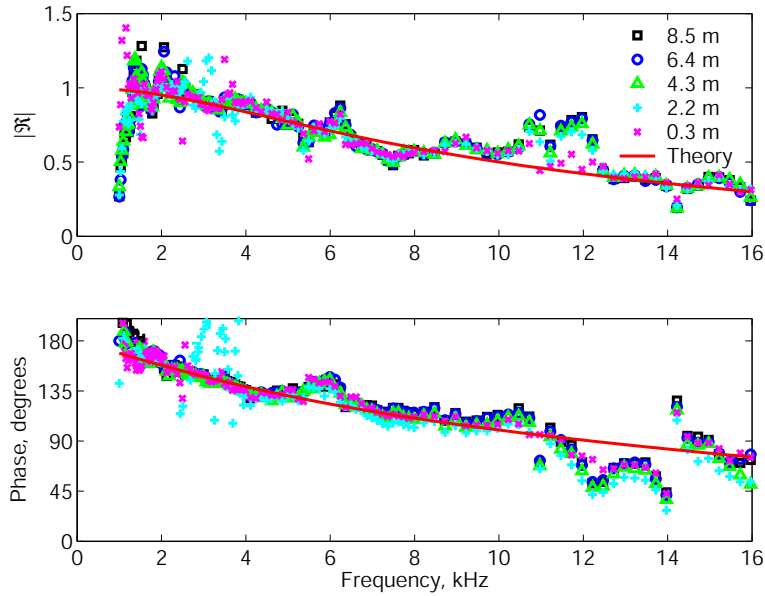
Figure 4.4: Variation of the magnitude and phase of the reflection coefficient with the depth of the tube below the water surface. Only every 20th data point is shown for clarity.

interesting observation is that the measurement made at 0.3m ("X's" in Figure 4.4) are closer to the theoretical result in the 10-12 kHz range than the other measurements. This suggests, as mentioned before, that one or more bubbles may have been responsible for the poor agreement in the 10-12 kHz range but were dislodged as the apparatus was raised during this experiment.

Measurements of the reflection coefficient were also made with our HDPE window in place to test our assertion that it can be modelled as acoustically transparent. The window was attached after the depth-dependency experiments while the tube was only 0.3 m below the surface. The instrument was then returned to a depth of 8 m. The measured magnitude and phase of the reflection coefficient with the window in place are shown in Figure 4.5. Although the low frequency results are still somewhat messy and the 14 kHz feature is still

present, the data fit the theory reasonably well at all other frequencies.
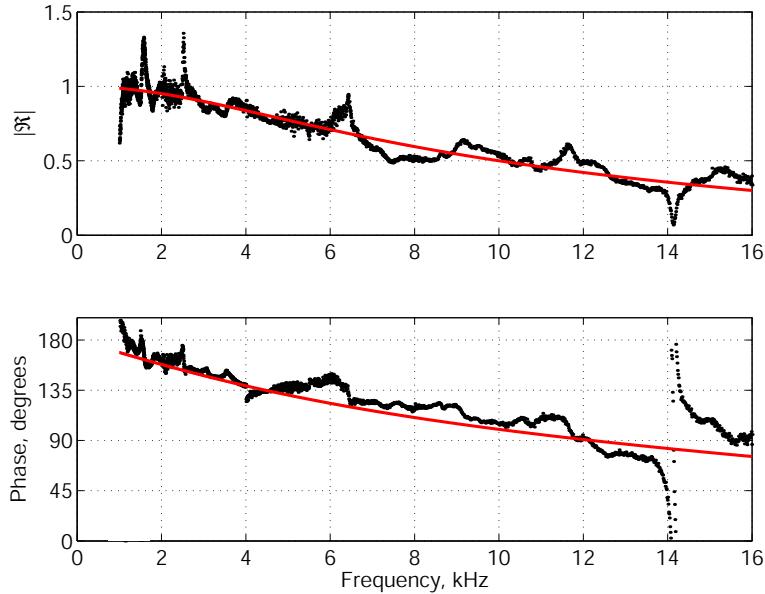
Figure 4.5: Magnitude and phase of the measured (dots) and theoretical reflection coefficient at the tube opening with the HDPE window in place.

A typical measurement of the coherence function, γ^2, between the two hydrophone signals is shown in upper plot of Figure 4.6 and the corresponding magnitude of random error, ϵ_r, in the measured transfer function given by Eq. (3.19) is shown in the lower plot. As discussed in Section 3.6.1, in a perfect system the coherence function would equal 1 (and the error magnitude would equal 0). Here, the coherence is significantly less than one at all frequencies, an indication of possible noise, bubble, or electrical problems. The extraordinarily low coherence between 4-6 kHz suggests the presence of a bubble, as bubbles tend to wreak more havoc around select frequencies (namely their resonant frequencies) than others. We most note that the data measured in this frequency range, although somewhat noisy, agree rather well with the theoretical result. The signal coherence issue is revisited

in Section 4.1.3.
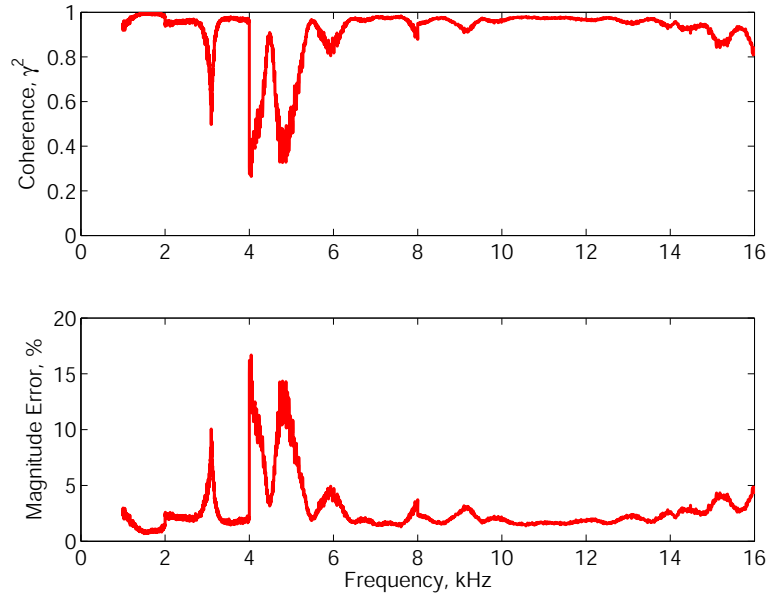
Figure 4.6: Measured coherence between the two hydrophone signals (upper plot) and corresponding estimated random errors in the measured transfer function (lower plot).

4.1.2   Radiated pressure along the tube axis

After the reflection coefficient measurements were completed, the hydrophone sheath was repositioned on the positioning belt to allow it to be scanned, along the tube axis, out from the tube opening. The hydrophone was positioned such that its acoustic center was in plane with the tube opening and the entire system was lowered to a depth of 5 meters. The tube was excited with 1-16 kHz random noise and the time-averaged pressure spectrum[1] was

[1]A random noise source was used because time constraints (measurements at all 47 spatial points were made in about 15 minutes) dictated that all frequencies be interrogated at once. It would have been much better to use a select number of pure frequency tones and measure the amplitude of the hydrophone signal at each point on an oscilloscope. In that setup, all signals could have been amplified to the same pressure level and band-pass filtered to reduce the effects of noise, which would have been especially beneficial at the lower frequencies.

measured at approximately 1.9 mm intervals from the tube opening until the hydrophone had travelled about 11 cm out of the tube.

Measurements at five select frequencies, normalized to the pressure at the tube opening, are plotted in Figure 4.7 as open circles. The lines represent the normalized theoretical pressure profile predicted by Eq. (2.31). The data agree fairly well with the predictions, especially for the middle and upper frequencies. The low frequency measurements are subject to significantly lower source level (see footnote), possibly accounting for the less-than-perfect results.
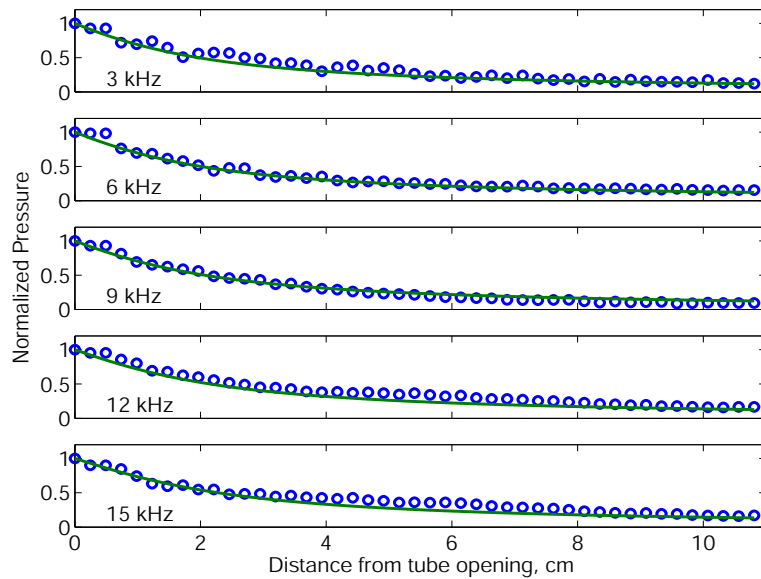
Figure 4.7: Radiated pressure profile as a function of distance from the tube opening. Measurements (open circles) are compared with the theoretical result (solid line).

4.1.3 Modifications to design after Dodge Pond

Although the Dodge Pond experiments were overall modestly successful, they revealed a number of shortcomings of the impedance tube system. The two biggest problems were poor source level at low frequencies and higher-order effects at the first cutoff frequency. Little could be done about the first cutoff frequency, save rebuilding the entire apparatus around a smaller tube or filling the tube with a fluid that has a higher sound speed. The source level problem, however, was manageable.

As we saw in Section 3.6, the TFM is very suspectable to errors if the signal to noise ratio is small. The low source level at low frequencies, due to the response of our sound source, was most probably responsible for the noisy low-frequency data from the Dodge Pond experiments. The sound source has a very high electrical impedance at low frequencies (see Appendix E), requiring higher a driving voltage to achieve the same radiation intensity. One possible solution is to drive the source with a higher voltage at the lower frequency ranges, but we generally operate near the saturation level of our power amplifiers. Another solution, which was adopted, is to lower the electrical load impedance of the source using an impedance matching transformer (matchbox).

An impedance matcbox, such as the Krohn-Hite MT-56 used here, is nothing more than a simple electrical transformer. Electrical transformers are devices that transfer energy from one electric circuit to another via a magnetic field without change in frequency [75, 76]. The magnetic field is created by a primary winding of wire and picked up by a secondary winding.

The equivalent electrical impedance, Z_{eq}, of the load with a transformer inline is

$$Z_{\text{eq}} = \left(\frac{N_1}{N_2}\right)^2 Z_{\text{load}} \qquad (4.2)$$

where N_1 and N_2 are the number of primary and secondary windings and Z_{load} is the electrical impedance of the load (i.e., our sound source). The MT-56 is designed to step up electrical impedances $((N_1/N_2) > 1)$ but can be run in reverse to step down the impedance. In this case, the turn ratio in Eq. (4.2) is flipped, $(N_1/N_2) \rightarrow (N_2/N_1)$. For the MT-56, (N_2/N_1) can be selected to be 0.1, 0.2, 0.4, or 0.8.

To provide the highest possible low-frequency source level, the lowest turn ratio, 0.1, was selected for the 1-2 and 2-4 kHz bands. A turn ratio of 0.8 was used for the remaining frequency bands (4-8 and 8-16 kHz) to provide some gain (but not enough to damage the source or other electronics). The matchbox proved remarkably efficient at improving the response of the source. The acceleration profile of the source head mass with the transformer inline is compared to that without it in Figure 4.8. The measured low frequency accelerations are close to an order of magnitude higher when using the matchbox.

To verify that the higher source level improves the quality of our measurements, the impedance tube system was suspended in the middle of a large, water-filled wooden tank approximately 3.3 m in diameter and 2.4 m deep. The impedance tube system was allowed to reach thermal equilibrium with the water in the tank and meticulously de-bubbled. The magnitude and phase of the reflection coefficient at the tube opening measured in the tank are shown in Figure 4.9. The low frequency measurements are significantly cleaner than those measured at Dodge Pond. The measurements also agree fairly well with the theoretical
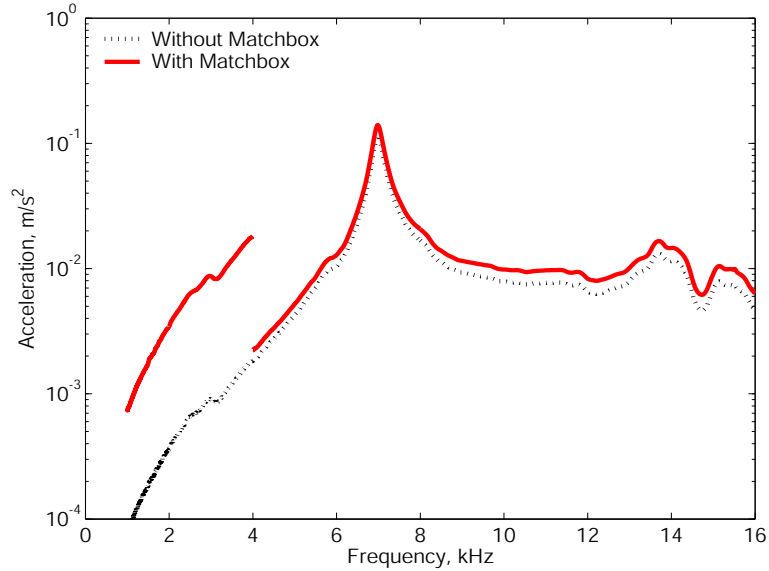
Figure 4.8: Acceleration of the source head mass with and without the impedance matching transformer inline.

result also plotted on the figure. This is interesting as the theoretical result was derived assuming that the tube opened into an infinite volume of fluid, but the dimensions of our tank are on the order of 2 wavelengths at 1 kHz. Tank modes and bottom, surface and wall reflections may, however, be responsible for some of the low-frequency deviations from the theory.

There was also significant improvement in the overall signal quality, as measured by the coherence between the two hydrophone signals (Figure 4.10, upper plot). The coherence function is nearly unity at all frequencies and the corresponding estimated random errors in the magnitude of the transfer function (lower plot) are well below 2%. This supports our statement that the Dodge Pond experiments were corrupted by either noise or bubbles as both of these issues were thoroughly addressed in this experiment.

112
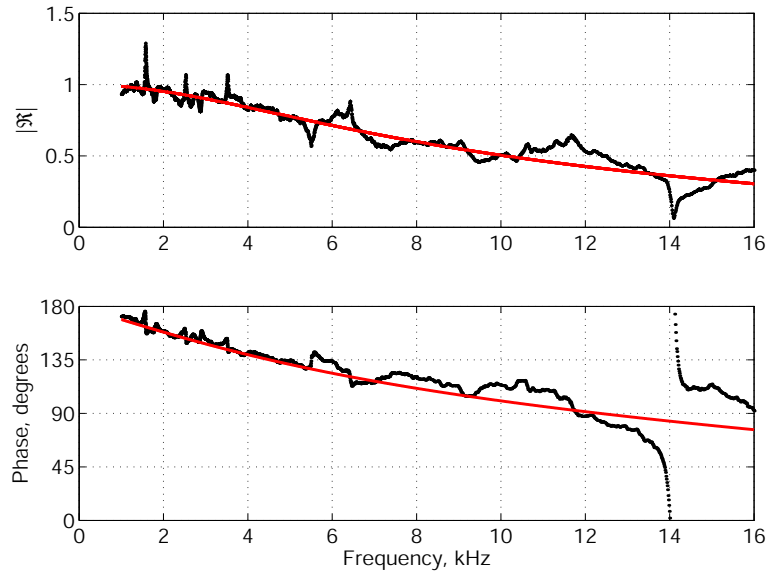
Figure 4.9: Magnitude and phase of the measured and theoretical reflection coefficient of a baffled tube opening using the impedance matching transformer.
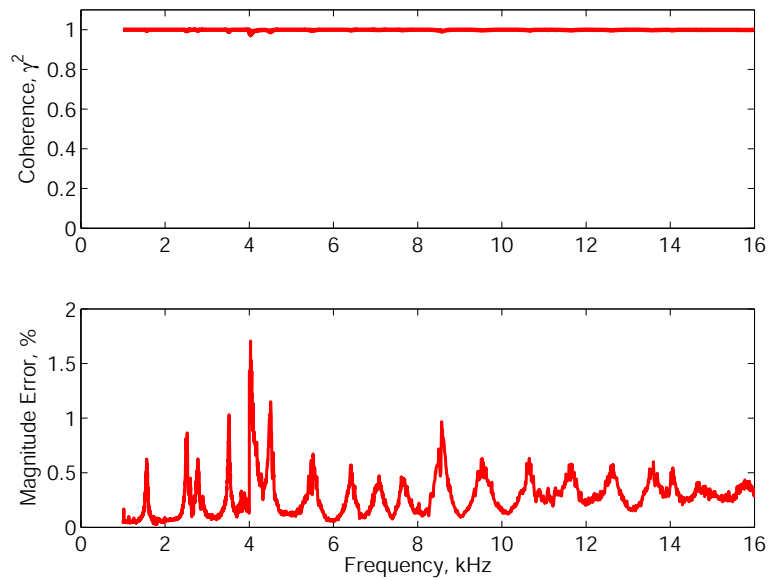
Figure 4.10: Measured coherence function between the two hydrophone signals (upper plot) and corresponding error in the magnitude of the measured transfer function (see Section 3.6.1).

4.1.4 Recapitulation

A low signal to noise ratio undoubtedly contributed to the less-than-perfect low frequency measurements at Dodge Pond as there was significant improvement in the quality of the measurements once the source level was raised. The impedance matchbox will be a standard piece of equipment from now on. There was also significant improvement in the coherence at the high frequencies without much gain in source level in the wooden tank experiments, a strong indication that there was some system non-linearity corrupting the Dodge Pond measurements. Bubbles remain the most likely culprit, possibly present either in the tube or just outside the tube during the Dodge Pond experiments. The water at Dodge Pond is host to a significant amount of organic matter which may both capture bubbles or create them in the process of decaying. It is possible that although care was taken to remove bubbles during preparation at Dodge Pond that some may have entered during the raising and lowering, or become attached to the face of the baffle. Although the wooden tank cannot be taken as an infinite body of fluid (as Dodge Pond could reasonably be assumed to be), it is a much more hospitable environment for de-bubbling.

The structure of the measured reflection coefficient (for instance where the measured data are greater or less than the prediction) in the wooden tank is remarkably similar to that measured at Dodge Pond (see Figure 4.5). This is a good indication of our system's robustness (we get similar results in different environments) but also affirms our worries that our baffle does not behave exactly as modelled. It is not, after all, either perfectly rigid compared to water or infinite in extent. In any event, the measured reflection coefficients

both at Dodge Pond and more so in the wooden tank are in relatively good agreement with the theory developed in Chapter 2.

4.2 Bubbly Liquids - Preliminary Experiment

Two sets of experiments were made measuring the reflection coefficient at the tube opening with a bubbly liquid outside the tube. The first, detailed in this Section, was a preliminary measurement made in our laboratory of a small bubble sample whose size distribution was not directly measured. The second set of experiments were made in a larger tank at the Naval Research Laboratory (NRL) in Washington, DC and are described in Section 4.3. In these experiments the tank was completely filled with bubbles and an attempt was made to simultaneously measure the bubble size distribution. While the results of the preliminary experiment were promising, the NRL experiments encountered problems with the impedance tube system and super-saturated water.

4.2.1 Experimental setup

The preliminary bubbly liquid experiments were carried out in the same wooden tank discussed in Section 4.1.3. Bubbles are produced by an array of five fish tank bubblers. The bubblers are porous tubes about 20 cm in length mounted with suction cup clips on a plastic platform as illustrated in Figure 4.11. Large brass feet, not shown in the Figure, are bolted to the bottom of the platform, providing support and adding enough weight so that the entire assembly sinks in water. The bubblers are feed compressed air from a small

plenum also attached to the platform. The plastic air lines leading from the plenum to the bubblers are valved such that the air flow to each bubbler can be adjusted individually. The plenum is feed by a regulated compressed air tank. Before the bubbler platform is lowered to the bottom of the tank, the air flow is turned on with the bubblers just below the surface. The valves are adjusted until all five bubblers have visually similar bubble production rates. A broad distribution of bubbles was created by the bubblers. Visual inspection next to a machinists scale showed that most bubbles were below 1 mm in radius but a few existed up to 2 mm. The void fraction was estimated, visually, to lie between 0.05 and 2%.
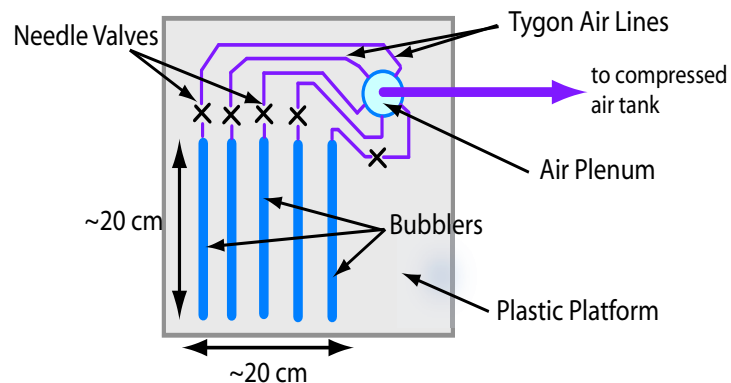
Figure 4.11: Illustration of the bubbler used for the preliminary bubbly liquid experiments.

Once the bubbler valves are adjusted the platform is lowered to the bottom of the tank and positioned so the bubbles rise just in front of the tube opening. This setup is shown in Figure 4.12. The opening of the tube is fitted with the HDPE window to keep bubbles from entering the tube. The reflection is measured using the standard procedure. Results from a typical measurement are shown in Figure 4.13.
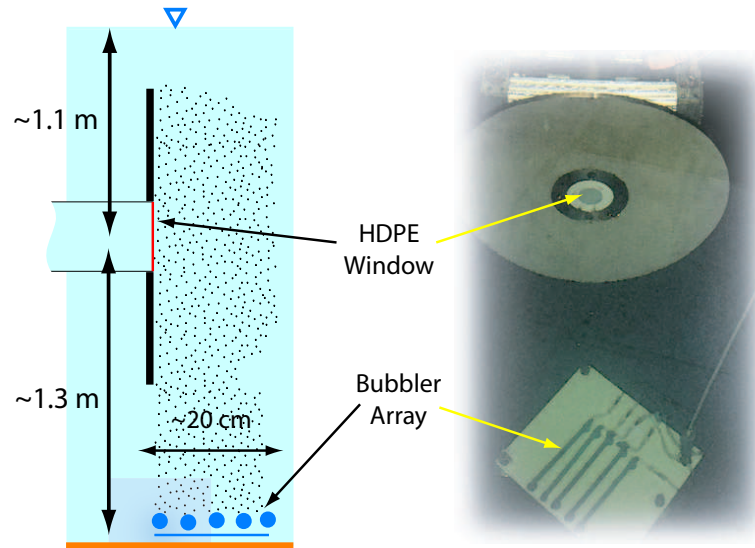
Figure 4.12: Illustration (left) and photograph (right) of impedance tube setup used for the preliminary bubbly liquid experiments.
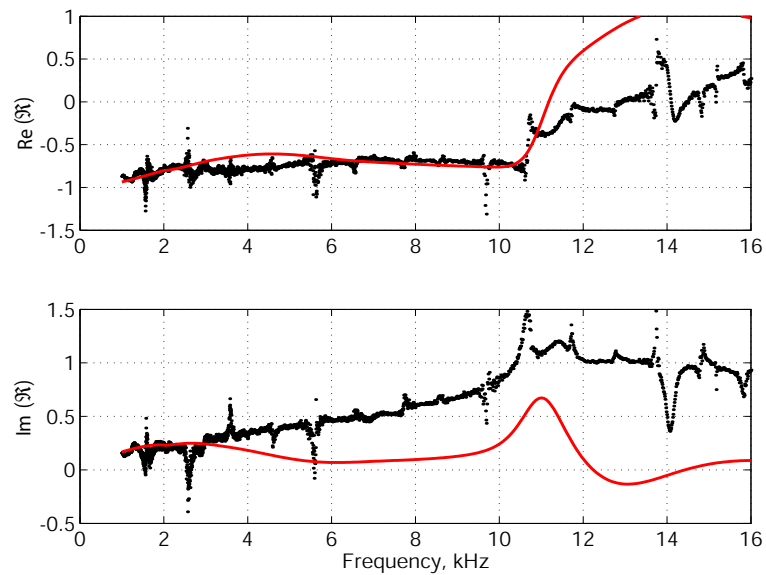
Figure 4.13: Real and imaginary components of the measured reflection coefficient (dots) compared to the theoretical prediction for a bubbly liquid with the bubble size distribution shown in Figure 4.14 using Eq. (2.74).

4.2.2 Preliminary results

Also plotted on Figure 4.13 is a theoretical reflection coefficient for a bubble population that was fitted to the data (but still matched the observations made by eye). The fitting process will be briefly summarized here. The real part of the measured reflection coefficient shows a shift away from $\text{Re}\,(\Re) \approx -1$ around 10.6 kHz. This shift can be explained by the sudden rise in phase speed of a bubble liquid at the resonance frequency of the individual bubbles that comprise it. The bubble distribution was therefore centered around bubbles that resonate at 10.6 kHz. The larger bubbles that were observed also had to be accounted for, requiring a large "tail" on the distribution. A standard Gaussian distribution is not suited for such a population. A sum of log-normal bubble size distributions was chosen instead. The log-normal distribution used here has the form of

$$\wp\,(a) = C \exp\left(-b\left(\ln\left(\frac{a}{a_0}\right)\right)^2\right) \tag{4.3}$$

where a_0 is the center bubble radius, b is the log-normal equivalent of the Gaussian standard deviation, and C is a constant that scales to the void fraction. In this case, the void fraction was set to 0.1% to reduce the number of fitting parameters. The final distribution, fit by adjusting the absolute values of b and the relative values of C in a sum of log-normal distributions, is shown in Figure 4.14.

The preliminary results were encouraging. Although the bubble size distribution was not measured directly, the data show features that are consistent with a reasonable fitted bubble population, such as the departure from $\text{Re}\,(\Re) \approx -1$ and the peak in the imaginary component at the resonant frequency of the center bubble size. Without a simultaneous
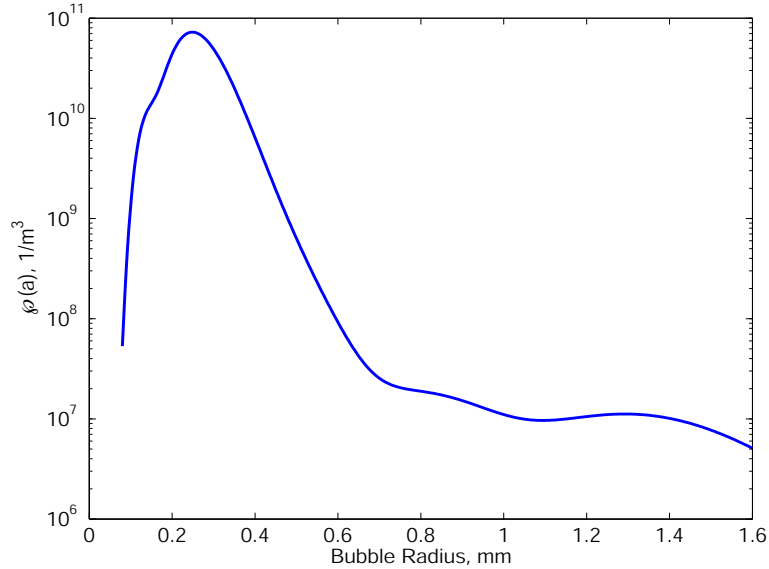
Figure 4.14: Estimated bubble size distribution. The peak in the distribution corresponds to bubbles that resonate around 10.6 kHz.

measurement of the bubble size distribution, however, the effectiveness of the tube cannot be judged with any certainty. We also note that there are small, period, "blips" in the data at approximately 1.4 kHz intervals. The cause of this structure is examined in Section 4.3.3.

4.3   NRL Salt Water Tank Facility experiments

The bubble tank facility at the Naval Research Laboratory, officially designated as the Salt Water Tank Facility (this is somewhat of a misnomer as the tank was filled with fresh water at the time), is unique. The tank itself is very large, some 6 m wide by 6 m long by 3 m deep with porous tube bubblers (originally designed to aerate catfish hatcheries) lining its floor. The tank geometry is illustrated in Figures 4.15 and 4.16. Each of the 40 bubblers is feed with an individually regulated air line that includes a volume flow-meter. The bubbler

air lines are supplied by a series of three large, individually regulated, plenums which are in turn supplied by a large industrial air compressor. The facility is also equipped to with an underwater digital video camera system to measure the bubble size distribution.
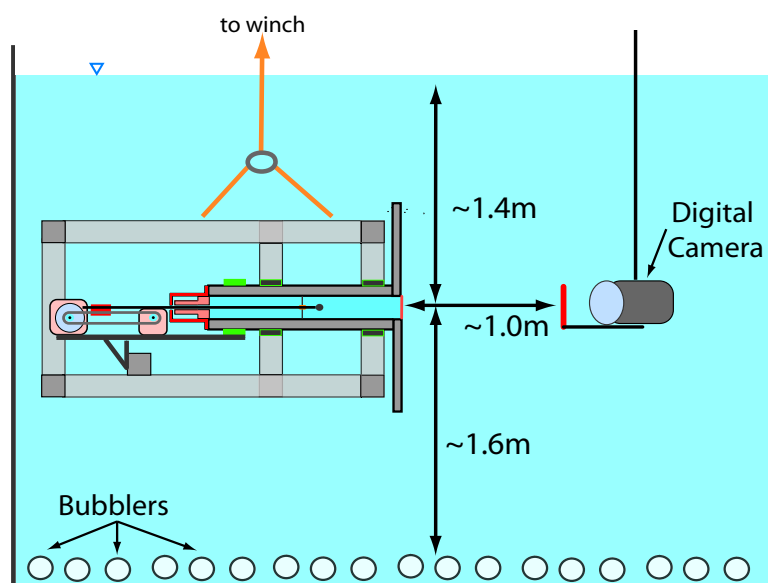
Figure 4.15: Side view of the experimental setup at the NRL bubble tank facility (not to scale).

4.3.1 Experimental procedure

Before submersion, the tube was aligned in the standard manner. After submersion many attempts were made to de-bubble the tube in the usual way. The tank water, however, was super-saturated with gas[2] and bubbles would form on all tube surfaces on about a two minute timescale. Coating the tube surfaces with wetting agents did nothing to stop the

---

[2]Water was added to the tank about an hour before the tube was submerged. This was done to raise the water level in the tank, making the tube easier to access from the platforms above the tank. Easy access to the tube is essential for easy de-bubbling. However, in another ironic twist of fate, adding the water to the tank made de-bubbling much more difficult as we suspect that this water, coming from a high-pressure source, was super-saturated with air.
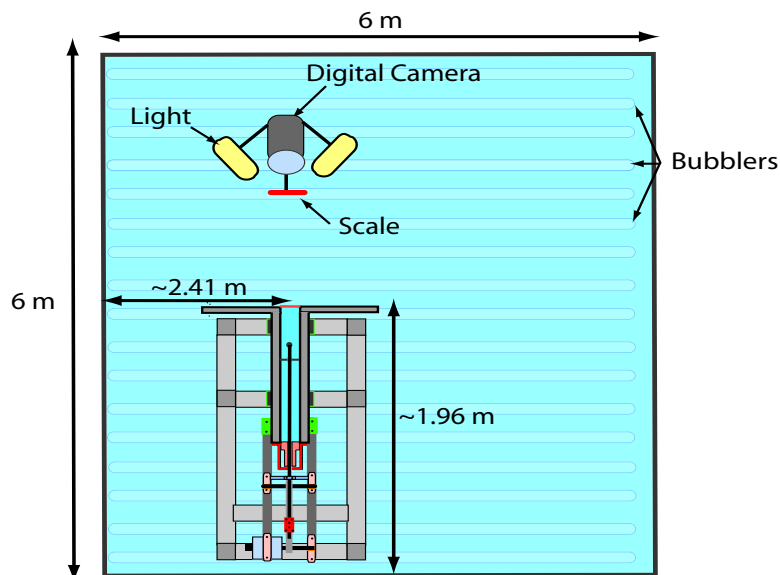
Figure 4.16: Top view of the experimental setup at the NRL bubble tank facility (not to scale).

diffusion-driven bubble formation, but did make the bubbles somewhat easier to remove. A number of novel approaches to de-bubbling were attempted, including flushing the tube with gravity-feed flow of degassed water. After eight hours hunched over the tube on a very uncomfortable platform, we resigned ourselves to let the tube sit in the tank overnight with the hopes that the system would reach an equilibrium state.

Bubbles were still forming in the tube on the second day, but at a much slower rate. The tube was reassembled underwater and then oriented vertically, with the tube opening pointing up. The tube was again flushed with degassed water from a gravity feed. When no new bubble formation was observed after ten minutes, we crossed our fingers, attached the HDPE window and positioned the tube, oriented horizontally, as shown in Figures 4.15 and 4.16.

The system was instrumented as described in Section 3.3.4 (including the impedance matchbox), with the exception of the charge converter. The relatively shallow deployment depth allowed the hydrophone cable to reach a platform above the water level and be plugged directly into a Brüel and Kjær Nexus conditioning charge amplifier. The Nexus, a very low-noise instrument with selectable gain and filtering, was set to provide 316 mV/kPa with 100 Hz to 100 kHz band-pass filtering. This about three times the gain provided by the previous charge convertor, hopefully reducing the relative amount of electromagnetic noise as the signal is carried along the 30 m coaxial cable from the Nexus directly to the VSA.

Measurements were made of the sound speed in the tube and of the reflection coefficient at the tube opening with the bubble production mechanism turned off. The sound speed measurements showed excellent agreement with elastic tube theory. The reflection coefficients measurements were similar to those measured at Dodge Pond and in the large wooden tank. These measurements suggest that our de-bubbling efforts were successful.

After the preliminary measurements, the bubblers were turned on. Bubble production was controlled by adjusting a pressure regulator on the final plenum before the manifold. The flow control valves were adjusted until relatively similar flow rates feed each bubbler. Both the pressure and air flow rate were recorded. Measurements were made at line pressures of 9.0, 8.0, 7.0, 6.0, 5.8, 5.6, 5.4, 5.2 and 5.0 psi. The lowest value is just above the hydrostatic pressure in the tank at bubbler depth. At each pressure, the complex reflection coefficient was measured in the usual manner.

4.3.2   Bubble distributions

An accurate measurement of the bubble population is imperative when making comparisons to theory. Thirty second clips of digital video recordings of the bubble population were recorded at each pressure level. The digital camera was set at about one meter from the tube opening (so as not to interfere with the measurements). Between 2 and 5 frames from the 30 seconds were selected for post processing.

The camera records images of bubbles that pass in between the camera lens and a white screen. The screen is illuminated by two underwater lights and has a machinist's scale fixed to it. A sample frame is shown in Figure 4.17. The machinist's scale provides the needed reference for determining bubble size. Each image is calibrated using this scale, providing a calibration constant, ℓ_{ref}, the number of image pixels per unit length. The bubbles, as visible in the sample frame, are not perfect spheres. As rising bubbles are distorted along in the direction of gravity, the bubbles are assumed to be spheroids, symmetric around the axis of gravity. Measurements of both the horizontal (Δx) and vertical (Δy) axis lengths (in pixels), as shown in Figure 4.18, are required to determine the bubble volume,

$$V = \frac{4}{3}\pi \left(\frac{\ell_{ref}\Delta x}{2}\right)^2 \left(\frac{\ell_{ref}\Delta y}{2}\right). \tag{4.4}$$

The measured diameters can be related to an effective radius, a, for a spherical bubble of the same volume,

$$a = \ell_{ref} \sqrt[3]{\left(\frac{\Delta x}{2}\right)^2 \left(\frac{\Delta y}{2}\right)}. \tag{4.5}$$
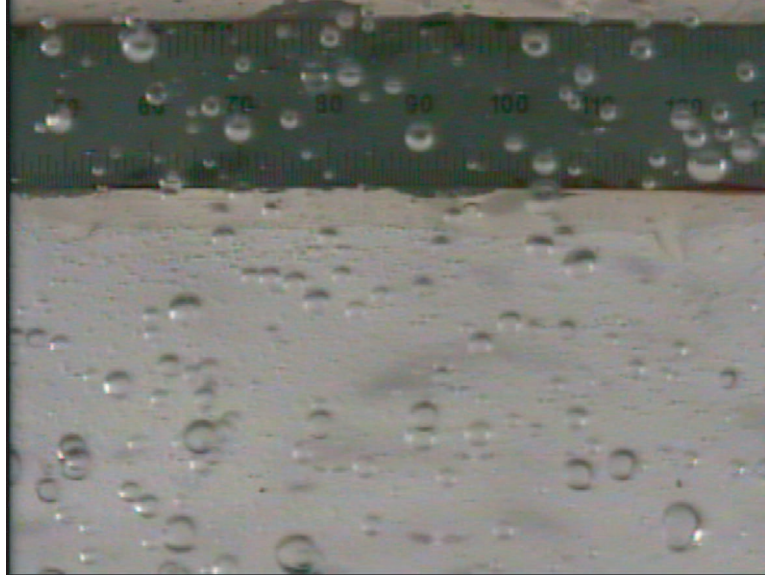
Figure 4.17: Sample frame of video captured by the underwater digital camera for a supply pressure of 9.0 psi. The machinist's scale is visible at the top, perhaps appearing as a dark band in poor reproductions of the figure.
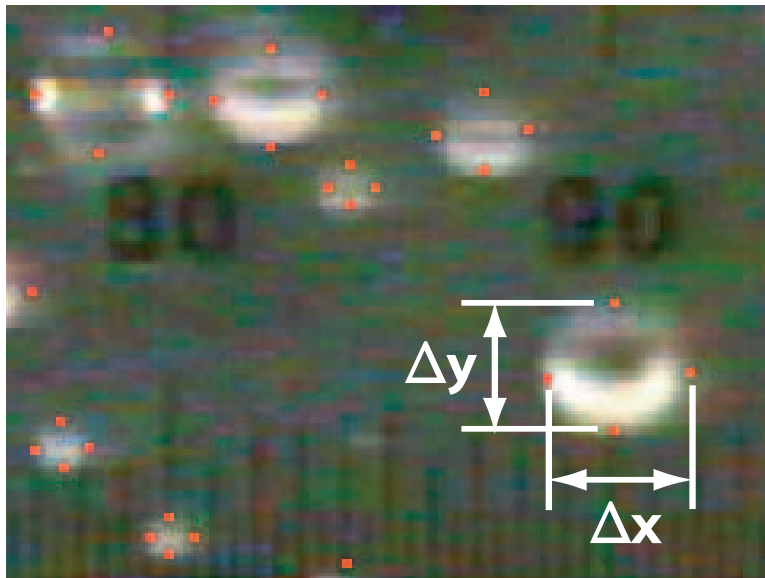
Figure 4.18: Blow-up of the sample video frame. The the horizontal (Δx) and vertical (Δy) axis lengths are labelled.

124

Corrections for camera artifact

The bubble size distributions must also be corrected for the view of the underwater camera. Bubbles just in front of the camera will appear larger than those just in front of background screen. The correction procedure is simple but not necessarily straightforward. As shown in Figure 4.19, the volume captured by the camera is roughly the frustum of a square pyramid. This volume is divided into a finite number, N, of volume bins of equal thickness, h. The bin closest to the screen is defined to be bin 1 and that closest to the camera lens is bin N. The volume, V_n, of each bin, also modelled as the frustum of a pyramid, is given by

$$V_n = \frac{1}{3}h\left(A_t + A_b + \sqrt{A_t A_b}\right)$$ (4.6)

where A_t is the area of the "top" of the pyramid (facing the lens) and A_b is the area "base" (facing the screen).

All measured bubble radii in bin n, $a_{bin,n}$, must be corrected by a factor specific to that bin, C_n:

$$a_{bin,n} = \frac{a_{meas}}{C_n}.$$ (4.7)

The correction factor varies linearly with bin number:

$$C_n = 1 + m\left(\frac{n - \frac{1}{2}}{N}\right)$$ (4.8)

where n is the volume bin number, N is the total number of bins and

$$m = \frac{1}{2}\left(\frac{X}{x} + \frac{Y}{y}\right) - 1$$ (4.9)

is the slope of the correction factor. Here X, Y, x and y are the widths and heights of the white screen and camera lens, respectively (see Figure 4.19).
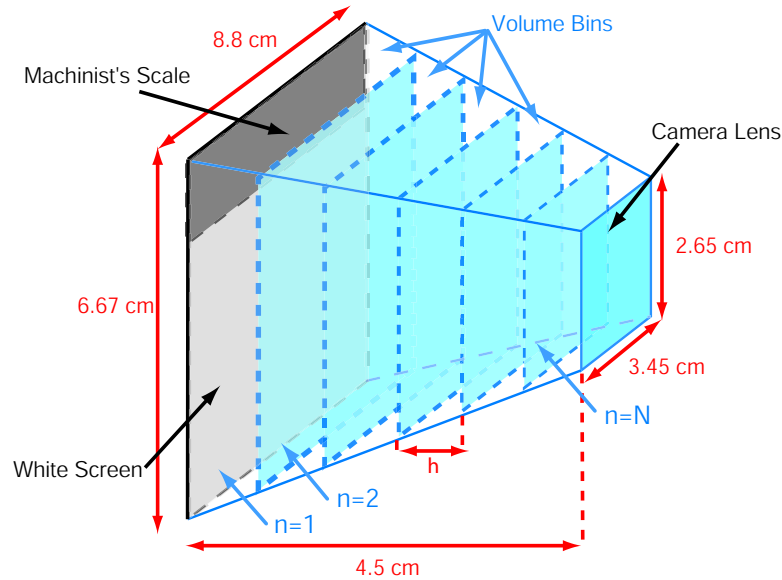
Figure 4.19: Dimensioned illustration of the camera setup (not to scale). The volume of bubble water photographed by the camera is divided into a finite number of bins to correct for camera artifacts.

If the bubbles captured by the camera are assumed to be randomly scattered throughout the entire volume, then the proportion of the total number of bubbles in each volume bin is equal to the volume of that bin relative to the total volume. That is to say if the volume of bin n is V_n, then the proportion of bubbles in that bin (relative to the total number of bubbles in the video frame) is V_n/V_T, where V_T is the total volume. Those bubbles in the volume bin closest to the camera lens (bin N) require the most correction. But this bin also has the smallest volume, so the fewest amount of bubbles require the most correction. Likewise, those bubbles in the largest bin (bin 1, closest to the screen) require the least correction.

This process results in a bubble size distribution that is somewhat sensitive to bin size. Ideally, the bins should be of vanishingly small thickness, but this would require an infinite

number of bubble measurements. In practice, the bin size was adjusted until there was little observable change if the number of bins was increased or decreased by one. Typically between 10 and 15 bins were used. Figure 4.20 shows the result of this correction procedure on one of the measured distributions. The corrected bubble size distribution (bottom frame) shows a clear shift towards smaller sizes from the raw bubble distribution (top frame).
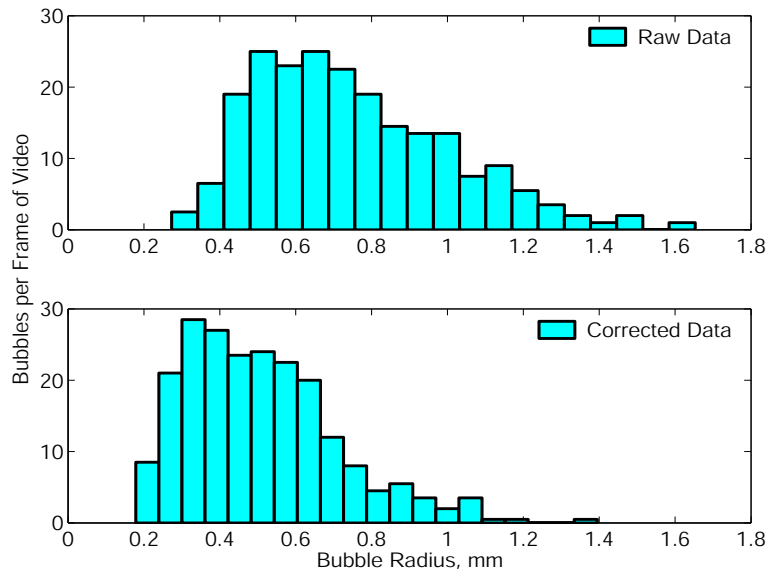
Figure 4.20: Histogram of the raw measured bubble size distribution (top) compared against the same distribution corrected for camera artifact (bottom) for the 6.0 psi case. There is a clear shift towards smaller bubble sizes.

Bubble distribution fitting

Once the bubble size distribution has been corrected for the camera view, the measured bubble radii are fit to a standard distribution to ease post-processing. This work follows the fitting procedure described in [1], except a modified log-normal distribution is used here. Fitting is achieved by comparing the cumulative density function (CDF), $D(a)$, of the

measured distribution to that of the model distribution. The cumulative density function
is the probability that any given radius in the distribution is smaller than the input size
$(0 \leq D(a) \leq 1)$. The CDF of the measured distribution is

$$D_{meas}(a) = \frac{\bar{n}(a)}{N},$$ (4.10)

where $\bar{n}(a)$ is the number of measured bubble radii $\leq a$ and N is the total number of
bubbles in the distribution matrix. The measured CDF is compared against the model
CDF, given by

$$D_{model}(a) = \int_{a_{min}}^{a} \wp(\xi) \, d\xi,$$ (4.11)

where $\wp(a)$ is the probability density function (see Section 2.2.2). As mentioned above, a
modified log-normal distribution of the form

$$\wp(a) \propto \exp\left(-b\left(\ln\left(\frac{a}{a_0}\right)\right)^2\right)$$

was used. This modified distribution is not normalized in a standard manner[3] and the CDF
had to be modified to force it to span the range $0 \leq D_{model} \leq 1$ by taking

$$D_{model}(a) \rightarrow \frac{D_{model}(a)}{D_{model}(a_{max})}.$$ (4.12)

---

[3]The standard log-normal distribution takes the form

$$\wp(\xi) = \frac{\sqrt{b}}{\xi\sqrt{\pi}} \exp\left(-b\left(\ln(\xi)\right)^2\right)$$

which is normalized such that

$$\int_0^\infty \wp(\xi) \, d\xi = 1.$$

We found that distributions with the radius term in the denominator preceding the exponent did not fit the
data as well as those without.

The model CDF was fit to the measured CDF using a least-squares fit, minimizing the R^2 parameter,

$$R^2 = \sum_{a_i=a_{min}}^{a_{max}} \left(D_{meas}\left(a_i\right) - D_{model}\left(a_i\right) \right)^2 , \tag{4.13}$$

in two dimensions varying the values of a_0 and b. This fitting procedure usually resulted in very good fits to the data. A typical result is shown in Figure 4.21.
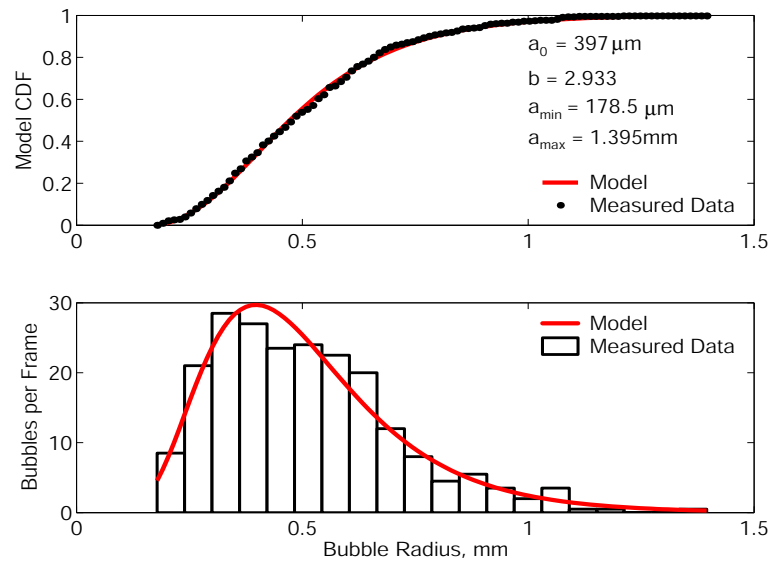
Figure 4.21: The measured cumulative density function is compared with that of the model distribution fit to the data (top frame) for the 6 psi case. The fitting parameters for the truncated, modified log-normal distribution are listed. The bottom frame shows a histogram of the measured bubble distribution compared with the best-fit probability density function.

Void fraction estimates

If every bubble in an integer number of frames is counted, the void fraction can be estimated. As mentioned above, the sample captured by the digital camera can be modelled as the frustum of a square pyramid, with a total volume, V_T given by Eq. (4.6) (see Figure 4.19

129

for dimensions). The void fraction, β, is simply the sum of the measured bubble volumes divided by the total volume of the video frame,

$$\beta = \frac{1}{nV_T} \sum_j \frac{4}{3}\pi a_j^3, \tag{4.14}$$

where n is the number of video frames analyzed. Void fraction estimations by this method have been shown, in past experiments performed at the facility, to be in good agreement with samples taken directly from the bubbly liquid in tank. The samples were collected by simultaneously sealing the top and bottom of a vertically-oriented cylinder as bubbles rose through it. The void fraction is the volume of air trapped in the cylinder divided by the total volume.

Uncertainties in bubble distribution measurements

The bubble sizing process is subject to a number of uncertainties, the most prominent being the actual measurement of the bubble size. As seen in Figure 4.18, it is difficult to distinguish the exact pixel that defines the bubble wall. The measurements of Δx and Δy generally had an uncertainty estimated to be about 3 pixels, corresponding to an average uncertainty in effective spherical radius of $\pm 16.6\%$. The uncertainty in bubble size also manifests itself as an uncertainty of $+56/-40\%$ in void fraction. The uncertainty in bubble size could be reduced if the camera had a higher optical zoom; fewer bubbles would be imaged per frame, but each would occupy more pixels. This would, however, make the void fraction estimates, which require a large bubble sample in a known volume, even more unreliable.

4.3.3 Experimental results and analysis

Due to time constraints in analyzing the bubble distributions, comparisons were only made at three pressures: 6.0, 7.0 and 9.0 psi. Comparisons are also limited to the measured and theoretical complex reflection coefficients (no attempt was made to back out the phase speed and attenuation of the bubbly liquid). For the measured bubble distributions and void fractions there was little difference in the theoretical predictions using the two different bubble models discussed in Sections 2.2.2 and 2.2.3, most likely because the distributions were generally very broad. Comparison was therefore limited to the model championed by Commander and Prosperetti, Eq. (2.74).

Measurements of the complex reflection coefficient for the 6.0, 7.0 and 9.0 psi cases are shown in Figures 4.22, 4.23 and 4.24, respectively. At these pressures the void fractions were estimated by Eq. (4.14) to be 0.133, 0.196 and 0.532%. As evident in the plots, the measurements leave much to be desired. Not only does the data have considerable structure (it is not smooth), which will be discussed later, but the measurements are very far off from the theoretical predictions, plotted as solid lines on the figures. Possible explanations for the disagreement between the measurements and the model come in two varieties - measurement problems (i.e., bubbles) and/or model inaccuracies, specifically our model of the the tube opening. Figure 4.25 is a plot of theoretical phase speed and attenuation for the measured bubble distributions.

Measurement problems, such as bubbles forming in and/or entering the tube are a very real possibility, especially given the problems encountered while de-bubbling. Experience
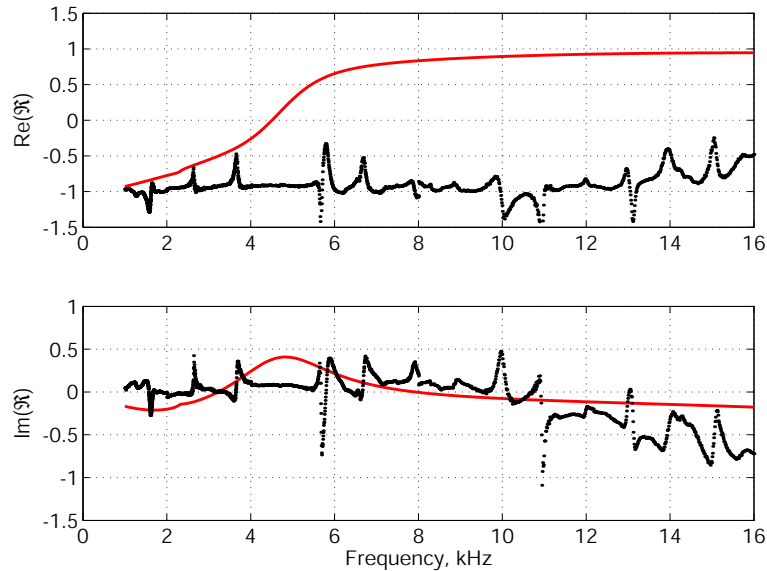
Figure 4.22: The real and imaginary parts of the measured reflection coefficient are compared with the theoretical value using the bubble distribution of Figure 4.21 for the 6.0 psi case. The void fraction was estimated to be 0.133%

has shown that a single bubble rarely influences the data over the entire frequency range. It would take a number of bubbles inside the tube to account for the degree of awfulness seen here. The tube was checked for bubbles at the end of the experiments, and a few bubbles were visible just behind the HDPE window. These bubbles could have entered the tube in two ways. The bubbles may have slipped behind the window during experiments, in which case they would have always been located right at the water/bubbly liquid interface, limiting any adverse effects on the measurements. However, the bubbles may have formed inside the tube during the experiment and moved up to the tube opening as the tube was raised for inspection. If this were the case, the bubbles would have seriously corrupted the measurements and could explain the poor agreement.

There is also a strong possibility that the baffled tube model developed in Chapter
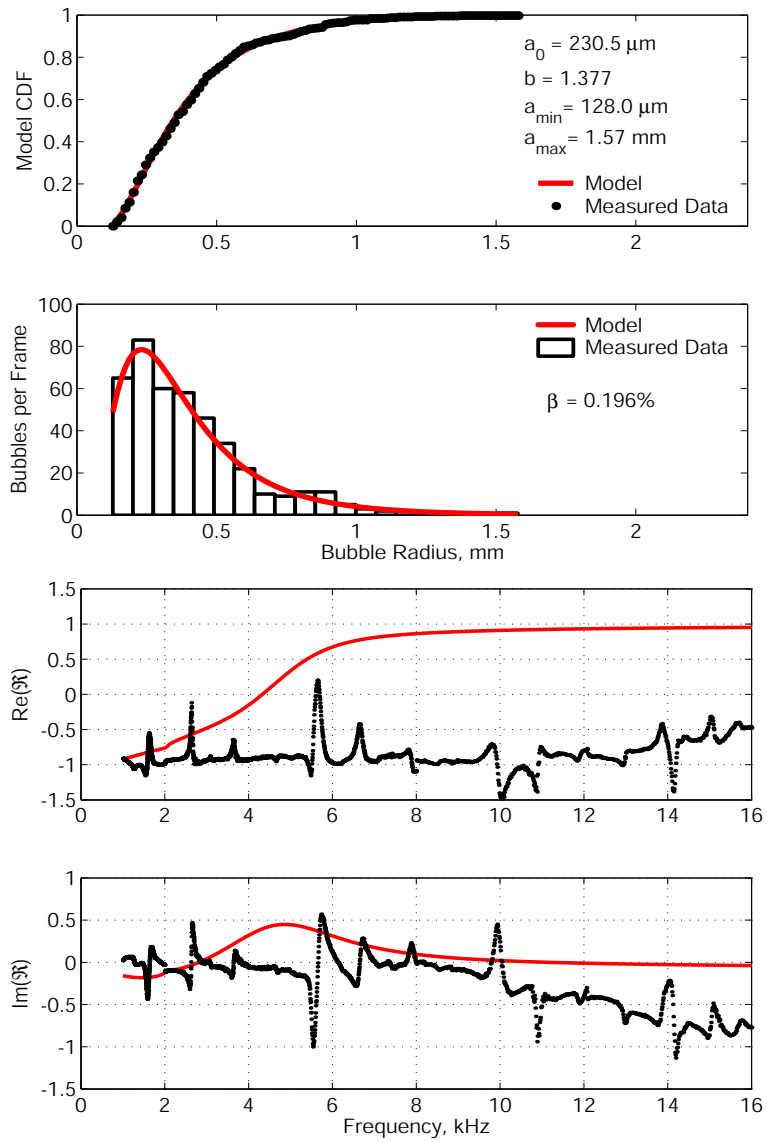
Figure 4.23: The measured and modelled CDF (top frame) and PDF (second from top) for the 7.0 psi case. The void fraction was estimated to be 0.196%. The real and imaginary parts of the measured and theoretical reflection coefficients are shown in the bottom two plots.
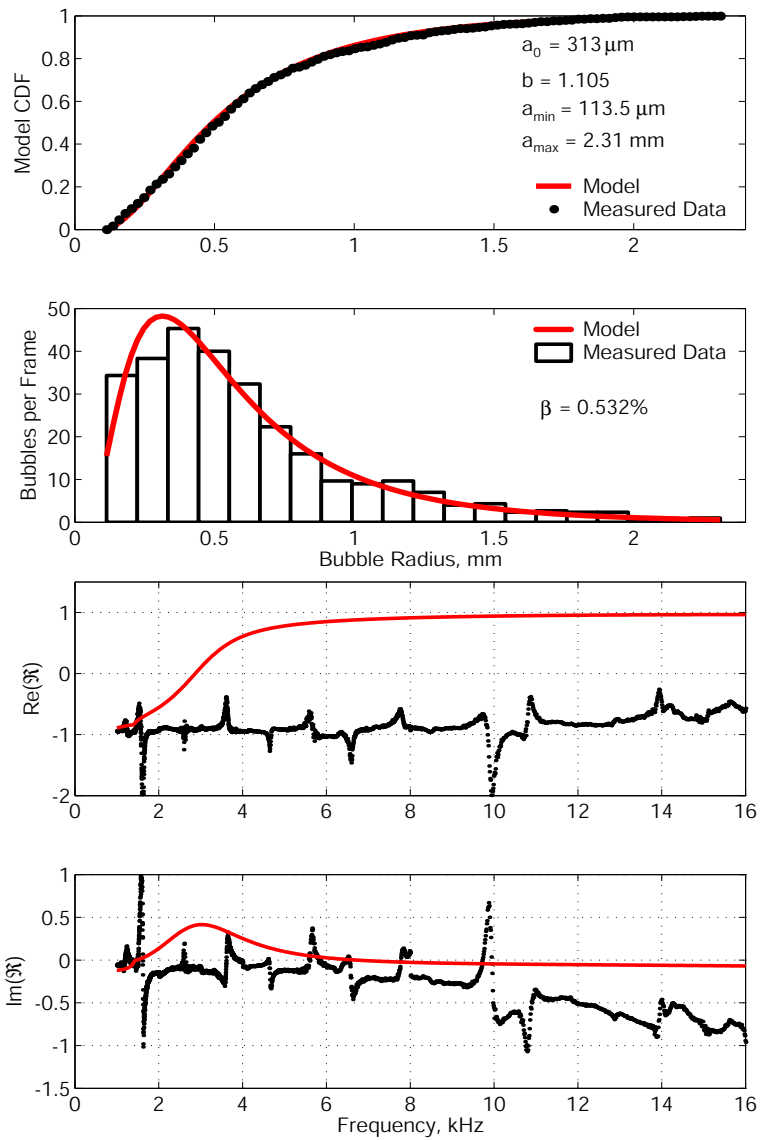
Figure 4.24: The measured and modelled CDF (top frame) and PDF (second from top) for the 9.0 psi case. The void fraction was estimated to be 0.532%. The real and imaginary parts of the measured and theoretical reflection coefficients are shown in the bottom two plots.
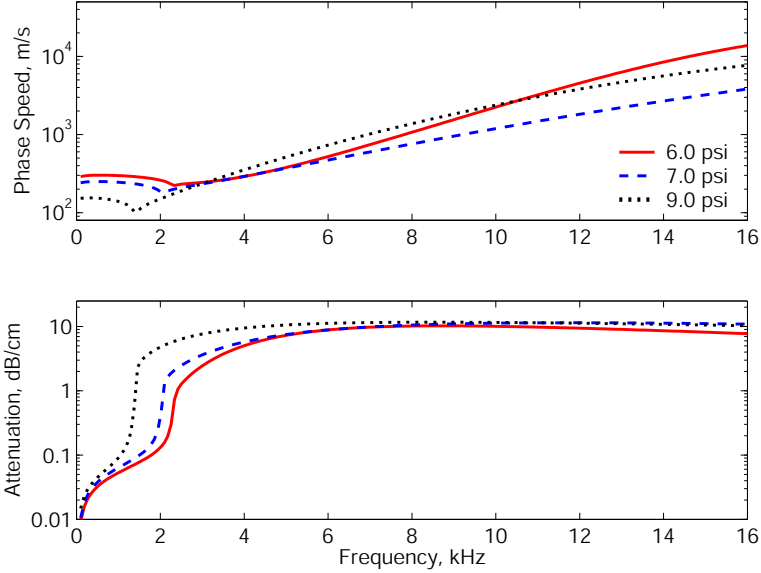
Figure 4.25: The predicted phase speed and attenuation for the measured bubble distributions at experimental pressures.

2 may have been compromised in these experiments. To investigate this possibility, the measurements were also compared against the other theoretical limit - the unbaffled tube opening discussed in Section 2.1.7. Figures 4.26 and 4.27 compare the measured complex reflection coefficient against both the baffled and unflanged theoretical predictions for water inside the tube and the measured bubbly distribution outside for the 7.0 and 9.0 psi cases. Eq. (2.51) was used to correct the unflanged theory for the two-fluid case. The unflanged prediction matches the data much better than the baffled case, especially at the higher frequencies. Of course the real system lies between these two theoretical extremes, but these calculations suggest that it behaves more like an unflanged tube than a tube fitted with an infinite rigid baffle.

Assuming the data are not corrupt, there are two possible mechanisms that could explain

the better fit with the unflanged case. The first is that the high phase speed in the bubbly liquid is on the order of that of steel for the highest frequencies (see Figure 4.25). This would make the baffle appear acoustically transparent and would easily explain the observations. However, for frequencies below 10 kHz, the phase speeds on are on the order of water or lower where we have already verified that the baffle behaves close to rigid. The other, more probable, explanation is that the attenuation is so high, predicted to be on the order of 10 dB/cm for all frequencies above about 3 kHz, that the sound field is not in communication with the baffle but rather the tube appears as if it is radiating into an infinite space. As the bubbly liquid interface is strongly reflecting ($|\Re| \approx 1$), very little sound makes it past the HDPE window to begin with. With attenuation on the order of 10 dB/cm, the sound travels no more than one or two centimeters before it is attenuated to the noise level. Between 2 and 4 kHz, where the data do not show much agreement with either theory. It is at these frequencies where the sound speed and attenuation both begin to rise and the experiment is not accurately described by either theory. Perhaps this could be avoided if measurements were made without any baffle at all.

All the bubbly liquid measurements show periodic structure at approximately 1.0 kHz intervals, starting around 1.6 kHz. These frequencies happen to correspond to tube resonant frequencies, $\cos kL = 0$. The features can be explained by looking at another measurement made in the bubble tank. A limiting assumption behind the single-hydrophone TFM is that the sample being interrogated has acoustic properties which are fixed in time. The impedance at the tube opening must be exactly the same when the measurement is made
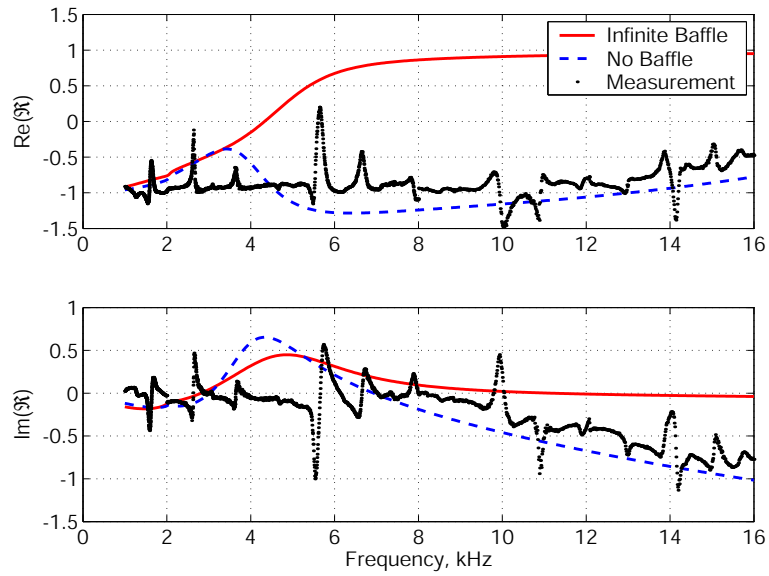
Figure 4.26: The measured complex reflection coefficient is compared with both the baffled and un-baffled theoretical predictions for the measured bubble distribution for the 7.0 psi case.
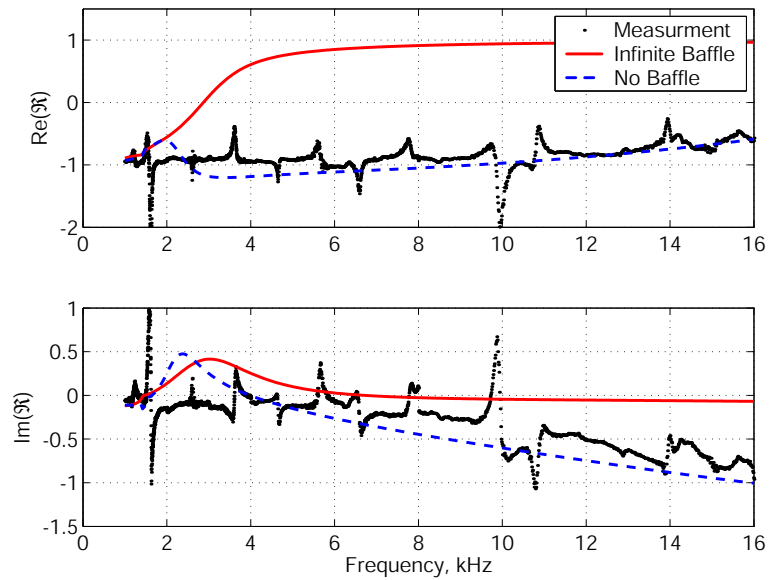
Figure 4.27: The measured complex reflection coefficient is compared with both the baffled and un-baffled theoretical predictions for the measured bubble distribution for the 9.0 psi case.

at point 1 as it was when the measurement was made at point 2. To investigate how stable the bubble population was with time, the pressure spectrum inside the tube was measured, without moving the hydrophone, at 30 second intervals for 5 minutes. This corresponds roughly to the measurement timing during an actual TFM run. The pressure spectrum inside the tube is a very strong function of the bubble population outside it. The measured pressure spectra are shown in the upper plot of Figure 4.28. There is no difference in the measurements except at the tube resonances, where there is always a slight variation in the peak value. The variance, a measurement of how different data sets are, of the seven spectra are shown in the bottom plot. There are clear peaks in the variance around the resonant frequencies. This measurement indicates that the bubble population is slightly unsteady in time and that this instability effects the pressure spectrum inside the tube most at tube resonance.

To investigate if an unstable bubble population could be the cause of periodic structure, a new sensitivity analysis was performed. The analysis was performed similar to the noise and uncertainty analysis in Section 3.6.2. To simplify the model, the simulated tube termination was assumed to be pressure-release, that is, $\Re = -1$. The simulation was used to create the "measured" complex transfer function at point 2. Before the "measurement" was made at point 1, the value of the reflection coefficient was changed to $\Re = -0.995$, simulating a slight change in impedance at the tube opening with time. The reflection coefficient was then calculated in the usual manner.

The simulation results are shown in Figure 4.29. The upper plot shows the "measured"
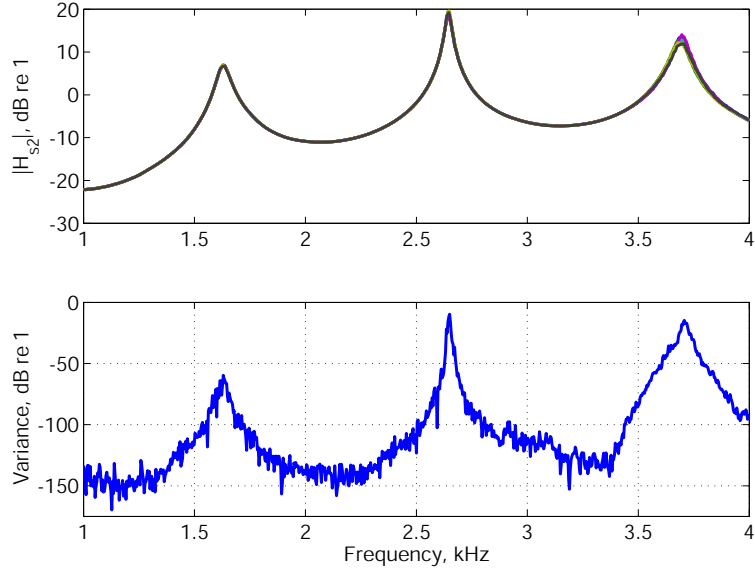
Figure 4.28: Magnitude of the measured pressure spectrum inside the tube at 30 sec intervals (upper plot) and the corresponding variance in the measurements (lower plot).

pressure spectrum at point 1 for both the $\Re = -1$ and $\Re = -0.995$ terminations. There is no discernable difference between the two at the scale shown, an indication of just how little change was added to the system. The effect on the magnitude and phase of the reflection coefficient, shown in the middle and lower plots, is very pronounced. We see a periodic artifact very similar to that observed in the bubble tank measurements, a clear indication that a time varying bubble is responsible. It is worth noting that away from tube resonance frequencies the simulated measurements are quite accurate. This is to be expected as the peak value of resonance is governed very strongly by the reflection coefficient (see Eq. (3.22)).
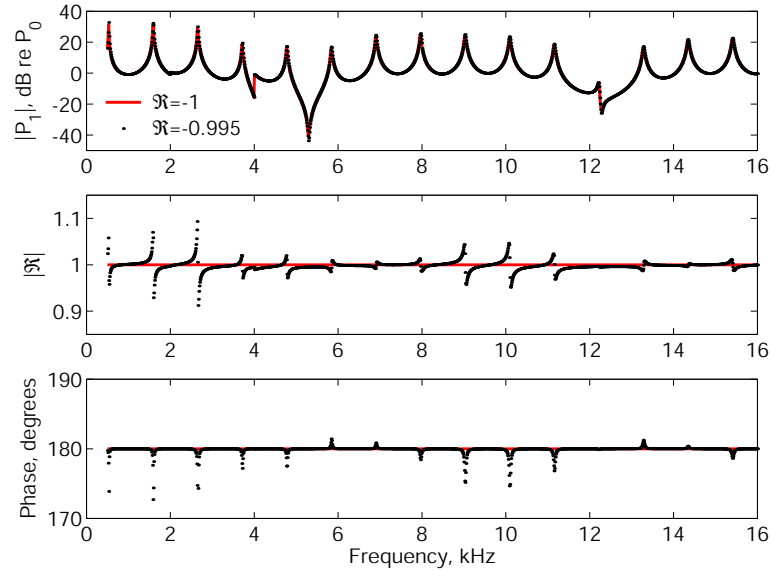
Figure 4.29: Numerical simulation of an impedance tube showing the effect of a slight change in $\Re$ between measurement points.

4.3.4 Recapitulation - Bubbly Liquids

While unsuccessful in accurately characterizing the bubbly liquids, these experiments brought to light a number of shortcomings that, once fixed, may significantly improve tube performance and ease of deployment. These shortcomings take many forms, including problems with the tube design, experimental conditions, and model inaccuracies.

Foremost, the difficulties de-bubbling the tube not only wasted a precious day of experiments, but revealed the most troublesome problem with the tube design: it must be flooded with its host fluid and de-bubbled on site. This not only limits the facilities where deployment is possible to those with access to the waterline, but leaves the system at the mercy of gassy water. A better design, discussed in more detail in the next chapter, is to seal the tube completely and fill it with a fluid that is not friendly to bubble formation.

140

Sealing the tube will also keep bubbles from entering the tube during experiments.

The bubble population was not perfectly stable in time. This was to be expected for a real bubble generation system, but its effect on the measurements was much more pronounced than anticipated. The single-hydrophone TFM, as we have shown, can only be applied to terminations that are *absolutely* stationary in time, rendering it completely impractical for the investigation of bubbly liquids. A two-sensor method must be employed in that case, presenting considerable calibration challenges. One possible solution is addressed in Chapter 6.

he measurements, assuming they are not otherwise corrupt, show much better agreement with an unflanged tube model than our flanged model. This suggests that the sound field is attenuated before ever interacting with the baffle. The purpose of the baffle was to better define the boundary conditioning in the tube opening plane. However, it appears that the baffle complicates the problem instead of simplifying it and may be responsible for the disagreement between the unflanged tube theory and the measurements in the 2-4 kHz range. The baffle should not be used in future bubbly liquid experiments.

These criticisms are not to say the tube developed here is without worth. We have very high expectations for measuring the acoustic propagation parameters of marine sediments and other media with lower attenuation and that do not change in time with the present tube system.

Chapter 5

A sealed, oil-filled impedance tube

The Dodge Pond experiments suggested, and the NRL experiments confirmed, that serious changes to the impedance tube design are necessary should it ever be suited for deployment in anything but a relatively controlled environment. Far too much time and effort are required for tube alignment, submerged assembly, and de-bubbling. The current procedure is also overly susceptible to problems caused by flooding it with less-than-ideal water, such as the super-saturated water encountered in the NRL experiments. The requirement that significant assembly be undertaken underwater also places a restriction on deployment locations and conditions.

All these issues are avoided if the tube is completely sealed with a well-characterized bubble-free liquid. This would eliminate the need for flooding and de-bubbling which would in turn greatly simplify the alignment process, tremendously simplifying and speeding up the deployment process. The process of sealing the tube completely free of air, as we will

see here, is relatively straightforward but time consuming but only needs to be performed once, or possibly a couple times a year.

This chapter will be divided into five short sections. The first covers the fill fluid selection process. Characterization of the physical properties of the fill fluid are discussed in the second section. The third explains modifications made to the original tube design to seal the fluid inside it. Experiments carried out to verify tube performance are detailed in the final two sections.

5.1 Fill fluid considerations

A number of different fill fluids were considered. The ideal fluid would be nonconducting, noncorrosive, and otherwise as inert as possible as well as environmentally friendly (should it ever leak out) but it should also repel water to keep it from entering the tube. The ideal fluid would also have a low viscosity, similar to water, and would effectively wet the walls of the tube to help keep from trapping bubbles. To maintain the full useable frequency range, the sound speed of the fluid should be close to that of water, ideally slightly higher (to push the first cutoff frequency up). The fluid must also have known (or measurable) temperature dependence on sound speed and viscosity.

Water itself was dismissed outright as being conducting, too prone to outgassing, and corrosive. Vegetable based oils, such as castor or soybean oil were contenders, as they have similar sound speeds and densities to water. They are also both very inexpensive, readily obtainable, nonconducting, chemically inert, and environmentally friendly. They

are, however, rather viscous and can absorb some water.

Petroleum based oils come in many different types, most of which tend to break down certain adhesives, plastics and rubbers, making them unacceptable for use. Some, however, are relatively stable and inert, such as mineral oil. Mineral oil is relatively inexpensive, has a similar sound speed to water, and comes in low viscosity varieties. Some mineral oils are also rated for contact with human food products, suggesting that they pose minimal environmental impact. Mineral oil is also a strong contender.

Silicone oils can have extremely low viscosities, displace water and easily wet most surfaces. Besides being nonconducting and noncorrosive, they do not attack most rubbers, plastics, or other silicones. The major drawback is that silicone fluids, such as Dow Corning 200 series fluids or DOT 5 brake fluids, are highly compressible and have sound speeds on the order of 900 m/s. Use of a silicone fluid, although otherwise desirable, would cut the useable frequency range of our tube almost in half. Other possibilities included a number of synthetic oils and glycol based fluids, such as DOT 3 or 4 brake fluids (which have remarkably high sound speeds). Most of these failed either or both of the chemically inert and environmentally friendly requirements.

After much debate, a low viscosity food-grade mineral oil, STE Oil Company's Crystal Plus 70 FG, was chosen as the fill fluid. Like most mineral oils, 70 FG is colorless, odorless, and tasteless. The material safety data sheet (MSDS) for the oil states that although not recommended for direct human consumption, no adverse effects have ever been documented as a result of ingestion. The only danger posed by the oil is that it is slightly flammable in

vapor form.

5.2 Fill fluid characterization

It was necessary to characterize certain physical properties of the oil before use. The most critical properties are the density and sound speed which play important roles in waveguide propagation and in the TFM. The viscosity was also measured, as it is the dominant dissipative mechanism inside the tube. As with water, the density, sound speed, and viscosity of mineral oil are functions of temperature. This section details the measurements made to characterize these quantities.

The density of the mineral oil was measured by pipetting a known volume of oil onto a milligram balance. The density was measured to be 814 ± 3 kg/m^3 and was independent, within the measurement uncertainty, of temperature between -5 and 25 degrees Celsius.

The sound speed was measured using two 2.0 MHz transducers and a pulser-receiver. The pulser triggers a 200 MHz digital storage oscilloscope at the same time it sends a pulse to the transmit transducer. The arrival time of the pulse at the second transducer is measured on the oscilloscope and recorded. With the measured separation distance between the transducer it is straightforward to calculate the sound speed. This method assumes, of course, that the sound speed is not dispersive (frequency dependent). The sound speed measurements, taken between 8 and 26 degrees Celsius, are plotted on Figure 5.1. The sound speed decreases with increasing temperature, which is common for oils [77]. The

data were fit to a a second-degree polynomial in temperature,

$$c\left(T\right) = c_2 T^2 + c_1 T + c_0, \tag{5.1}$$

which can be used to extrapolate the data to slightly higher or lower temperatures. For our measurements, the best fit constants were $(c_0, c_1, c_2) = (1479.6, -3.0699, -0.02737)$ for c in meters per second and T in degrees Celsius. The absolute uncertainty in the measured sound speed is estimated to be about ± 5 m/s based on the uncertainty in the measured separation distance and arrival time.
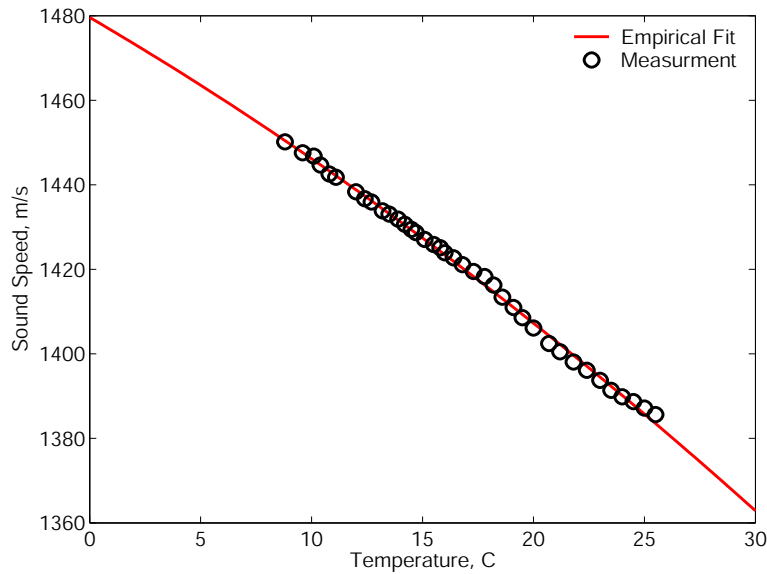
Figure 5.1: Measured sound speed of mineral oil (open circles) as a function of temperature compared with a second degree polynomial empirical fit (solid line).

The viscosity was measured with a Cannon LV2000 digital viscometer between 0 and 30 degrees Celsius. The viscosity measurements, in centipoise, are plotted in Figure 5.2. The viscosity of liquids can be fit to the form [78]

$$\mu = A 10^{\frac{B}{T-C}} \tag{5.2}$$

146

where T is the absolute temperature. For our measurements, the best fit constants were $(A, B, C) = (0.333, 202, 183)$ for μ in centipoise and T in Kelvin.
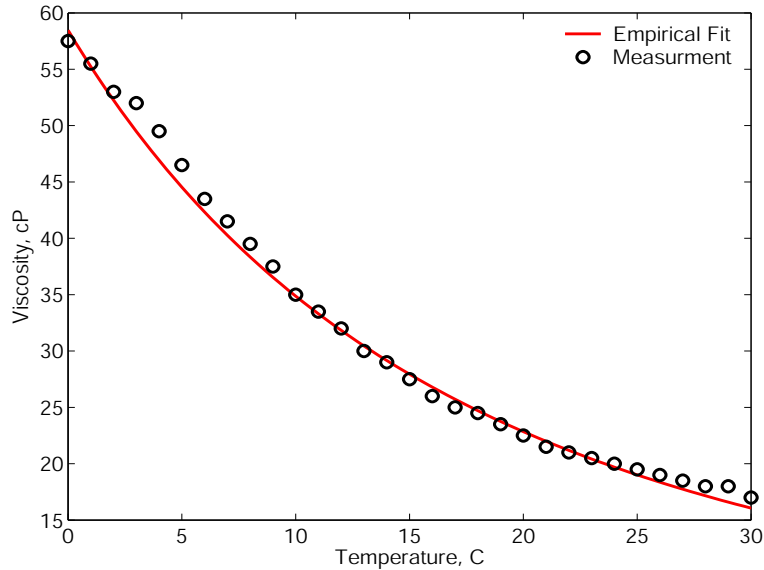
Figure 5.2: Measured viscosity of mineral oil (open circles) as a function of temperature compared with an empirical fit (solid line).

5.3 Design modifications

The necessary design modifications were straightforward and are shown in Figure 5.3. The tube needed to be sealed at both ends - the baffled opening and the rear of the sound source. The tube opening was sealed by semi-permanently fixing the silicone rubber window (see Section 3.3.3) to the baffle with a silicone rubber sealant. The silicone sealant bonds extremely well to the silicone window and fairly well to stainless steel baffle. Immediately after the window was glued to the baffle, all air bubbles trapped in the sealant were rolled out with a heavy steel rolling pin. All excess silicone sealant was removed from the inner

diameter of the baffle with a small putty knife.
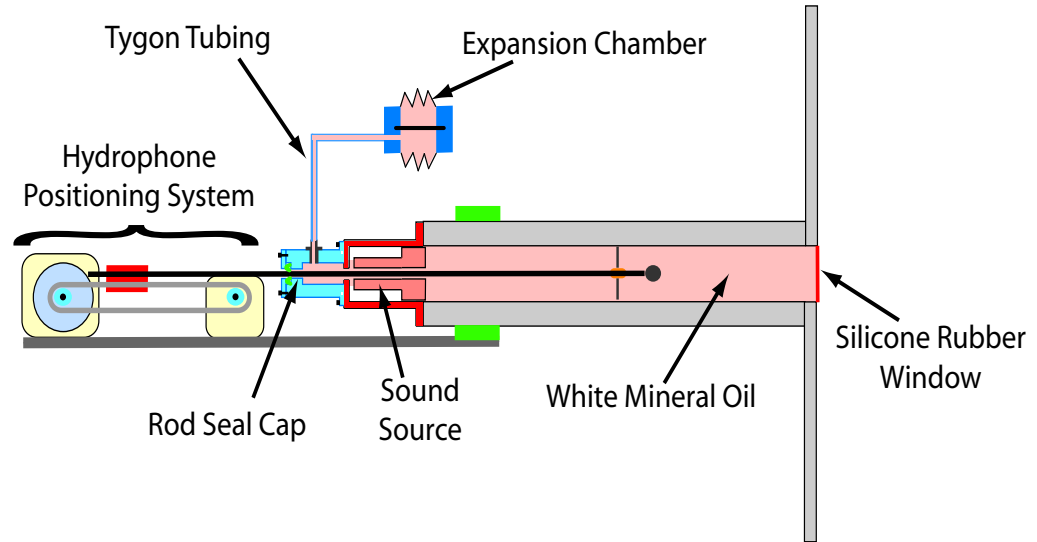
Figure 5.3: Overview of the oil-filled impedance tube system (not to scale).

The source end of the tube was sealed with a solid nylon cap, illustrated in Figure 5.4. This cap serves two main purposes. The first is that allows for linear motion of the hydrophone sheath while maintaining a seal to prevent oil leakage. This is accomplished with a standard rubber 1/4 inch hydraulic rod seal. The second is that it aligns the hydrophone sheath with the axis of the source, helping to keep the hydrophone in the center of the tube. A section of Tygon tubing attached to a barbed fitting on the side of the cap allows the oil in the tube to communicate with an expansion chamber. The expansion chamber, nothing more than a sealed neoprene-latex bellows, is necessary to account for the fluid volume displaced by the hydrophone sheath as it moves from one position to another inside the tube.

The hydrophone sheath was also redesigned and rebuilt. The Teflon insert shown in
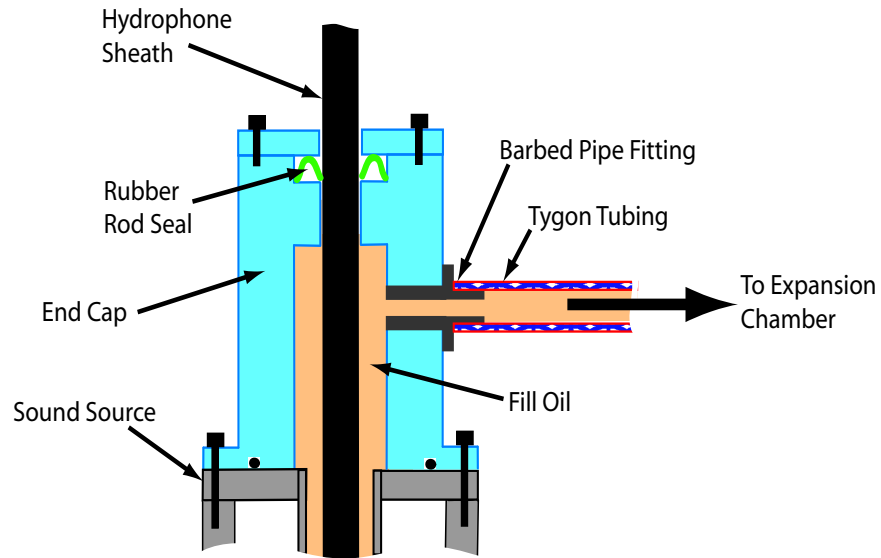
Figure 5.4: The rod seal cap mounts on the end of the sound source and seals against the hydrophone sheath to prevent oil leaking out of the system (not to scale).

Figure 3.8 was replaced with a stainless steel piece that the narrower sheath section threads into. This was done to alleviate problems encountered with the Teflon outgassing and bending during the previous experiments. The far end of the sheath must also be sealed to keep oil from leaking out. A liquid tight cord-grip fitting (Hummel CF07AR-BR) seals against the hydrophone cable, as shown in Figure 5.5. This fitting mates with a female NPT to barbed tube fitting. A length of 1/4 inch inner diameter Tygon tubing connects the hydrophone sheath to the barbed fitting. The tubing allows for some strain relief and keeps the fitting assembly from interfering with the timing belt. The fitting assembly travels with the tubing inside a section of aluminum pipe which serves to support the weight of the fittings and helps keep the system aligned. The pipe is secured to the aluminum frame that surrounds the entire tube assembly with two stainless steel pipe clamps.

149
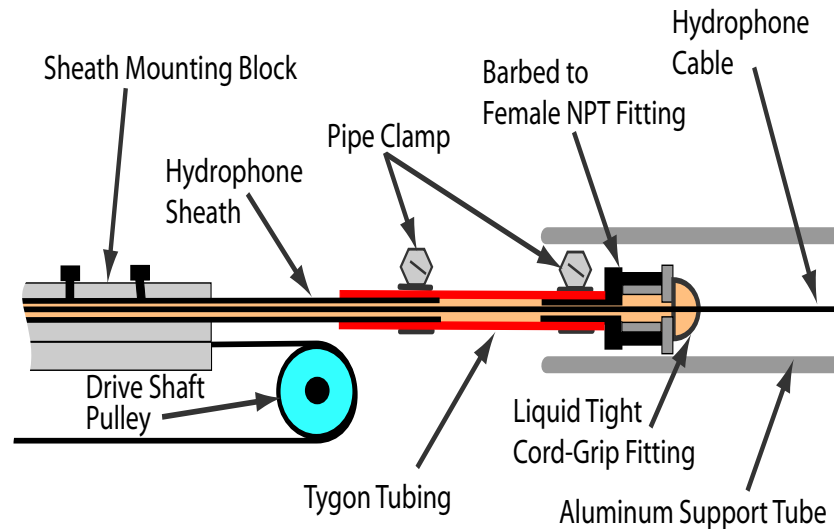
Figure 5.5: The far end of the hydrophone sheath is fitted with a length of tygon tubing. A liquid-tight cord grip fitting mounted on a barbed NPT fitting attaches to the tubing and seals the oil inside. The entire assembly rides inside a length of aluminum pipe to support the weight of the fittings (not to scale).

Filling the tube with oil was a time consuming and messy process. The major steps will be briefly outlined here. Before use, the mineral was degassed under a vacuum to remove any dissolved air (and keep bubbles from forming). The tube was filled with oil with the baffled opening facing down, supported by high-density styrofoam. All system components, such as the hydrophone sheath, centering star, sound source, and the source end cap described above were assembled while submerged in oil. Special attention was paid to make sure all o-ring grooves and o-rings were properly wetted with oil before assembly.

5.4   Verification of the oil-filled tube

As with the water filled tube, a number of experiments were made to confirm that the oil-filled tube behaves as modelled. All measurements were made with the tube oriented upside

down. The tube opening was supported by two layers of 5 cm thick styrofoam. Because styrofoam is soft and porous it behaves almost as pressure-release compared to water (or oil). For these experiments the pressure inside the tube was assumed to be given by Eq. (3.15).

The first measurement was of the phase speed inside the tube. Measurements were made using the standard two-point cross correlation procedure. The measured phase speeds are plotted in Figure 5.6. The measurements are compared with the theoretical prediction of the elastic tube theory discussed in Section 3.2 using the measured density and intrinsic sound speed of the oil. There is excellent agreement between the measurements and the theory.
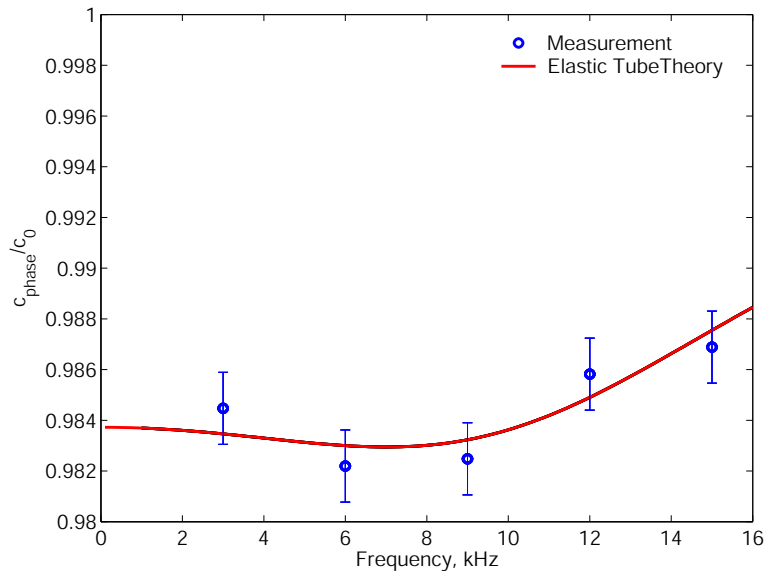
Figure 5.6: Measured phase speed in the mineral oil-filled tube as a function of frequency compared with elastic tube theory.

The standing wave pattern in the tube was measured at five different frequencies. Mea-

surements were made at around 5 mm intervals over a 20 cm section of the tube. For this experiment the tube was excited with a continuous wave of constant frequency and the amplitude of the hydrophone signal was measured on a digital oscilloscope. The measurements are compared with the theoretical prediction in Figure 5.7. As with the phase speed measurement, there is very good to excellent agreement at all frequencies between the measurements and the theory.
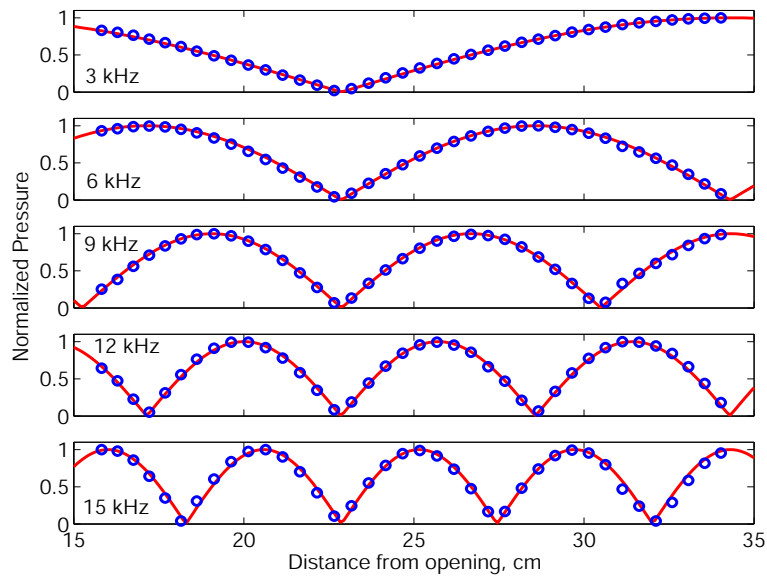
Figure 5.7: Normalized pressure as a function of position inside the oil-filled tube for 5 different driving frequencies (open circles) compared with the theoretical prediction prediction for a sound-soft termination (solid lines).

The impedance of an oil-filled transmission line, terminated by the styrofoam, was also measured. As we assumed that the styrofoam acts as if sound soft, the theoretical impedance of the oil transmission line is given by (3.17). The measured impedance is compared with the theoretical result in Figure 5.8. There is good agreement between the two except for slight "blips" around 5.4, 9.4 and 14 kHz. These may be artifacts caused by the styrofoam

termination, which we know to be imperfect.
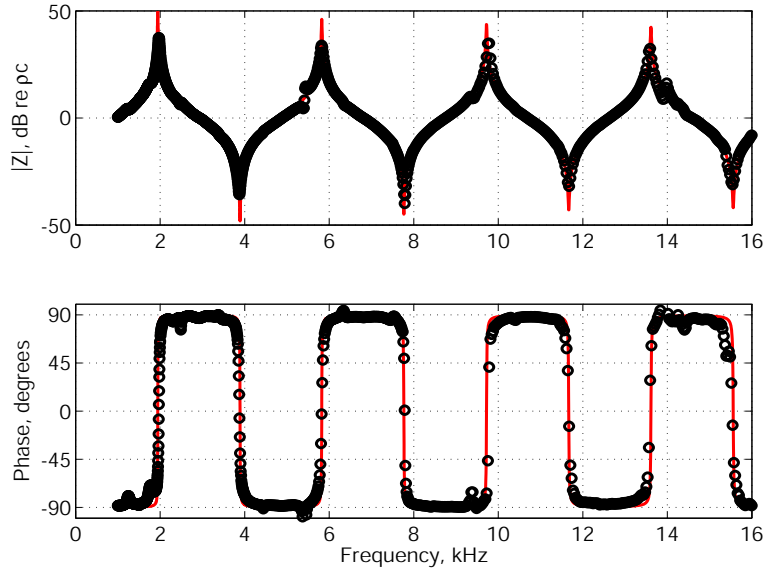
Figure 5.8: Measured magnitude and phase of a styrofoam-terminated 17.8 cm oil-filled transmission line (open circles) compared with the theoretical prediction for a sound-soft terminated transmission line (solid line).

5.5   Reflection from the baffled opening

The oil filled tube was lowered into our laboratory's large wooden water-filled tank, discussed in Section 4.1.3. The reflection coefficient and impedance at the tube opening were measured. The measurements, compared with the theoretical prediction of Eq. (2.47), are shown in Figures 5.9 and 5.10. With mineral oil inside the tube and water outside the ratio of specific impedances is about $\gamma \approx 0.774$. The agreement between the measurements and the theory at all frequencies is as good, and often better, than observed with the water-filled tube in the same tank. These measurements serve to demonstrate the feasibility of what

153

may be the next generation liquid-filled impedance tube.
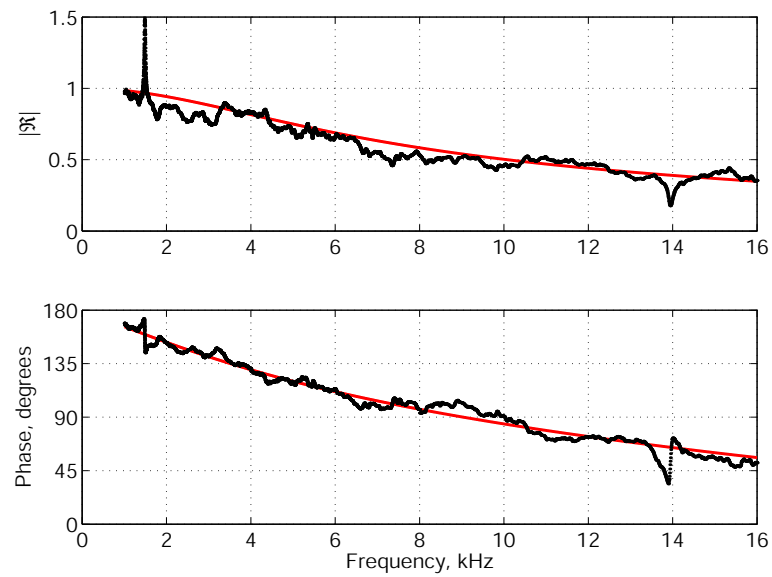
Figure 5.9: Measured magnitude and phase of the reflection coefficient of the oil-filled tube radiating into a large water-filled tank (dots) compared with the theoretical prediction of Eq. (2.47).

154
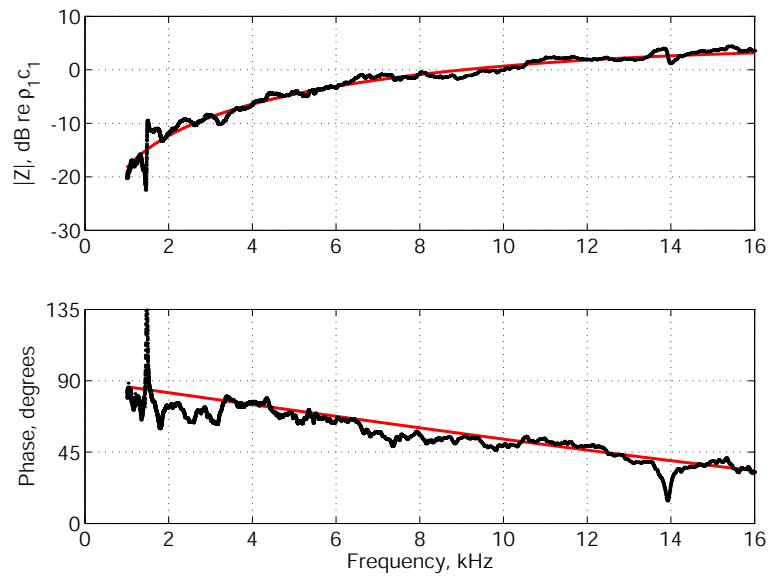
Figure 5.10: Measured magnitude and phase of the impedance at the opening of the oil-filled tube radiating into a large water-filled tank (dots) compared with the theoretical prediction.

Chapter 6

Recapitulation and Future Work

This Chapter summarizes the major results obtained developing and testing an impedance tube for in situ deployment in an marine environment. Possible solutions for most of the difficulties and problems encountered in this work are provided, as are a number of suggestions for future system improvements, adaptations, and measurements.

6.1 The water-filled baffled impedance tube

A submersible, baffled, thick-walled, water-filled impedance tube capable of remote deployment in up to 20 m of water has been developed. The impedance tube uses a single hydrophone transfer function method to measure the complex reflection coefficient at the tube opening. Development of the tube required significant engineering design to accommodate submersion and to adapt the scanned hydrophone approach for use in a water-filled tube. It has a usable frequency range of 1 - 16 kHz and requires no calibration, both

156

significant improvements over previous water-filled impedance tube systems.

The reflection coefficient measured with the tube submerged in a large body of water agrees favorably with classical theory for a baffled tube opening. This may be the first measurement of its type made in water and serves as a validation of the impedance tube's performance.

6.2   Bubbly liquid experiments

The bubbly liquid experiments at the NRL Salt Water Tank Facility were of limited success. The most useful outcome of the experiments, as is often the case with experiments run for the first time, was that they brought to light a number of design faults that needed to be addressed. These issues include de-bubbling difficulties, sensitivity to unstable bubble populations, and an inaccurate model of the tube opening. The first two issues are addressed in the next section, the latter is discussed here.

The bubbly liquid experiments showed that the baffled tube opening is poorly suited for bubbly liquid measurements. An unflanged tube of decreasing wall thickness at the opening may be able to be more accurately modelled as even with the baffle in place, the measurements agreed well with the unflanged model, except in the 2-4 kHz range where the individual bubbles were beginning to resonate. The unflanged model, however, requires significantly more computing time than the baffled model, and a supercomputer may be necessary should an attempt be made to determine phase speed and attenuation from a numerical inversion.

6.3 Future impedance tube work

The bubbly liquid experiments also revealed that the single hydrophone transfer function method fails when measuring fluids whose properties are not perfectly stable in time. If a submersible impedance tube is ever to be used for in situ bubble characterization a two hydrophone method must be employed. Two sensor methods present considerable calibration and frequency range limitations. One promising solution addressing both is to use a hybrid system with a single wall-mounted hydrophone in combination with a scanned hydrophone similar to the one used in this work. To calibrate the two hydrophones, the scanned hydrophone is positioned at exactly the same location as the acoustic center of the wall-mounted hydrophone and the transfer function between the two measured. This transfer function can be used a calibration factor between the two hydrophones. An attempt to employ this method was undertaken in the laboratory, but current belt and pulley positioning system was incapable of the fine adjustments required to properly align the two hydrophones for calibration. A different positioning system, perhaps one using a lead screw, would be required.

In Chapter 5 we demonstrated the feasibility of a sealed, oil-filled impedance tube. Sealing the tube eliminates the need for on-site alignment and assembly, dramatically reducing the time required for preparation and field deployment. It also assures a bubble-free tube. Future liquid-filled impedance tubes should unquestionably be sealed. Although very few problems were encountered with the mineral used here, more research into fill fluids may yield one better-suited for use in an impedance tube (i.e. one with a higher sound speed).

The silicone rubber window did deform somewhat during the experiments, suggesting that a stiffer window or better expansion chamber may be in order. Ideally, the entire positioning system would be enclosed and filled with oil, eliminating the need for an expansion chamber to accommodate displacement of the hydrophone sheath .

Although modifications need to be made before the impedance tube can be used for measurements of bubbly liquids, it is almost certainly suited, in its present (oil-filled) form, for in situ measurements of ocean-bottom sediments. In this case, the baffle would be required to support the tube on top of the sediment. The theoretical phase speeds of water-saturated sediments are much closer to water and exhibit much less dispersion than bubbly liquids. This is important as impedance tubes generally work best when measuring fluids of similar specific impedance. The theoretical attenuation in saturated sediments is also significantly less than that in bubbly liquids, suggesting that their may be fewer difficulties modelling the tube opening as baffled.

Eventually, a numerical routine to determine the phase speed and attenuation from the measured reflection coefficient would be desirable. This would require a very well defined model of the tube opening, but would bring the impedance tube full circle as a measurement device.

Appendix A

Derivation of the Wood-Mallock Equation

Wood derived his 1930 result, Eq. (1.5), for the sound speed in a two-fluid mixture by assuming the mixture may treated as homogenous with an effective density and compressibility governed by the relative volumes of the two fluids. Although this is an acceptable and accurate approximation, it was given without proof. The following is a more rigorous derivation using a control mass approach[*].

Consider the control mass shown in Figure A.1a. The mass initially occupies a volume, V_0, that is comprised of two fluids with different densities and sound speeds. We define a void fraction, β, as

$$\beta = \frac{V_2}{V_0} \tag{A.1}$$

---

[*]Although I wish I could claim to be smart enough to have derived this myself, I owe this particular derivation to a lecture given by Professor Allan D. Pierce at Boston University on January 22, 2004.

where V_2 is the volume of the second fluid and V_0 is the total volume. It is noted that:

$$1 - \beta = \frac{V_1}{V_0} \tag{A.2}$$

as $V_1 + V_2 = V_0$. The density of the mixture, ρ_m, is given by the total mass divided by the total volume:

$$\rho_m = \frac{\rho_1 \left(1 - \beta\right) V_0 + \rho_2 \beta V_0}{V_0} = \rho_1 \left(1 - \beta\right) + \rho_2 \beta. \tag{A.3}$$
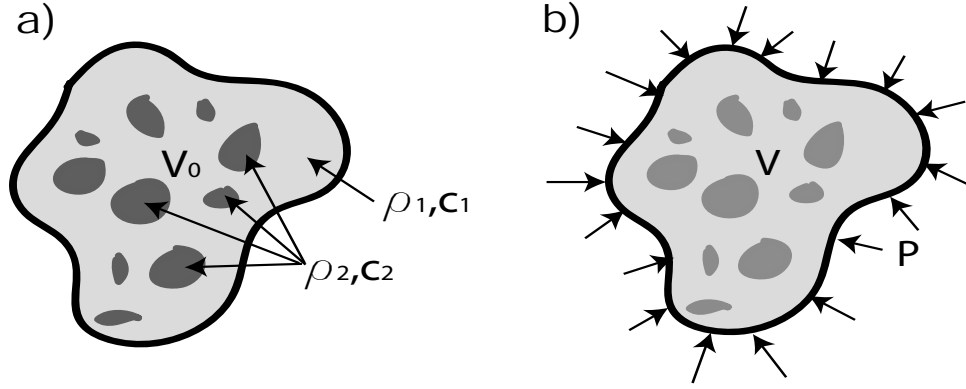
Figure A.1: a) Control mass; b) Deformation under pressure

The pressure, P, acting on the control mass, initially P_0, is then perturbed such that $P \rightarrow P_0 + \Delta P$. The pressure perturbation causes changes in the individual densities and volumes of the two components:

$$\begin{aligned}
\rho_1 &\rightarrow \rho_{1,0} + (\Delta\rho)_1 ; & \rho_2 &\rightarrow \rho_{2,0} + (\Delta\rho)_2 \\
V_1 &\rightarrow \left(1 - \beta\right) V_0 + (\Delta V)_1 ; & V_2 &\rightarrow \beta V_0 + (\Delta V)_2
\end{aligned} \tag{A.4}$$

as well as on the effective mixture:

$$\begin{aligned}
V &\rightarrow V_0 + \Delta V \\
\rho_m &\rightarrow \rho_{m,o} + (\Delta\rho)_m
\end{aligned} \tag{A.5}$$

161

where $\Delta V = (\Delta V)_1 + (\Delta V)_2$. In these equations a subscript 0 refers to the density in the initial, unperturbed state. For the control mass, the mass must remain unchanged between initial and perturbed states:

$$(V_0 + \Delta V)(\rho_{m,0} + (\Delta \rho)_m) = V_0 \rho_{m,0}.. \tag{A.6}$$

Imposing that all perturbations be small, we can neglect the $\Delta V (\Delta \rho)_m$ term, leaving us with

$$(\Delta \rho)_m = \frac{-\rho_{m,0}}{V_0} \Delta V = \frac{-\rho_{m,0}}{V_0} ((\Delta V)_1 + (\Delta V)_1). \tag{A.7}$$

As the mass of each constituent fluid must remain constant, we can write

$$\begin{aligned} (\Delta V)_1 &= (1-\beta) V_0 \left(\frac{-(\Delta \rho)_1}{\rho_{1,0}} \right) \\ (\Delta V)_2 &= \beta V_0 \left(\frac{-(\Delta \rho)_2}{\rho_{2,0}} \right) \end{aligned} \tag{A.8}$$

Substituting Eqs. (A.8) and (A.3) into Eq. (A.7) and dividing by ΔP we have

$$\frac{(\Delta \rho)_m}{\Delta P} = ((1-\beta)\rho_{1,0} + \beta \rho_{2,0}) \left((1-\beta) \frac{1}{\rho_{1,0}} \frac{(\Delta \rho)_1}{\Delta P} + \beta \frac{1}{\rho_{2,0}} \frac{(\Delta \rho)_2}{\Delta P} \right). \tag{A.9}$$

Dropping the 0 subscripts and noting that the speed of sound, c, is given by $c^{-2} = \Delta \rho / \Delta P$, the equation for the sound speed in the mixture is:

$$\frac{1}{c_m^2} = \frac{(1-\beta)^2}{c_1^2} + \frac{\beta^2}{c_2^2} + \beta(1-\beta) \frac{\rho_1^2 c_1^2 + \rho_2^2 c_2^2}{\rho_1 \rho_2 c_1^2 c_2^2} \tag{A.10}$$

which is equivalent to the result given in Section 1.2.

Appendix B

Green's Function Solution to the

Helmholtz Equation

A Green's function for the Helmholtz equation is a solution for G to:

$$\nabla^2 G\left(x,y,z|x_0,y_0,z_0\right) + k^2 G\left(x,y,z|x_0,y_0,z_0\right) = -4\pi\delta\left(x-x_0\right)\delta\left(y-y_0\right)\delta\left(z-z_0\right)$$

where δ is the Dirac delta function. In vector notation, the equation is:

$$\nabla^2 G\left(\vec{r}|\vec{r_0}\right) + k^2 G\left(\vec{r}|\vec{r_0}\right) = -4\pi\delta\left(\vec{r}-\vec{r_0}\right) \tag{B.1}$$

The velocity potential in the region of interest, assuming no sound sources lie in the region, is a solution to the homogeneous Helmholtz Equation:

$$\nabla^2\phi\left(\vec{r}\right) + k^2\phi\left(\vec{r}\right) = 0. \tag{B.2}$$

The first step in the Green's function approach is to multiply Eq. (B.1) by $\phi(\vec{r})$ and Eq. (B.2) by $-G(\vec{r}|\vec{r_0})$:

$$\phi(\vec{r})\nabla^2 G(\vec{r}|\vec{r_0}) + k^2 \phi(\vec{r}) G(\vec{r}|\vec{r_0}) = -4\pi\phi(\vec{r})\delta(\vec{r} - \vec{r_0})$$

$$-G(\vec{r}|\vec{r_0})\nabla^2\phi(\vec{r}) - G(\vec{r}|\vec{r_0})k^2\phi(\vec{r}) = 0$$

and then add the two equations:

$$\phi(\vec{r})\nabla^2 G(\vec{r}|\vec{r_0}) - G(\vec{r}|\vec{r_0})\nabla^2\phi(\vec{r}) = -4\pi\phi(\vec{r})\delta(\vec{r} - \vec{r_0}). \qquad (B.3)$$

The trick to the approach is to switch the $\vec{r}$ and $\vec{r_0}$ vectors (this does not violate either Eqs. (B.1) or (B.2)) and integrate both sides over the region of interest, V_0, (such that the volume includes the vector $\vec{r}$):

$$\iiint\limits_{V_0} \phi(\vec{r_0})\nabla_0^2 G(\vec{r}|\vec{r_0}) - G(\vec{r}|\vec{r_0})\nabla_0^2\phi(\vec{r_0})\, dV_0 = \iiint\limits_{V_0} -4\pi\phi(\vec{r_0})\delta(\vec{r} - \vec{r_0})\, dV_0. \quad (B.4)$$

Green's theorem is used to change the left-hand side of Eq. (B.4) from a volume integral to a surface integral:

$$\iiint\limits_{V_0} \phi\nabla_0^2 G - G\nabla_0^2\phi\, dV_0 = \iint\limits_{S_0} \phi\frac{\partial}{\partial n_0}G - G\frac{\partial}{\partial n_0}\phi\, dS_0$$

where S_0 is the surface that bounds V_0 and $\partial/\partial n_0$ is the outward normal derivative to this surface. The right-hand side of Eq. (B.4) can be simplified using the following property of the Dirac delta function:

$$\iiint\limits_{V_0} \phi(\vec{r_0})\delta(\vec{r} - \vec{r_0})\, dV_0 = \begin{cases} \phi(\vec{r}) & \vec{r} \in V_0 \\ \\ 0 & \vec{r} \notin V_0 \end{cases}$$

Eq. (B.4) can now be written:

$$\phi(\vec{r}) = \frac{-1}{4\pi}\iint\limits_{S_0} \phi(\vec{r_0})\frac{\partial}{\partial n_0}G(\vec{r}|\vec{r_0}) - G(\vec{r}|\vec{r_0})\frac{\partial}{\partial n_0}\phi(\vec{r_0})\, dS_0. \qquad (B.5)$$

This is an interesting result – if the properties of the acoustic field on any closed surface are known, the acoustic field anywhere inside the bounded volume can be determined! The general solution of (B.1) for the Green's function is [46]:

$$G\left(\vec{r}\,|\vec{r_0}\right) = \frac{e^{ik|\vec{r}-\vec{r_0}|}}{|\vec{r}-\vec{r_0}|}.$$

(B.6)

This is the same solution one obtains for the pressure field at $\vec{r}$ from a point monopole source located at $\vec{r_0}$.

To solve Eq. (B.5) for the region shown in Figure 2.6, the following condition on G must be satisfied:

$$\frac{\partial}{\partial n_0}G\left(\vec{r}\,|\vec{r_0}\right)\Big|_{z_0=0} = 0.$$

(B.7)

Using the method of images, the normal slope on the loci of points (say, $\vec{r_0}$ and $\vec{r_0}'$) equidistant from two monopoles oscillating in phase will be zero. More specifically, if $\vec{r_0} = (x_0, y_0, z_0)$ and $\vec{r_0}' = (x_0, y_0, -z_0)$ then the normal slope at the plane defined by $z_0 = 0$ will be zero, as required above. Using the principle of superposition, the Green's function satisfying Eq. (B.7) is:

$$G\left(\vec{r}\,|\vec{r_0}\right) = \frac{e^{ik|\vec{r}-\vec{r_0}|}}{|\vec{r}-\vec{r_0}|} + \frac{e^{ik|\vec{r}-\vec{r_0}'|}}{|\vec{r}-\vec{r_0}'|}.$$

(B.8)

Setting $z_0 = 0$ as required by Eq. (2.23), the Green's function of choice is:

$$G\left(\vec{r}\,|\vec{r_0}\right) = \frac{2e^{ik|\vec{r}-\vec{r_0}|}}{|\vec{r}-\vec{r_0}|}$$

(B.9)

where $\vec{r_0} = (x_0, y_0, 0)$.

Appendix C

Reflection from a Baffled Tube Opening

Equation (2.46) predicts the plane wave reflection coefficient for a sound-hard tube fitted with an infinite, sound-hard flange at its opening. It is similar to, if not exactly the same as, solutions given in [41, 40, 45, 46, 47] which were all obtained using similar assumptions (namely neglecting higher-order terms in Eq. (2.26)). The validity of this result will be evaluated by further comparison against another, more rigorously derived, published result and a numerical (finite element) model.

Norris and Sheng [39] published a solution for the primary reflection coefficient from a baffled tube opening in terms of the coefficients of the higher order terms. Their solution (using our notation) is given by:

$$\Re\left(kb\right) = -1 + \frac{2}{M_{00}}\left(\eta_{00} - \sum_{n=1}^{\infty}\eta_{n0}\frac{k_{zn}}{2k}B_n\right) \tag{C.1}$$

where:

$$\eta_{nn}(kb) = \beta_n^{(1)}(kb) + \alpha_{1n}^2 \beta_n^{(2)}(kb)$$

$$\eta_{nm}(kb) = \frac{\alpha_{1n}^2 \beta_n^{(1)}(kb) - \alpha_{1m}^2 \beta_m^{(1)}(kb)}{\alpha_{1n}^2 - \alpha_{1m}^2}$$

$$\beta_n^{(q)}(x) = i \int_0^x \frac{2 J_1^2(s) s\, ds}{(x^2 - s^2)^{1/2} (s^2 - \alpha_{1n}^2)^q} + \int_x^\infty \frac{2 J_1^2(s) s\, ds}{(s^2 - x^2)^{1/2} (s^2 - \alpha_{1n}^2)^q} \qquad \text{(C.2)}$$

$$M_{00}(kb) = \eta_{00}(kb) + \frac{i}{kb}$$

Needless to say, this system of equations is not pleasant to solve, and the B_n terms must be determined numerically. They do, however, provide a rational function approximation for the reflection coefficient, valid for $0 < kb < 3.8$, in the form of:

$$\Re(kb) = -|\Re| e^{i2kL} \qquad \text{(C.3)}$$

where:

$$|\Re| = \frac{1 + \alpha kb + \beta(kb)^2}{1 + \alpha kb + (1+\beta)(kb)^2}$$

$$(\alpha, \beta) = (0.323, -0.077) \qquad \text{(C.4)}$$

$$\frac{L(kb)}{b} = \frac{0.82159 - 0.49(kb)^2}{1 - 0.46(kb)^3}$$

Figure C.1 compares the magnitude and phase of the complex reflection coefficient predicted by the equation developed in Section 2.1.6, Eq.(2.46), and that published by Norris and Sheng (C.3). The functions are plotted over the range $0 < kb < 1.6$, which corresponds roughly to 0 to 16 kHz in our water-filled impedance tube. The two curves are nearly indistinguishable in magnitude and very similar in phase, an indication that the higher order terms play little role at these values of kb. No corrections are given by Norris and Sheng should the fluids inside and outside the tube be different.

A second comparison made was against a numerical model constructed using the finite element method (FEM). The exact details of this method will not be discussed here. A
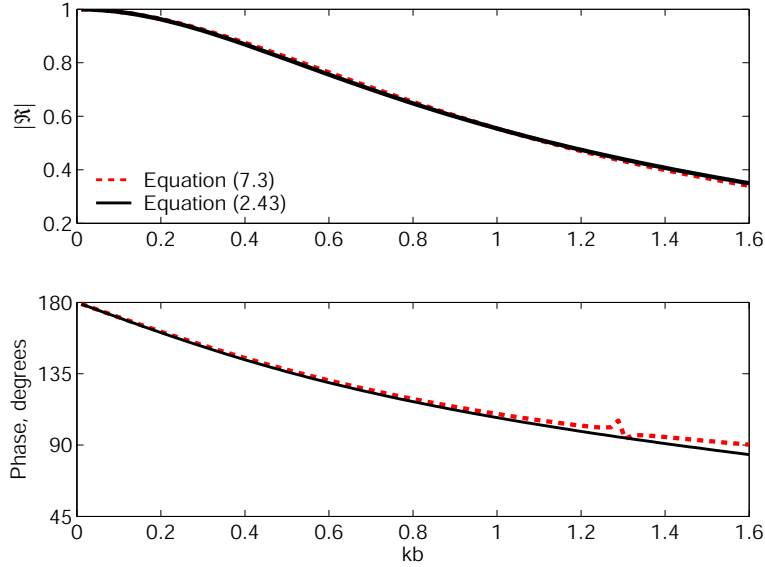
Figure C.1: Comparison of the magnitude and phase of the complex reflection coefficient as predicted by Eq. (2.46) and Eq.(C.3)

commercial FEM package, FEMLab (COMSOL Inc., Burlington, MA), was used to solve the Helmholtz pressure equation for a geometry and set of boundary conditions matching our problem. Figure C.2 shows a sample pressure field result and labels the boundary conditions used in the model. These boundary conditions will be discussed first.

Because it is impossible to create a numerical model that extends to infinity as required to model a tube fitted with an infinite baffle, radiation boundary conditions ($\partial p/\partial n + ikP = 0$) (also called non-reflecting or absorbing boundary conditions) were placed on the appropriate boundaries as an approximation. These boundary conditions are imperfect and the resulting solution is sensitive to the model size. Therefore, two different sizes were used for the region outside the tube. Neumann boundary conditions ($\partial p/\partial n = 0$) were used on all rigid surfaces, as well as on the axis of symmetry. A simple Dirichlet boundary condition
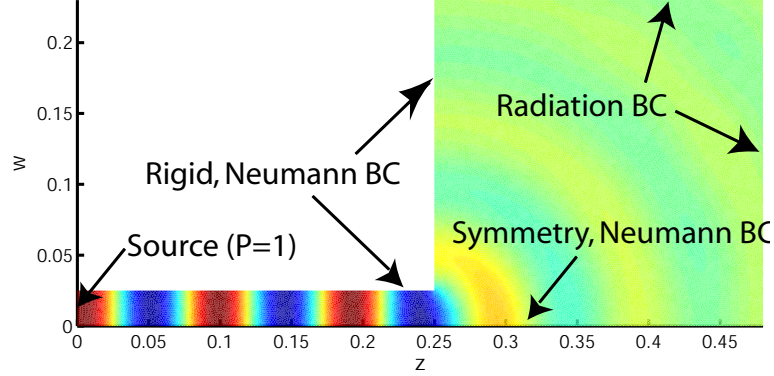
Figure C.2: Boundary conditions overlayed on a sample pressure amplitude field calculated using the FEM model

$(p = 1)$ was used to provide a sound "source" at $z = 0$ in the model.

The impedance was determined by dividing the pressure by its gradient at the tube opening:

$$Z_n = i\omega\rho\frac{1}{b}\int_0^b \frac{P}{\frac{\partial P}{\partial z}}\,dw \tag{C.5}$$

The line integration, performed numerically by FEMLab, was used to average the values across the entire tube opening. The reflection coefficient was then evaluated using Eq. (2.45).

Figure C.3 compares the reflection coefficient obtained using the FEM simulation and that predicted by Eq. (2.46). Two different sets of FEM results are shown, corresponding to the two different sizes of the region outside the tube. Again we see very good agreement in the magnitude and quite acceptable agreement in phase (though not perfect). As noted above, there are slight differences between the two FEM models, causing the numerical "wiggles" in the results.

The results shown in this Appendix affirm that the theory developed in Section 2.1

169
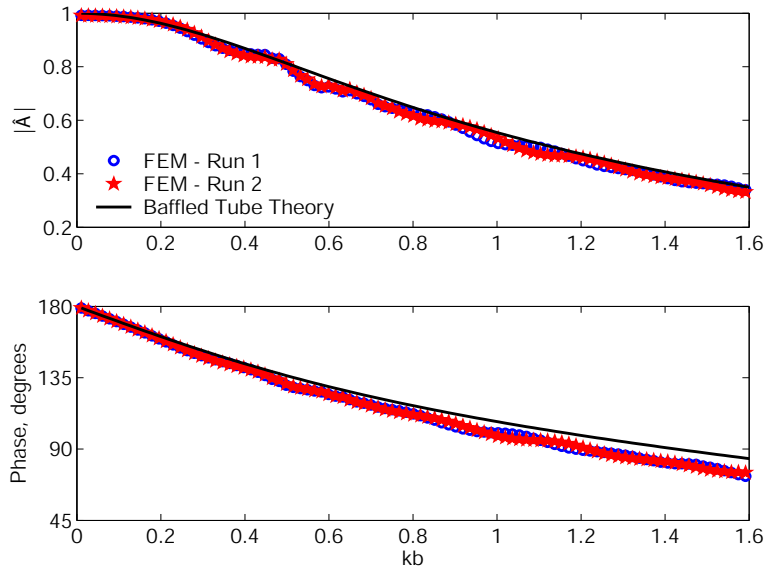
Figure C.3: Comparison of the magnitude and phase of the reflection coefficient predicted by Eq. (2.46) and two FEM models

accurately predicts the reflection coefficient for an open tube, at least in the range $0 < kb < 1.6$. This statement is made after comparison against the most complicated published theoretical result (to the author's knowledge) and a finite element model (which the author has verified against other theoretical results).

Appendix D

Technical Drawings
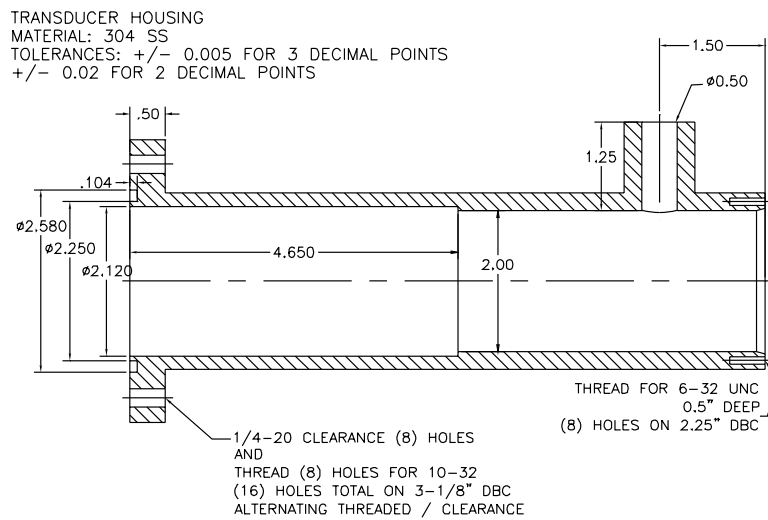
Figure D.1: Dimensioned drawing of source transducer housing

END CAP
MATERIAL: 304 SS
TOLERANCES: +/- 0.005 FOR 3 DECIMAL POINTS
+/- 0.02 FOR 2 DECIMAL POINTS

6-32 CLEARANCE
(8) HOLES ON
2.25" DBC

$\varnothing 2.50$

$\varnothing 1.920$

.50

.25

THREAD FOR 1/2"-NPT
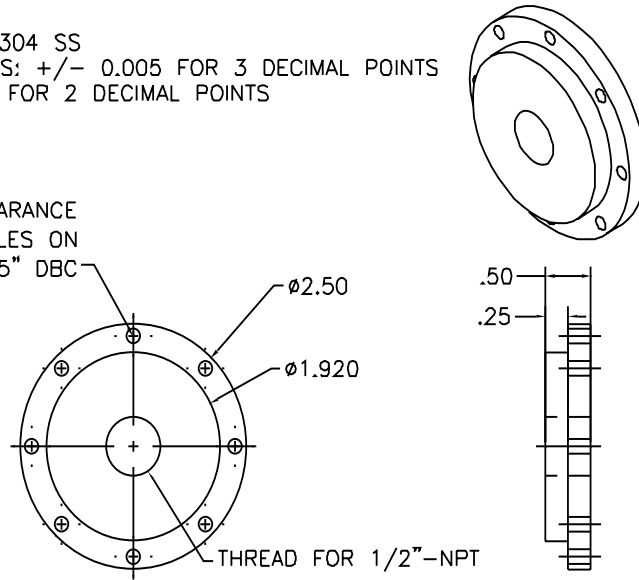
Figure D.2: Dimensioned drawing of source housing endcap

HEAD MASS
MATERIAL: 303 SS
TOLERANCES: +/- 0.005 FOR 3 DECIMAL POINTS
+/- 0.02 FOR 2 DECIMAL POINTS

.93

.167

.23

.056

.02

$\varnothing 1.798$

$\varnothing 1.411$

$\varnothing .492$

$\varnothing .348$

THREAD FOR
5/8-11 UNC
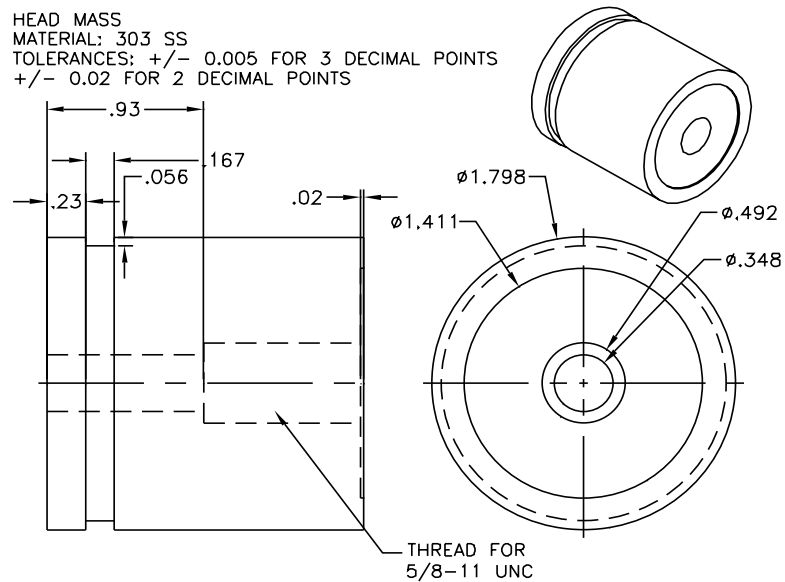
Figure D.3: Dimensioned drawing of source head mass

172

TAIL MASS
MATERIAL: 303 SS
TOLERANCES: +/- 0.005 FOR 3 DECIMAL POINTS
+/- 0.02 FOR 2 DECIMAL POINTS

1.27
.180
.060
.025

ø1.938
ø1.520
ø.625
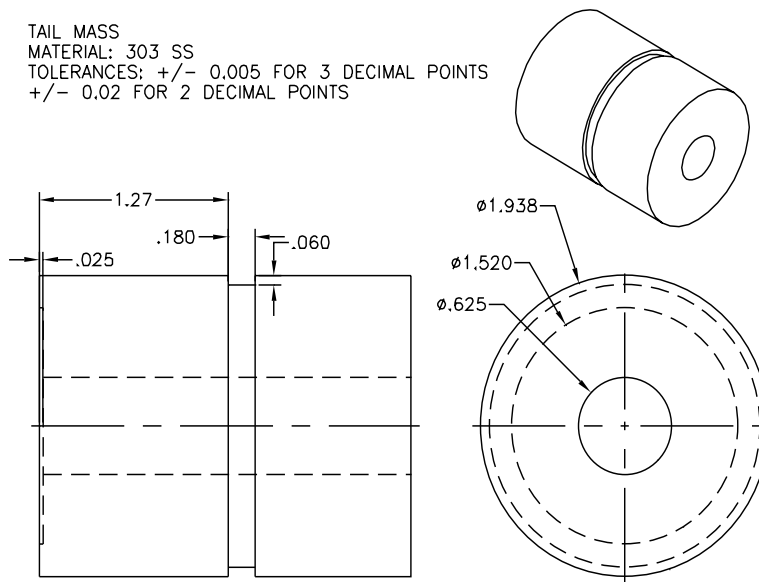
Figure D.4: Dimensioned drawing of source tail mass

Appendix E

Electrical Impedance of the Source Transducer

The electrical impedance is defined as the ratio between the voltage, V, and current, I:

$$Z_\Omega = \frac{V}{I} \tag{E.1}$$

and is a complex quantity, including both magnitude and phase information. The measured magnitude and phase of the impedance of the source transducer is shown in Figure E.1. The magnitude of the impedance is on the order of 100,000 Ω at low frequencies, while the voltage and current are 90° out of phase, expect at resonance. The primary resonance at 7 kHz is clearly visible in both plots.
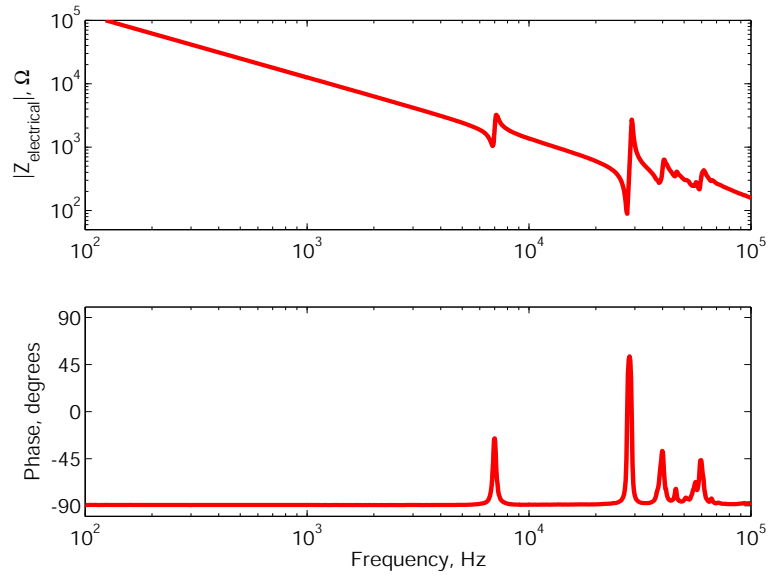
Figure E.1: Electrical Impedance of the source transducer while submerged in water. Resonances at 7 and 28 kHz are clearly visible.

Appendix F

MATLAB Scripts

This section contains some of the more useful MATLAB codes written by the author for this work. They are edited, condensed, and annotated for easy reading.

F.1 Impedance of baffled tube opening

This file, rigid_baffle.m, is a function that returns the theoretical impedance and reflection coefficient at the opening of a tube fitted with an infinite, rigid baffle. The input parameters are listed in the code.

```
function[Zout, Rout]=rigid_baffle(k1,k2,rho1,rho2,w,b)

%Returns complex reflection coefficient and impedance of a tube opening
%fitted with a rigid baffle.
%
%Use:
%
%[Z R]=rigid_baffle(k1,k2,rho1,rho2,w,b)
%
%Inputs:
```

```
%k1 = wavenumber INSIDE tube
%k2 = wavenumber OUTSIDE tube
%rho1 = density inside tube
%rho2 = density outside tube
%w = angular frequency
%b = tube radius

%Complex specific impedances:
Z1=rho1.*w./k1;        %Inside Tube
Z2=rho2.*w./k2;        %Outside Tube
gamma=Z1./Z2;          %Specific Impedance Ratio

%Impedance at opening:
kb=k2.*b;
Rz=1-2.*besselj(1,2.*kb)./(2.*kb);    %Resistance
Xz=2.*struve1(2.*kb)./(2.*kb);        %Reactance

%Outputs:
Zout=Z2.*(Rz-i.*Xz);                       %Impedance
Rout=(Rz-gamma-i.*Xz)./(Rz+gamma-i.*Xz);   %Reflection coefficient
```

F.2   Complex sound speed of a bubbly liquid

This file, C_and_P.m, returns the complex wavenumber, sound speed, phase speed, and

attenuation of a bubbly liquid as predicted by Commander and Prosperetti [29], Eqs. 2.74,

etc. The file bubble_XXX.m (see Section F.3) is called to provide the bubble distribution

as a function of void fraction and statistical bubble size parameters.

```
function[kout, cmout, cout, alphaout, Aout]=C_and_P(ap,pdf,w)

% Returns the complex wavenumber and sound speed for a bubbly liquid
% Uses Commander and Prossperetti, JASA 85, p732-746;
%
% Use:
%[k cm c alpha A]=C_and_P(ap,pdf,w)
%
%inputs:
```

```matlab
%ap  = radii vector (m) (use bubble_pdf.m or bubble_log.m)
%pdf = radius distribution corresponding to ap
%w   = driving frequency (rad/s) (can be a vector)
%
%outputs:
%k  = complex wavenumber (1/m)
%cm = complex sound speed (m/s)
%c  = phase speed (m/s)
%alpha = attenuation (1/m)
%A  = attenuation (dB/m)
%
%Calls fluid parameters in liquid_air_properties.m

liquid_air_properties;  %loads fluid properties

for aa=1:1:length(w)

%Bubble Calculations
b=bubble_b(ap,w(aa));           %Dampening Coefficient
w0=bubble_w0_driven(ap,w(aa));  %Resonant Frequency

%Calculate complex k;

int_p_k=ap.*pdf./(w0.^2-w(aa)^2+2*i*w(aa).*b); %Integrand

for bb=1:1:length(ap)-1 %Performs integration numerically
    s2(bb)=mean([int_p_k(bb) int_p_k(bb+1)]).*(ap(bb+1)-ap(bb));
end

k2=w(aa)^2/cl^2+4*pi*w(aa)^2.*sum(s2);  %Wavenumber Squared

%outputs:
kout(aa)=sqrt(k2);       %Complex Wavenumber
cmout(aa)=w(aa)./kout;  %Complex Sound Speed

cout(aa)=w(aa)./real(kmout(aa));    %Phase Speed
alphaout(aa)=imag(kmout(aa));       %Attenuation
Aout(aa)=20.*log10(exp(1)).*(alphaout(aa));

end
```

The following file, Kargl.m, applies Kargl's [58] effective medium correction to the previous file, returning a modified complex wavenumber, etc.

```
function[kout, cmout, cout, alphaout, Aout]=Kargl(ap,pdf,w)

%Returns the complex wavenumber and sound speed for a bubbly liquid
%using Kargl's effective medium approach (JASA 111(1) p 168-173)
%
% Use:
%[k cm c alpha A]=Kargl(ap,pdf,w)
%
%inputs:
%ap = radii vector (m) (use bubble_pdf.m)
%pdf = radius distribution corresponding to ap
%w  = driving frequency (rad/s) (can be vector)
%
%outputs:
%k  = complex wavenumber (1/m)
%cm = complex sound speed (m/s)
%c  = phase speed (m/s)
%alpha = attenuation (1/m)
%A  = attenuation (dB/m)
%
%Calls fluid parameters in liquid_air_properties.m
%

liquid_air_properties;   %loads fluid properties

for aa=1:1:length(w)     %cycles through frequency vector

%Bubble Calculations
w0=bubble_w0_driven(ap,w(aa));

%Calculate complex k;
err=0.1;  %Error limit in absolute wavenumber for while loop (1/m)
ka=0;      %Bad initial guess
kb=w(aa)./cl;   %Good starting point

while abs(ka-kb)>err     %Cycles until c_m in b_vis is close to prediction
    ka=kb;
    b=bvis(ap)+bth(ap,w(aa))+w(aa)*ka.*ap./2;       %Uses c_m in b_vis
    int_p_k=ap.*pdf./(w0.^2-w(aa)^2+2*i*w(aa).*b);  %Integrand
```

```
    for bb=1:1:length(ap)-1          %Performs numerical integration
        s2(bb)=mean([int_p_k(bb) int_p_k(bb+1)]).*(ap(bb+1)-ap(bb));
    end
    kb=sqrt(w(aa)^2/cl^2+4*pi*w(aa)^2.*sum(s2));  %New guess
end

%outputs:
kout(aa)=kb;              %Complex Wavenumber
cmout(aa)=w(aa)./kout;  %Complex Sound Speed

cout(aa)=w(aa)./real(kmout(aa));    %Phase Speed
alphaout(aa)=imag(kmout(aa));       %Attenuation
Aout(aa)=20.*log10(exp(1)).*(alphaout(aa));

end
```

F.3   Bubble size distribution

Two files, bubble_pdf.m and bubble_log.m provide a bubble size distribution to be used directly in either bubbly liquid file as a function of void fraction and statistical size parameters. The first, bubble_pdf.m, returns a Gaussian distribution (Eq. 2.77) for a given void fraction, bubble center radius, and standard deviation. The second file, bubble_pdf_log.m returns a log normal distribution (Eq. 4.3). The input parameters are void fraction, bubble center radius, and the log normal equivalent of a standard deviation, b_n. bubble_log.m is given below, bubble_pdf.m is of similar form, only the shape of the distribution changes.

```
function [alogout, logout] = bubble_log(a0,amin,amax,bn,beta,W)

%returns scaled distribution for given bubble sizes and void fraction
%
%use
%
```

```
% [alog plog]=bubble_log(a0,amin,amax,bn,beta,W)
%
%inputs:
% a0 = mean bubble radius (m) can be vector
% bn = deviation parameter    can be vector
% amin = minimum bubble size present (m)
% amax = maximum bubble size present (m)
% beta = void fraction
% W    = weighting factor (required if a0,bn are vectors)
%
%use of W:
% If a0=[2 5] and half the bubbles are centered around 2 and half around
% 5, then W=[0.5 0.5].  If 90% are centered around 2 and 10% around 5, then
% W=[0.9 0.1].  sum(W) need not be 1.
%
%outputs:
%alog = bubble size vector (m)
%plog = bubble size distribution (#/unit volume)

%Error if vector lengths disagree:
if abs(length(a0)-length(bn))>0
    error('lengths of a0 and bn do not agree')
end

%Radius Vector:
eps=0.01;  %Cuts off integration if distribution is less than 1% of max

Amin=min(a0.*exp(-sqrt(-log(eps)./bn)));   %Lower 1% bubble radius
Amax=max(a0.*exp(sqrt(-log(eps)./bn)));     %Upper 1% bubble radius

if amin<Amin
    amin=Amin;        %Lower overall limit
end if amax>Amax
    amax=Amax;        %Upper overall limit
end

ap=linspace(amin,amax,500);      %Bubble radius vector

%Distribution Shape:
if nargin==5|length(a0)==1  %If only one center radius (a0 not a vector)

    if length(a0)>1   %Error if W required and not given
```

```
        error('Please Specify a Weighting Factor, W')
    end

    p_vf=exp(-bn.*(log(ap./a0)).^2); %Distribution (yet to be scaled)

else                              %If a0 and bn are vectors
    p_vf=0; %start value
    for bb=1:1:length(a0)
        p_vf=p_vf+W(bb).*exp(-bn(bb).*(log(ap./a0(bb))).^2); %Adds next value
    end
end

%Distribution constant for given Void Fraction:
int_p_vf=ap.^3.*p_vf;        %Function to integrate

for aa=1:1:length(ap)-1     %Performs numerical integration
    sss(aa)=mean([int_p_vf(aa) int_p_vf(aa+1)]).*(ap(aa+1)-ap(aa));
end

C=beta*3./(4*pi)./sum(sss);  %Constant for Void Fraction

%Output:
logout=C.*p_vf;       %Weighted distribution
alogout=ap;           %Bubble radius vector
```

F.4   Single hydrophone TFM

These files returns the complex reflection coefficient and impedance measured by the single

hydrophone transfer function method. The first file, load_data.m, loads two files, one each

for the two measured hydrophone-source transfer functions, H_{1s} and H_{s2} for each frequency

band. The second file single_hydrophone_TFM.m uses this data to compute the effective

transfer function between the two hydrophones, H_{12}, and the reflection coefficient.

```
%load_data.m
```

```
%This file loads the data files and creates the required variables.
```

```
%The file names are in XYYMMDD## format, where YY is the year, MM is the
%month, and DD is the day.  The numbering corresponds to the order in which
%the measurements are made during a standard run.  The space delimitated
%ascii files are in the following format (f, Re(H), Im(H), C) where f is
%the frequency, H is the transfer function between channels 1 and 2, and C
%is the measured coherence between the two channels.

%  Load the data files.
load X04060301.ASC % nearest to surface 1-2kHz
load X04060302.ASC % nearest to surface 2-4kHz
load X04060303.ASC % nearest to surface 4-8kHz
load X04060304.ASC % nearest to surface 8-16kHz
load X04060305.ASC % furthest from surface 8-16kHz
load X04060306.ASC % furthest from surface 4-8kHz
load X04060307.ASC % furthest from surface 2-4kHz
load X04060308.ASC % furthest from surface 1-2kHz


%Frequency Vectors
fA=X04060301(:,1);      % 1-2 kHz
fB=X04060302(:,1);      % 2-4 kHz
fC=X04060303(:,1);      % 4-8 kHz
fD=X04060304(:,1);      % 8-16 kHz


%Complex Transfer Functions
H2A=X04060301(:,2)-i.*X04060301(:,3);   %H_s2, 1-2 kHz
H2B=X04060302(:,2)-i.*X04060302(:,3);   %H_s2, 2-4 kHz
H2C=X04060303(:,2)-i.*X04060303(:,3);   %H_s2, 4-8 kHz
H2D=X04060304(:,2)-i.*X04060304(:,3);   %H_s2, 8-16 kHz


H1A=X04060308(:,2)-i.*X04060308(:,3);   %H_1s, 1-2 kHz
H1B=X04060307(:,2)-i.*X04060307(:,3);   %H_1s, 2-4 kHz
H1C=X04060306(:,2)-i.*X04060306(:,3);   %H_1s, 4-8 kHz
H1D=X04060305(:,2)-i.*X04060305(:,3);   %H_1s, 8-16 kHz


%Coherence
CA=X04060301(:,4).*X04060308(:,4);      % 1-2 kHz
CB=X04060302(:,4).*X04060307(:,4);      % 2-4 kHz
CC=X04060303(:,4).*X04060306(:,4);      % 4-8 kHz
CD=X04060304(:,4).*X04060305(:,4);      % 8-16 kHz


%end load_data.m

%Impedance_Calculator.m
```

```
%inputs
loadit=1;    %Load Data?
T=18.9;      %Temperature

%Hydrophone locations (don't correct for acoustic center):
d0=7;            %nearest distance (inches)
dA=6.0+d0;       %far 1-2k
dB=3.0+d0;       %far 2-4k
dC=1.5+d0;       %far 4-8k
dD=0.75+d0;      %far 8-16k

%LOAD DATA ?
if loadit==1
load_data
end

%CONSTANTS
eps=6e-5;        %standard loss parameter, water in tube
b=2.601/100;     %inner radius of tube, m
ac=15.8e-3;      %distance to hydrophone acoustic center, m

%CALCULATIONS
%Water outside tube:
rho=rhotemp_NIST(T);      %Density at temperature
c0=ctemp(0,T);           %Sound speed at temperature

%Angular Frequencies:
wA = 2*pi.*fA;       %  rad/s
wB = 2*pi.*fB;
wC = 2*pi.*fC;
wD = 2*pi.*fD;

%Convert distances to (m):
d0=d0.*0.0254;
dA=dA.*0.0254;
dB=dB.*0.0254;
dC=dC.*0.0254;
dD=dD.*0.0254;

%Phase speed in tube, from LaFleur and Shields elastic waveguide theory:
cA=ctemp_LandS(T,fA);    %m/s
```

184

```
cB=ctemp_LandS(T,fB);
cC=ctemp_LandS(T,fC);
cD=ctemp_LandS(T,fD);

%Wave number in tube accounting for losses
kA=wA./cA.*sqrt(1+eps.*(1-i).*sqrt(2.*cA./wA)./b);  %1/m
kB=wB./cB.*sqrt(1+eps.*(1-i).*sqrt(2.*cB./wB)./b);
kC=wC./cC.*sqrt(1+eps.*(1-i).*sqrt(2.*cC./wC)./b);
kD=wD./cD.*sqrt(1+eps.*(1-i).*sqrt(2.*cD./wD)./b);

%Complex specific acoustic impedance in tube
Z0A=rho.*cA;      %kg/m2/s
Z0B=rho.*cB; Z0C=rho.*cC; Z0D=rho.*cD;

%Hydrophone Spacing, s:
sA = dA-d0;  % m
sB = dB-d0; sC = dC-d0; sD = dD-d0;

%Distance to furthest hydrophone:
LA =dA-ac ;    % m
LB =dB-ac ; LC =dC-ac ; LD =dD-ac ;

%Transfer function bethween hydrophones, H12:
HA = H2A.*H1A; HB = H2B.*H1B; HC = H2C.*H1C; HD = H2D.*H1D;

%Reflection Coefficient from Chung and Blaser
RA=exp(-kA.*(i*2*LA)).*(HA-exp(kA.*(i*sA)))./(exp(-kA.*(i*sA))-HA);
RB=exp(-kB.*(i*2*LB)).*(HB-exp(kB.*(i*sB)))./(exp(-kB.*(i*sB))-HB);
RC=exp(-kC.*(i*2*LC)).*(HC-exp(kC.*(i*sC)))./(exp(-kC.*(i*sC))-HC);
RD=exp(-kD.*(i*2*LD)).*(HD-exp(kD.*(i*sD)))./(exp(-kD.*(i*sD))-HD);

%end Impedance_Calculator.m
```

Bibliography

[1] Preston Scot Wilson. *Sound Propagation and Scattering in Bubbly Liquids.* Ph.D Dissertation, Boston University, Boston Massachusetts, 2002.

[2] D. C. Blanchard and A. H. Woodcock. Bubble formation and modification in the sea and its meteorological significance. *Tellus*, 9(2):145–158, 1957.

[3] Gordon M. Wenz. Acoustic ambient noise in the ocean: Spectra and sources. *The Journal of the Acoustical Society of America*, 34(12):1936–1956, 1962.

[4] Hugh C. Pumphrey and L. A. Crum. Free oscillations of near-surface bubbles as a source of the underwater noise of rain. *The Journal of the Acoustical Society of America*, 87(1):142–148, 1989.

[5] Lawernce A. Crum, Hugh C. Pumphrey, Ronald A. Roy, and Andrea Prosperetti. The underwater sounds produced by impacting snowflakes. *The Journal of the Acoustical Society of America*, 106(4):1765–1770, 1999.

[6] J. Ophir and K. J. Parker. Contrast agents in diagnostic ultrasound. *Ultrasound in Medicine and Biology*, 15(4):319–333, 1989.

[7] Edward O. Belcher. Quantification of bubbles formed in animals and man during decompression. *IEEE Transactions on Biomedical Engineering*, 27(6):330–338, 1980.

[8] Christopher E. Brennen. Cavitation in biological and bioengineering contexts. In *Fifth International Symposium on Cavitation (cav2003)*, Osaka, Japan, November 2003.

[9] M. R. Bailey, V. A. Khokhlova, O. A. Sapozhnikov, S. G. Kargl, and L. A. Crum. Physcial mechanisms of the therapeutic effect of ultrasound (a review). *Acoustical Physics*, 49(4):437–464, 2003.

[10] P. D. Jepson, M. Arbelo, R. Deaville, I. A. P. Patterson, P. Castro, J. R. Baker, E. Degollada, H. M. Ross, Herráez, A. M. Pocknell, F. Rodríguez, F. E. Howie, A. Espinosa, R. J. Reid, R. J. Jaber, J. R. Jaber, V. Martin, A. A. Cunningham, and A. Fernández. Gas-bubble lesions in stranded cetaceans. *Nature*, 425:575, October 2003.

[11] R.P. Taleyarkhan, C.D. West, J.S. Cho, R.T. Lahey Jr., R.I. Nigmatulin, and R.C. Block. Evidence for nuclear emissions during acoustic cavitation. *Science*, 295:1868–1873, 2002.

[12] R.P. Taleyarkhan, J.S. Cho, C.D. West, R.T. Lahey Jr., R.I. Nigmatulin, and R.C. Block. Additional evidence for nuclear emissions during acoustic cavitation. *Physical Review E*, 69(3), 2004.

[13] A. Mallock. The damping of sound by frothy liquids. *Proceedings of the Royal Society, Series A*, 84 (A 572):391–395, 1910.

[14] A. B. Wood. *A Textbook of Sound*. MacMillan, New York, 1930.

[15] Lyman Spizter Jr. Acoustic properties of gas bubbles in a liquid. Technical Report 6.1-sr20-918, National Defense Research Committee, July 1943.

[16] L. L. Foldy. Propagation of sound through a liquid containing bubbles, Part I: General theory. Navy Project Number NS-141. , Office of Scientific Research and Development, National Defense Research Committee, April 1944.

[17] Walter Kuhl, Erwin Meyer, Hermann Oberst, Eugen Skudrzyk, and Konrad Tamm. *Sound Absorption and Sound Absorbers in Water*. Bureau of Ships, United States Navy, Washington, DC, 1951. Translated from German by Charles E. Mongan, Jr.

[18] Herman Medwin. In situ acoustic measurements of bubble populations in coastal ocean waters. *Journal of Geophysical Research*, 75(3):599–611, 1970.

[19] E. L. Cartensen and L. L. Foldy. Propagation of sound through a liquid containing bubbles. *The Journal of the Acoustical Society of America*, 19(3):481–501, 1947.

[20] Francis E. Fox, Stanley R. Curley, and Glenn S. Larson. Phase velocity and absorption measurements in water containing air bubbles. *The Journal of the Acoustical Society of America*, 27(3):534–539, 1955.

[21] Edward Silberman. Sound velocity and attenuation in bubbly mixtures measured in standing wave tubes. *The Journal of the Acoustical Society of America*, 29(8):925–933, 1957.

[22] H. B. Karplus. The velocity of sound in a liquid containing gas bubbles. Technical Report C00-248, Armour Research Foundation of Illinois Institute of Technology, June 1958.

[23] Frederick W. Gibson. Measurement of the effect of air bubbles on the speed of sound in water. *The Journal of the Acoustical Society of America*, 48(5):1195–1197, 1970.

[24] M. Minnaert. On musical air-bubbles and sounds of running water. *The London, Edinburgh, and Dublin Philosophical Magazine and Journal of Science, Series 7*, 16:235–248, 1933.

[25] C. Devin. Survey of thermal, radiation, and viscous damping of pulsating air bubbles in water. *The Journal of the Acoustical Society of America*, 31(12):1654–1667, 1959.

[26] Andrea Prosperetti. Thermal effects on damping mechanisms in forced oscillations of gas bubbles in liquids. *The Journal of the Acoustical Society of America*, 61(1):17–27, 1977.

[27] Andrea Prosperetti. Thermal behavior of oscillating gas bubbles. *Journal of Fluid Mechanics*, 222:587–616, 1991.

[28] Andrea Prosperetti. Sound attenuation in a bubbly liquid. NCSC CR-87-40-3, Naval Coastal Systems Center, February 1987.

[29] Kerry W. Commander and Andrea Prosperetti. Linear pressure waves in bubbly liquids: Comparison between theory and experiments. *The Journal of the Acoustical Society of America*, 85(2):732–746, 1989.

[30] T. G. Leighton. *The Acoustic Bubble*. Academic Press, New York, 1994.

[31] Preston S. Wilson, Ronald A. Roy, and William M. Carey. An improved water-filled impedance tube. *The Journal of the Acoustical Society of America*, 133(6):3245–3252, 2003.

[32] John I. Dunlop. Measurement of acoustic attenuation in marine sediments by impedance tube. *The Journal of the Acoustical Society of America*, 91(1):460–469, 1992.

[33] Eun-Joo Park. Acoustic characterization of saturated sediments using a thick-walled water-filled impedance tube. Master's thesis, Boston Universtity, 2003.

[34] Preston S. Wilson and Ronald A. Roy. Acoustic characterization of marine sediments by impedance tube. Final Report for NSWC Grant No. N61331-02-1-G002, June 2003.

[35] Preston S. Wilson, Ronald A. Roy, and William M. Carey. Development of an impedance tube technique for *in-situ* classification of marine sediments. *The Journal of the Acoustical Society of America*, 133(4), 2003. Presented at 145th meeting of ASA, Nashville, TN.

[36] G.N. Watson. *A Treatise on the Theory of Bessel Functions*. Cambridge University Press, 1996.

[37] David T. Blackstock. *Fundamentals of Physical Acoustics*. John Wiley and Sons, New York, 2000.

[38] Y. Nomura, I. Yamamura, and S. Inawashiro. On the acoustic radiation from a flanged circular pipe. *Journal of the Physcial Society of Japan*, 15:510–517, 1960.

[39] N. Norris and I. C. Sheng. Acoustic radiation from a circular pipe with an infinite flange. *Journal of Sound and Vibration*, 135(1):85–93, 1989.

[40] Allan D. Pierce. *Acoustics: An Introduction to Its Physical Principles and Applications*. Acoustical Society of America, Woodbury, NY, 3rd edition, 1994.

[41] John William Strutt (Lord Rayleigh). *The Theory of Sound*, volume 2. Dover Publications, New York, 2nd edition, 1945.

[42] A. B. Warren. A note on the acoustic pressure and velocity relations on a circular disc and in a circular orifice. *Proceedings of the Physical Society*, 40:296–299, 1928.

[43] N. W. McLachlan. The acoustic and inertia pressure at any point on a vibrating circular disc. *The London, Edinburgh, and Dublin Philosophical Magazine and Journal of Science, Series 7*, 14(94):1012–1025, 1932.

[44] John William Strutt. The theory of resonance. *Philosophical Transactions of the Royal Society*, 161:77–118, 1871.

[45] Phillip M. Morse. *Vibration and Sound*. Acoustical Society of America, Woodbury, NY, 1992.

[46] Phillip M. Morse and K. Uno Ingard. *Theoretical Acoustics*. Princeton University Press, Princeton, NJ, 1986.

[47] Heinrich Stenzel. *Handbook for the Calculation of Sound Propagation Phenomena*. Naval Research Laboratory, Washington, DC, 1947. Translated from German by A.R. Stickley (NRL Translation 130); Originally published by Julius Springer, Berlin, 1939.

[48] Ronald M. Aarts and Augustus Janssen. Approximation of the struve function H_1 occurring in impedance calculations. *The Journal of the Acoustical Society of America*, 113(5):2635–2637, 2003.

[49] Harold Levine and Julian Schwinger. On the radiation of sound from an unflanged circular pipe. *Physical Review*, 73(4):383–406, 1948.

[50] D. S. Jones. The scattering of a scalar wave by a semi-infinite rod of circular cross section. *Philosophical Transactions of the Royal Society of London, Series A*, 247(934):499–528, 1955.

[51] Y. Ando. On the sound radiation from s semi-infinite circular pipe of certain wall thickness. *Acustica*, 22:219–225, 1969.

[52] M. Bernard and B. Denardo. Re-computation of Ando's approximation of the end correction for a radiating semi-infinite circular pipe. *Acustica*, 82:670–671, 1996.

[53] A. Selamet, Z. L. Ji, and R. A. Kach. Wave reflections from duct terminations. *The Journal of the Acoustical Society of America*, 109(4):1304–1311, 2000.

[54] J.-P. Dalmont, C. J. Nederveen, and N. Joly. Radiation impedance of tubes with different flanges: Numerical and experimental investigations. *Journal of Sound and Vibration*, 244(3):505–534, 2001.

[55] L. van Wijngaarden. On equations of motion for mixutes of liquid and gas bubbles. *Journal of Fluid Mechanics*, 33:465–474, 1968.

[56] William M. Carey. A derivation of the sonic speed relationship for bubbly liquids. unpublished notes, 2003.

[57] William M. Carey and Ronald A. Roy. Sound scattering from microbubble distributions near the sea surface. In D. D. Ellis, J. R. Preston, and H. G. Urban, editors, *Ocean Reverberation*, pages 25–44. Kluwer Academic, Dordrecht, Netherlands, 1993.

[58] Steven G. Kargl. Effective medium approach to linear acoustics in bubbly liquids. *The Journal of the Acoustical Society of America*, 111(1):168–173, 2001.

[59] Stanley A. Cheyne, Carl T. Stebbings, and Ronald R. Roy. Phase velocity measurements in bubbly liquids using a fiber optic laser interferometer. *The Journal of the Acoustical Society of America*, 97(3):1621–1624, 1994.

[60] J. Y. Chung and D. A. Blaser. Transfer function method of measuring in-duct acoustic properties. i. theory. *The Journal of the Acoustical Society of America*, 68(3):907–913, 1980.

[61] W. T. Chu. Transfer function technique for impedance and absorption measurements in an impedance tube using a single microphone. *The Journal of the Acoustical Society of America*, 80(2):555–560, 1986.

[62] A. F. Seybert and Benjamin Soenarko. Error analysis of spectral estimates with application to the measurement of acoustic parameters using random sound fields in ducts. *The Journal of the Acoustical Society of America*, 69(4):1190–1199, 1981.

[63] Standard test method for impedance and absorption of acoustical materials using a tube, two microphones and a digital frequency analysis system. ASTM Designation E 1050-98, American Society for Testing and Materials, West Conshohocken, PA, 1998.

[64] V. Gibiat and F. Laloe. Acoustical impedance measurements by the two-microphone-three-calibration (TMTC) method. *The Journal of the Acoustical Society of America*, 88(6):2533–2545, 1990.

[65] Phillip M. Morse and Herman Feshbach. *Methods of Theoretical Physics, Part II*. McGraw-Hill, New York, 1953.

[66] William Jacobi. Propagation of sound waves along liquid cylinders. *The Journal of the Acoustical Society of America*, 21(2):120–127, 1949.

[67] T. C. Lin and G. W. Morgan. Wave propagation through fluid contained in a cylindrical, elastic shell. *The Journal of the Acoustical Society of America*, 28(6):1165–1176, 1956.

[68] V. A. Del Grosso. Systematic errors in ultrasonic propagation parameter measurements, part 4: Effect of finite thickness elastic solid tubes enclosing the liquid of interest. NRL Report 6852, Naval Research Laboratory, Washington, DC, 1968.

[69] V. A. Del Grosso. Analysis of multimode acoustic propagation in liquid cylinders with realistic boundary conditions - application to sound speed and absorption measurements. *Acoustica*, 24:299–311, 1971.

[70] L. D. Lafleur and F. D. Shields. Low-frequency propagation modes in a liquid-filled elastic tube waveguide. *The Journal of the Acoustical Society of America*, 97(3):1435–1445, 1995.

[71] L. Elvira-Segura. Acoustic wave dispersion in a cylindrical elastic tube filled with a viscous liquid. *Ultrasonics*, 37:537–547, 2000.

[72] Jason Holmes. Vibrations of an infinite elastic cylinder with applications to towed hydrophone arrays. Presented for AM580, Theory of Elasticity, at Boston University, May 2004.

[73] Oscar B. Wilson. *An Introduction to the Theory and Design of Sonar Transducers*. Peninsula, Los Altos, CA, 1988.

[74] Hans Bodén and Mats Åborn. Influence of errors on the two-microphone method for measuring acoustic properties in ducts. *The Journal of the Acoustical Society of America*, 79(2):541–549, 1986.

[75] C. James Erickson and Charles D. Potts. *Mark's Standard Handbook for Mechanical Engineers*, chapter 15.1 Electrical Engineering. McGraw-Hill, New York, 10th edition.

[76] Krohn-Hite Corporation, Avon, MA. *Model MT-56 Operating and Maintence Manual*, 1977.

[77] R. W. Timme. Speed of sound in castor oil. *The Journal of the Acoustical Society of America*, 52(3):989–992, 1972.

[78] R. W. Fox and A. T. McDonald. *Introduction to Fluid Mechanics*. John Wiley and Sons, New York, 5th edition, 1998.

Vita

Jed Chester Wilbur was born in April, 1980 and grew up in the quiet town of Woodstock in northeastern Connecticut, the first of two sons to Paul and Florence Wilbur. Growing up he was forced to sped most of his time while not in school hauling stones, clearing brush, mending fences, splitting wood and many other arduous tasks which would, many years down the road, teach him the value of a hard day's work. Jed graduated from Woodstock Academy with high honors in 1998 and went on to attend Lafayette College in Easton, PA.

At Lafayette, Jed spent two years rowing for the crew team and then went on to found an outing club. He spent a semester studying in Brussels, Belgium and another month in South America before graduating *summa cum laude* with a Bachelor's of Science degree in Mechanical Engineering in 2002. After spending his summer working for a pharmaceutical company in France to complete a Bachelor's of Art degree in International Studies from Lafayette, Jed entered the Master's program at Boston University.

While at BU, Jed had the good fortune to join the physical acoustics group and work for Professor Ronald Roy. Here he studied the acoustics of multi-phase media, specifically bubbly liquids and water-saturated sediments. After completion of his Master's degree, Jed plans on working for a small research and development company in Lebanon, New Hampshire.

Permanent Address: 169 Hawkins Road, Woodstock Valley, CT 06282